PHILOSOPHICAL MAGAZINE

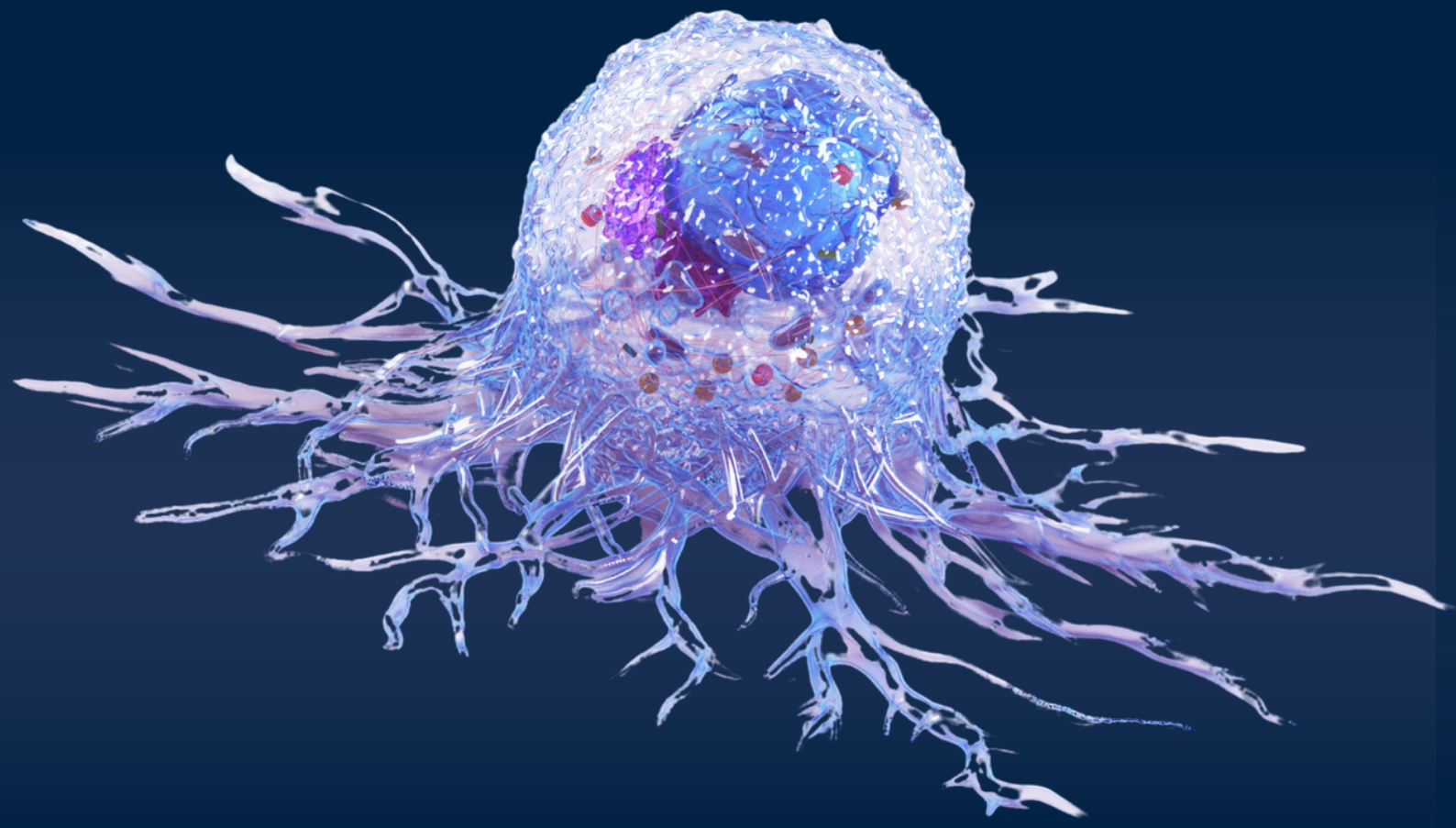

eBook:
Cancer as a physical system: Modeling and nanoscale innovations

Taylor & Francis
by informa

eBook

Cancer as a physical system: Modeling and nanoscale innovations

Contents

- An ablation study on hybrid quantum neural networks for enhancing brain tumour diagnosis
- Quantifying the organisation in cancer cell partitioning noise
- Modelling of nanosensors based on localised surface plasmon resonance
- A self-excitation point process model for quantifying nanoparticle agglomeration
- The phase-field model in tumor growth

Taylor & Francis
by informa

Taylor & Francis
Taylor & Francis Group

Philosophical Magazine

ISSN: 1478-6435 (Print) 1478-6443 (Online) Journal homepage: www.tandfonline.com/journals/tphm20

An ablation study on hybrid quantum neural networks for enhancing brain tumour diagnosis

Veerakumar Pandi & Kalaiselvi Thiruvenkadam

To cite this article: Veerakumar Pandi & Kalaiselvi Thiruvenkadam (15 Dec 2025): An ablation study on hybrid quantum neural networks for enhancing brain tumour diagnosis, Philosophical Magazine, DOI: 10.1080/14786435.2025.2600762

To link to this article: https://doi.org/10.1080/14786435.2025.2600762

PHILOSOPHICAL MAGAZINE
https://doi.org/10.1080/14786435.2025.2600762

Taylor & Francis
Taylor & Francis Group

An ablation study on hybrid quantum neural networks for enhancing brain tumour diagnosis

Veerakumar Pandi and Kalaiselvi Thiruvenkadam

Department of Computer Science and Applications, The Gandhigram Rural Institute-Deemed to be University, Gandhigram, India

ABSTRACT

The proposed work developed a robust hybrid quantum neural network model (HQNN) to mitigate the model overfitting problem for MRI brain tumour diagnosis. As quantum computing is the future of computation, the proposed work analyzed the impact of quantum layers on HQNN architectures and quantum advantages in improving model generalisation through an ablation study. We designed a single-layered shallow 10-Qubit parameterised quantum circuit (PQC) to reduce the model's overfitting. Fifteen HQNN models were designed, incorporating a diverse set of quantum gate arrangements to explore their effects on model performance. Through ablation experiments, the proposed work utilised the substantial impact of single-layered shallow PQC with R_X rotation, H-Gate superposition, and CZ entanglement in improving model expressivity and more stable performance on validation data, and enhanced the model's robustness. The proposed PQC compensates for the reduced regularisation effect caused by turning off 10% of neuron activations at each training step in the HQNN model. It improved the validation accuracy of the model by 4.73%, indicating better generalisation than classical FCNN models. The proposed work used brain tumour classification datasets from Kaggle and figshare repositories. We compared our HQNN model with state-of-the-art (SOTA) methods on standard MRI brain tumour datasets. The proposed HQNN model outperformed the SOTA methods with 98.17% test accuracy in binary classification and 96.97% test accuracy in multi-class classification.

ARTICLE HISTORY
Received 16 February 2025
Accepted 1 December 2025

KEYWORDS
MRI brain tumour analysis; machine learning; quantum computing; parameterised quantum circuits; hybrid quantum neural networks; ablation study

Introduction

Brain tumours are rapid and unexpected divisions of cells within brain tissues. These rapid tissue growths are divided into two types: benign and malignant. Benign tumours are non-cancerous and grow slowly, whereas malignant tumours are cancerous tissue growths that are considered aggressive and spread to other areas of the brain [1]. Central nervous system (CNS) tumours, such as Gliomas, meningiomas, and pituitary adenomas, account for 250,000 cases annually [2]. Identifying and characterising brain tumours and categorising them are crucial for diagnostics [3]. Current diagnostic methods face two major difficulties

CONTACT Kalaiselvi Thiruvenkadam kalaiselvi.gri@gmail.com Department of Computer Science and Applications, The Gandhigram Rural Institute-Deemed to be University, Gandhigram 624302, Tamilnadu, India

in identifying the tumour types: time consumption and interpretation variability across experts [4]. Advanced AI methods are needed to address these challenges, and enhance diagnostic accuracy and improve tumour type differentiation [5]. The proposed work designed a single-layered shallow 10-Qubit parameterised quantum circuit and integrated it into an optimised neural network model to improve the diagnostic accuracy and robustness of the model for MRI brain tumour classification.

Magnetic resonance imaging (MRI) [6] is a non-invasive, high-resolution, 3D imaging technique used for visualising complex brain tumour structures while avoiding radiation exposure. Since MRI produces hundreds of images per subject, manual inspection of MRI brain scans is a time-consuming task for radiologists and physicians. Manual techniques are hard to reproduce the results and impractical for huge volumes of data [7]. Artificial intelligence (AI) methods have proven accurate and fast in identifying and classifying brain tumours [8,9]. The AI methods for brain tumour diagnosis include machine learning (ML) classifiers, artificial neural networks (ANNs), and convolutional neural networks (CNNs) [7,10–14]. For MRI brain tumour classification, researchers have extracted radiomic features [15] [16], geometric features [17,18], statistical features [19,20], and deep features [21–23]. These features are utilised to train ML classifiers and ANN models.

CNN models work directly on images and extract superior features for autonomous learning. In recent years, the structure of CNNs has become more complex and diverse, leading to advanced CNN models. These advanced architectures replace traditional machine learning methods for segmenting and classifying brain tumours [24]. The modern deep learning models are effective and accurate in automatic segmentation of tumours and help radiologists in differentiating healthy brain tissues from cancerous ones with high precision [25–27].

The scarcity of comprehensive and balanced MRI brain tumour datasets is a major concern [28]. A limited amount of MRI brain tumour datasets is a bottleneck in medical image analysis and causes poor generalisation of deep learning models across different imaging conditions and tumour presentations [29]. CNNs use millions of complex, correlated parameters, making them prone to overfitting for small datasets [30]. In such cases, the network memorises noise instead of learning generalisable features. MRI brain images are complex due to multidimensionality, multiple contrast mechanisms, noise, and artifacts. Dropout [31] is one technique to overcome model overfitting by randomly dropping some units of the model. The other popular classical techniques to mitigate overfitting are regularisation and early stopping.

Quantum neural networks (QNNs), a subclass of quantum machine learning (QML), compute data using unique quantum properties: superposition, entanglement, and inference. CNNs are limited in their expressivity for complicated MRI brain images, and quantum neural networks can be more expressive due to superposition and entanglement [32]. Quantum machines can process complex operations and solve difficult problems better than classical computers [33]. QNNs can offer better generalisation with their unitary computing process [34]. QNNs train faster, express more functions, and generalise better than comparable classical models [35,36]. Quantum feature maps non-linearly encode classical input into high-dimensional quantum spaces [37], helping the QNN to capture complex patterns with limited training samples. Hybrid approaches use the best classical and quantum paradigms to solve problems in the current noisy intermediate-scale quantum era (NISQ). Modern hybrid quantum-classical

neural network models combine quantum circuits with neural networks [38–40]. Ablation studies on a hybrid quantum-classical neural network have proven quantum components enhancing the performance of the models [41–43].

However, QNNs with increased circuit depth face vanishing gradient problem called barren plateau [44]. The gradients of the cost function become exponentially small making the model unable to update the parameters effectively [45,46]. Using shallow PQCs with reduced circuit depth is a solid approach to mitigate exponential vanishing gradients in QNNs and effectively train the model against the barren plateau [47]. To design an effective hybrid quantum neural network model (HQNN), it is essential to systematically analyse both the architectural components of the quantum circuits and the hyperparameters of the neural networks [48,49].

The proposed work developed a shallow 10-Qubit PQC to avoid the barren plateau while maintaining the model's generalisation. We developed fifteen HQNN models incorporating a single-layer shallow PQC for MRI brain tumour classification and performed an empirical ablation study to identify the quantum advantage in each model's performance. The major contributions of the proposed work are summarised below:

(1) We designed a 10-qubit shallow PQC with a single quantum layer and blended it with an optimised neural network architecture. In the proposed work, we observed that the correlated quantum feature processing of MRI brain tumour images by the PQC enhanced the robustness of the proposed hybrid quantum neural network model.
(2) The proposed work performed an empirical ablation study on both the classical and quantum components. We conducted the ablation experiments in three stages as listed below:
    a. Ablation on classical neural network architecture to optimise the model.
    b. Ablation on the proposed single-layer shallow 10-Qubit PQC to configure the best combination of quantum gates for MRI brain tumour classification.
    c. Ablation on the PQC by varying the depth of the quantum circuit to observe the generalisation effect for increased quantum layers.
(3) The proposed work developed fifteen HQNN models. We evaluated the impact of fifteen different quantum gate combinations on brain tumour diagnosis using HQNN models. The results highlighted both positive and negative effects on performance. We observed a quantum advantage in terms of model generalisation, with the combination of Hadamard, R_X, and CZ gates significantly enhancing the validation performance of the proposed hybrid quantum-classical neural network.

The remainder of the article is structured as follows: Section 2 explores related works, while Section 3 delves into methodology. The findings of the proposed work are discussed in Section 4, and the conclusion is summarised in Section 5.

Related works

Existing research has developed advanced neural network architectures for MRI brain tumour classification. The rise of quantum machine learning has helped develop quantum neural networks and hybrid quantum neural network models for brain

tumour classification. This section discusses the related works to the proposed methodology.

AI models with PCA

Principal component analysis was employed for feature dimension reduction, and it improved the accuracy of the Support Vector Machines Model [50]. Basthikodi et al. extracted MRI brain features using Histogram of Oriented Gradients (HOG) and Local Binary Pattern (LBP) techniques. Their model scored 86.57% accuracy during validation. When used with PCA, the model scored 94.20% validation accuracy.

Shoaib et al. utilised pre-trained convolutional neural network models such as DenseNet201, EfficientNetB5, and InceptionResNetV2 to extract high-level features from MRI brain images for tumour classification. The high dimension MRI features from the models are as follows: 1920 features from DenseNet201, 1537 features from EfficientNetB5, and 2049 from InceptionResNetV2. To reduce the number of features and preserve the most important features, they used the PCA algorithm. The combination of DenseNet201 and PCA for support vector machines (SVM) and artificial neural networks (ANN) models gave superior performance with 100% and 98% accuracy scores for two different MRI brain tumour datasets [51].

In another study, for MRI brain tumour classification, PCA was used with Particle-swarm optimization (PSO) for feature optimisation and dimensionality reduction [52]. Pal et al. extracted radiomic features from MRI brain scans and further applied PSO and PCA. They used PCA to reduce the features and the xtreme gradient boosting (XGB) classifier scored 99.8%, 99.9%, and 99.7% accuracy, respectively. Pande & Chaki applied DenseNet121 and ResNet101 pre-trained models to MRI brain images for feature extraction. The features extracted by the two models (2048 + 1024 = 3072) were used to train a random forest classifier (RF), and it produced 98.1% accuracy. Using PCA, 3072 features were reduced to 2511 principal components. With the reduced features, the RF classifier saw better performance with 99.7% accuracy [53]. According to them, the PCA algorithm reduced the feature dimensions, improved training efficiency, and mitigated model overfitting.

Quantum models

An MRI-radiomics variational QNN model was developed to differentiate solitary large brain metastases (LBM) from high-grade gliomas (HGG) [54]. Felefly et al. extracted 1813 radiomic features from MRI brain images. They selected the 10 best features using a quantum annealer. They further reduced the features into three features using PCA. Three features were then encoded into quantum states using Y-axis rotations. For binary classification, they developed a QNN with a two-qubit parameterised variational circuit. When evaluated on test dataset, their QNN performed comparable to the XGB model and a dense neural network model with 74% balanced accuracy and 77% precision.

Kumar et al. developed a quantum support vector machine (QSVM) based quantum model for benign and malignant brain tumour classification [55]. They used the BraTS 2015 dataset. The thirteen features per sample in the dataset were reduced to 2 features

per sample using the PCA algorithm. The features were mapped into quantum states using ZZfeaturemap. They executed two quantum models: kernel-based QSVM and variational QSVM, in IBMQ Lima, a 5-qubit quantum processor. The models were also executed in two quantum simulators: STATEVECTOR and IBM QASM. The kernel-based QSVM performed better than the variational QSVM and classical SVM in accuracy and computational time. They observed that the 32-bit quantum simulators required less time than the 5-qubit real-time quantum processor to run the models.

A quantum convolutional neural network model developed by Ticku et al. performed better than the classical ResNet50 model with 92.13% test accuracy in MRI brain tumour classification [56]. They designed a quantum convolutional layer (QCL) with a quantum circuit, initialised with 4 qubits, and incorporated an R_X rotation gate to learn features. The circuit used Controlled-Rotation-X (CR_X) and CR_Z gates to pair neighbouring qubits. The classical image features are embedded into quantum states using Y rotation gates. With 4 qubits, the QCL assumed the input images were cut into 2*2 pixel squares. This was similar to a 2*2 kernel and a stride of 2 in classical CNN models. The QCL, comprising multiple stacked quantum circuits, learnt the features relevant to types of brain tumours through training iterations.

Hybrid quantum models

Akpinar & Oduncuoglu developed a hybrid quantum approach with classical ensemble feature selection and a parametrised quantum circuit for glioma grade classification with 74% accuracy [57]. They combined the features from the ensemble of 19 filter-based, embedded-based, and wrapper-based techniques for feature selection. They experimented with 6 parameterised quantum circuits for the classification task. The hyperparameters, such as the gates in the PQCs and feature map embedding, are adjusted to prepare 6 PQCs. As a result of their experimentation, they figured out that the PQC with R_Y, $R_{z,}$ and CY gates performed well.

A hybrid quantum-classical convolutional neural network architecture (QCCNN) was developed by Choudhuri & Halder for binary classification of MRI brain tumours [58]. They designed a QCL layer with an encoder to embed the image data into quantum states using rotation angles, a random quantum circuit to extract useful spatial details and features, and a decoder to measure the quantum data into classical form. Their hybrid model incorporates classical convolutional layers for further processing of the QCL output features. The architecture comprises two QCLs, two classical convolutional layers, a flatten layer, and two dense layers at the end. They used 3 datasets: BraTS 2013, Harvard Medical School dataset, and a private dataset. The QCCNN scored accuracy scores of 98.72%, 98.46%, and 98.17% on three datasets, respectively. Their findings demonstrate the better performance of QCCNN over a CNN architecture.

Depth-wise convolutional layers were integrated with quantum feature-encoding circuits, forming a hybrid quantum convolutional neural network (HQCNN) [32]. They designed a quantum circuit with an R_X gate for rotation angle adjustment during training and $CR_{X,}$ CR_Z gates for adjacent pairing of qubits. Their hybrid model produced 91.47% validation accuracy in MRI brain tumour classification. Ullah, M.S. et al. developed a hybrid approach incorporating pre-trained CNN models and a Quantum Theory-based Marine Predatory Optimization Algorithm (QTbMPA) for extracting and selecting

MRI brain image features [59]. They optimised the hyperparameters of the pre-trained InceptionResNetV2 and EfficientNetB0 models to extract features. The best among the extracted features are selected using QTbMPA for accurate classification. For the figshare brain tumour dataset, their classification model produced 99.80% accuracy.

A multi-level brain tumour classification model called Pyramid Quantum Dilated Convolutional Neural Network (PyQDCNN) was developed by Jetlin and Sherly [60]. They applied a U-Next model for MRI brain tumour segmentation. Initially, the PyQDCNN model was utilised to detect the presence of the tumour. After detection, the model was further used for multi-class classification of the brain tumours. For classification, the authors extracted features such as statistical, shape, and CNN features. The PyQDCNN model performed well for multi-class classification on the figshare dataset with 94.1% accuracy and 92.1% precision.

Research gap and motivation

In the current NISQ era, quantum machine learning is still in the development stages. The healthcare sector has not explored quantum computing and QML techniques fully [55]. With limited MRI brain images, Model overfitting, and poor generalisation are significant concerns in CNN models [28–30,32]. From the existing works [32,61,62], CNN models for MRI brain tumour classification faced the overfitting problem.

In [51] and [53,59,60], the authors extracted deep features from MRI brain images using pre-trained CNN models. The deep features can provide crucial hidden MRI information. But most of the features redundant and irrelevant to the classification tasks. Hence, a feature selection technique is needed to select important features and avoid overtraining of the classifiers. Hence, they used PCA to select important features.

Due to qubit limitations, in [54] and [55], the authors reduced the MRI brain features into three and two features for efficient quantum encoding. Representing the complex MRI brain images with two or three features to train a model might compromise the robustness of the model.

In [51,58], classical convolutional layers were used in the hybrid quantum models. Executing the hybrid models with a quantum circuit and millions of trainable parameters in CNN layers might lead to computational overhead. In [56], the stacking of multiple quantum circuits contributed to an increase in the model's architectural complexity. The quantum methods in [54] and [57] produced moderate performance with 74% accuracy.

Model generalisation is important in medical diagnosis models to create a real-time impact. In the proposed work, we utilised a shallow 10-Qubit PQC in creating a robust HQNN model for MRI brain tumour classification. The proposed work used PCA to extract the ten best features from MRI brain images. To handle each feature efficiently, we used ten qubits to encode each feature into one qubit. The proposed 10-qubit hybrid quantum model has proven to be a robust model with generalised performance on both validation and test data.

QNNs offer different performances for different quantum gates [63]. More experiments are needed to demonstrate the quantum advantages and compare QNNs with classical neural networks, thereby showing better generalisation in QNNs [33]. Hence, the proposed work performed various ablation experiments to analyze the quantum advantages in the proposed HQNN models for MRI brain tumour classification.

Methodology

The proposed methodology developed a hybrid quantum neural network model and performed ablation studies on classical and quantum modules. The PCA algorithm is utilised to reduce the high dimensions of MRI brain images into meaningful principal components. The FCNN and HQNN architectures were developed by choosing the appropriate layers, activation functions, and other necessary hyperparameters. The elements of the proposed architectures are removed and replaced to find the best-performing HQNN model. Figure 1 provides the graphical abstract of the proposed work.

Data augmentation

Data Augmentation [64] techniques ensure adequate images are supplied to the neural network models, specifically when the dataset holds a minimum images. In image datasets, data augmentation involves creating images similar to the existing ones. It is necessary to prepare more images for model training and avoid data imbalance problems where the number of images in one class may exceed the others. The imbalanced dataset may affect the model's training significantly [65]. The proposed work employed a symmetry-based data augmentation technique for MRI brain images, where flip, mirror, and rotation operations are applied to the brain images.

Quantum feature extraction

The proposed work extracted 10 best features from MRI brain images using PCA, and encoded the features into quantum states. PCA reduces the dimensions of high-dimensional MRI brain images and retains significant information. It reduces the dataset's

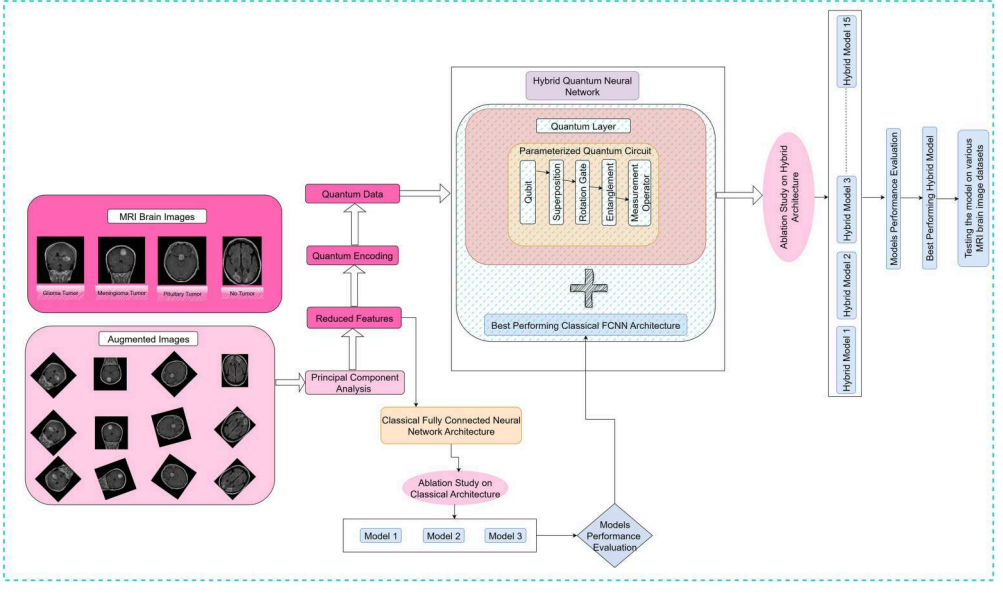

Figure 1. Framework of the proposed methodology.

complexity, recognising subtle patterns by amplifying the similarities and differences. The reduced features help the neural networks detect the subtle patterns in MRI images and improve the model's performance [50–52]. For hybrid quantum neural networks, the PCA features are well-suited for quantum data encoding and PQC training.

Quantum data encoding [66] embeds classical MRI features into quantum states, enabling it to be processed in quantum computations. Angle encoding [67] is one technique to map features into quantum states. This technique encodes classical features as a rotational angle on a qubit within the Bloch sphere [68], a unit sphere representing a qubit's orientation in quantum state space. Angle encoding is used in hybrid quantum neural networks for MRI brain tumour classification and has been proven to be effective [58,69,70]. The proposed work uses the R_X rotation gate and 10 qubits to facilitate an efficient quantum representation of 10 classical MRI brain features.

At first, 10 essential features from MRI brain images were extracted using PCA. The MRI brain images with the dimensions of (m × n) are flattened into a one-dimensional vector with d = m × n dimensions. Given N images, the matrix X with size N × d represents a new dataset, each row corresponding to a flattened image.

The flattened data are normalised as shown in Equation (1) to have zero mean and unit variance which avoids bias towards features with high magnitudes. The mean (μ) is subtracted from each feature. $X_{normalized}$ is the normalised brain image dataset.

$$X_{normalized} = X - \mu \tag{1}$$

As shown in Equation (2), the covariance matrix C is computed to capture the relationship between different features in the dataset.

$$C = \frac{1}{N} X_{normalized}^{T} X_{normalized} \tag{2}$$

From the covariance matrix C, the eigenvector matrix V is computed, where the eigenvectors correspond to principal components. The eigenvalue decomposition is applied to the covariance matrix C, as shown in Equation (3).

$$C = V \Lambda V^{\mathrm{T}} \tag{3}$$

Λ represents the diagonal matrix of eigenvalues. The eigenvalues are sorted in descending order, and their corresponding eigenvectors are rearranged accordingly. The top 10 eigenvectors (principal components) that capture the most significant variance in the data are selected since they represent the essential features of MRI brain images. The selected principal components transform the normalised MRI data into a new feature space. The projection of the original data $X_{normalized}$ onto the principal components is shown in Equation (4).

$$Y = X_{normalized} V_{10} \tag{4}$$

V_{10} is the matrix containing the top 10 eigenvectors. Y is the transformed data matrix with the dimension of N × 10.

The PCA-transformed dataset with n samples and d features is represented as Equation (5).

$$X_{pca} \in \mathbb{R}^{n \times d}, \text{ where } d = 10 \tag{5}$$

The samples are represented as rows in $X_{pca,}$ and the feature vector for a single sample is represented as Equation (6).

$$x^i = [x_1^i, x_2^i, \ldots . x_{10}^i] \in \mathbb{R}^{10}, \text{ where i} = 1, 2, \ldots, \text{n} \tag{6}$$

The 10 essential MRI brain features for each sample are encoded into quantum states. The proposed work used 10 qubits for the encoding scheme, and each qubit represents one feature. The d qubits are initialised to the basis state $|0\rangle^{\otimes d}$. The R_x rotation gate is a single-qubit rotation gate that rotates the qubit state around the X-axis of the Bloch sphere.

The classical feature x_i from the PCA-transformed dataset X_{pca} is normalised to a rotation angle $\theta_i \in [0, \pi]$ via min–max scaling (Equation 7). Here, $\min(X_{pca})$ and $\max(X_{pca})$ are computed globally across all features to ensure consistent encoding.

$$\theta_i = \pi \times \frac{x_i - \min(X_{pca})}{\max(X_{pca}) - \min(X_{pca})} \tag{7}$$

For each feature x_i in a given sample, an R_x gate is applied to the corresponding qubit as shown in Equation (8).

$$R_{x(x_i)} = e^{-i\, x_i X/2}, \text{ where X is the Pauli-X operator} \tag{8}$$

R_x rotation encodes the features into quantum states (Equation 9).

$$|\psi_i\rangle = \cos\left(\frac{x_i}{2}\right)|0\rangle - i\sin\left(\frac{x_i}{2}\right)|1\rangle \tag{9}$$

The $R_X(\theta)$ transformation encodes classical feature x_i into a quantum state parameterised by the angle $x_{i,}$,which is normalised to $[0, \pi]$ (Equation 7). This angle controls the probability amplitude of measuring the qubit states. The quantum circuit for a single sample is represented in Equation 10.

$$U_{encode} = \otimes_{i=1}^{d} R_x(x_i) \tag{10}$$

Here U_{encode} is applied to the initial state $|0\rangle^{\otimes d,}$ and each qubit independently encodes a feature.

Proposed HQNN

QNNs use quantum circuits (PQC) analogous to dense layers in classical neural networks for processing information [71,72]. HQNN combines classical neural network architectures with PQCs, which is a promising approach for image classification [72–74]. PQC prepares quantum states with quantum processors, and the measurements are carried out by measurement operators. The measured values are processed by classical layers [75]. In designing PQC, the R_X rotation gate better enhances the expressibility of the circuit than R_Y and R_Z [76]. Shallow quantum circuits that run in constant time can be more powerful than classical circuits [77].

In the proposed work, the HQNN model is designed by integrating the proposed shallow PQC with the fully connected neural network architecture to process quantum-encoded MRI brain features. After PQC, the measured quantum features are processed by dense layers for classification. To analyse the impact of quantum gates in

PQC for MRI brain tumour classification, the proposed work designed 15 PQCs with different quantum gates, such as rotation gates R_X, R_Y, and R_Z, entanglement gates CZ and CNOT, and Hadamard gate for superposition. The design of the proposed 10-Qubit PQC with Hadamard gate (H) superposition, parameterised R_X rotation, and Controlled-Z (CZ) entanglement is shown in Figure 2.

The PQC processes 10 quantum-encoded MRI brain features using parameterised R_X gate to encode features for learning, a CZ gate entanglement for correlated feature processing, and Pauli-Z to measure the outcomes of each qubit.

For each feature, the circuit applies superposition using the H gate. This gate transforms computational basis states into superpositions as Equation 11.

$$H = \frac{1}{\sqrt{2}}\begin{pmatrix} 1 & 1 \\ 1 & -1 \end{pmatrix} \tag{11}$$

The basis state transformations on $|0\rangle$ and $|1\rangle$ mentioned in Equation 12 and Equation 13.

$$H|0\rangle = H\begin{pmatrix} 1 \\ 0 \end{pmatrix} = \frac{1}{\sqrt{2}}\begin{pmatrix} 1 & 1 \\ 1 & -1 \end{pmatrix}\begin{pmatrix} 1 \\ 0 \end{pmatrix} = \frac{1}{\sqrt{2}}\begin{pmatrix} 1 \\ 1 \end{pmatrix} = \frac{|0\rangle + |1\rangle}{\sqrt{2}} \tag{12}$$

$$H|1\rangle = H\begin{pmatrix} 0 \\ 1 \end{pmatrix} = \frac{1}{\sqrt{2}}\begin{pmatrix} 1 & 1 \\ 1 & -1 \end{pmatrix}\begin{pmatrix} 0 \\ 1 \end{pmatrix} = \frac{1}{\sqrt{2}}\begin{pmatrix} 1 \\ -1 \end{pmatrix} = \frac{|0\rangle - |1\rangle}{\sqrt{2}} \tag{13}$$

For an arbitrary single-qubit state (Equation 14), the superposition is applied as Equation 15.

$$|\psi\rangle = \alpha|0\rangle + \beta|1\rangle \tag{14}$$

$$H|\psi\rangle = \frac{1}{\sqrt{2}}\begin{pmatrix} \alpha + \beta \\ \alpha - \beta \end{pmatrix} \tag{15}$$

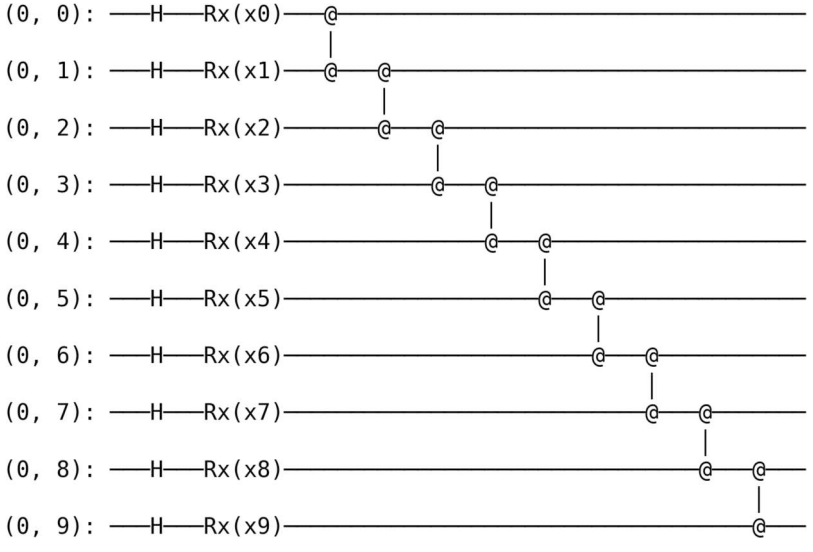

Figure 2. Proposed 10-Qubit Shallow PQC.

As all 10 qubits are initialised to $|0\rangle^{\otimes d}$, the H gate puts them into uniform superposition (Equation 16)

$$H^{\otimes 10}|0\rangle^{\otimes 10} = \frac{1}{\sqrt{2^{10}}}\sum_{k=0}^{2^{10}-1}|\mathrm{k}\rangle\ ,\ \text{where}\ |\mathrm{k}\rangle = |k_0 k_1 \ldots k_9\rangle \tag{16}$$

$|\mathrm{k}\rangle$ represents all possible 10-qubit basis states. The parameterised $R_x(\theta_i)$ gate adjusts the probability amplitudes during training, assuming θ_i as the trainable parameter for the i-th qubit (Equation 17). For classification, θ_i is tuned to minimise a cost function.

For a qubit in state $|k_i\rangle$, where $k_i \in \{0, 1\}$, and $1 - k_i$ is the flipped state of k_i

$$R_x(\theta_i)|k_i\rangle = \cos\left(\frac{\theta_i}{2}\right)|k_i\rangle - i\sin\left(\frac{\theta_i}{2}\right)|\overline{k_i}\rangle \tag{17}$$

Each $R_x(\theta_i)$ transforms the i-th qubit's state $|k_i\rangle$ as in Equation 17. For the proposed 10-qubit PQC, the R_x gates are applied to all qubits in the superposition state (Equation 18)

$$\otimes_{i=0}^{9}R_x(\theta_i)\left(\frac{1}{\sqrt{2^{10}}}\sum_{k=0}^{2^{10}-1}|k\rangle\right) = \frac{1}{\sqrt{2^{10}}}\sum_{k=0}^{2^{10}-1} \otimes_{i=0}^{9}\left(\cos\left(\frac{\theta_i}{2}\right)|k_i\rangle - i\sin\left(\frac{\theta_i}{2}\right)|1-k_i\rangle\right) \tag{18}$$

The controlled-Z (CZ) gate is a two-qubit gate to create entanglement between qubits. Here, a Pauli-Z operation is applied to the target qubit only when the control qubit is in the $|1\rangle$ state.

Consider two-qubit basis states $\{|00\rangle, |01\rangle, |10\rangle, |11\rangle\}$, the task of a CZ gate between them is to introduce a phase flip to the $|11\rangle$ state, leaving all other states unchanged.

For the 10-qubit system, CZ gates are applied to adjacent qubits sequentially as defined in Equation (19).

$$U_{entangle} = \prod_{i=1}^{9} CZ_{i-1,i} \tag{19}$$

Considering the states of the qubits after $R_X(\theta)$ as $|\Phi\rangle$, the entangled state $|\Phi_{\text{entangled}}\rangle$ becomes Equation (20).

$$|\Phi_{\text{entangled}}\rangle = U_{entangle}|\Phi\rangle \tag{20}$$

With entanglement, the states of qubits are made interdependent by applying CZ gates in the grid. This allows for feature correlations that classical systems cannot replicate.

The quantum states are measured using the Z measurement operator to extract classical information from the final quantum states. The measurement operator for a single-qubit and the proposed 10-qubit system are shown in Equation (21) and Equation (22).

$$\hat{Z} = |0\rangle\langle 0| - |1\rangle\langle 1| = \begin{pmatrix} 1 & 0 \\ 0 & -1 \end{pmatrix} \tag{21}$$

$$\hat{Z}^{\otimes 10} = \otimes_{i=0}^{9}\hat{Z}^{(i)} \tag{22}$$

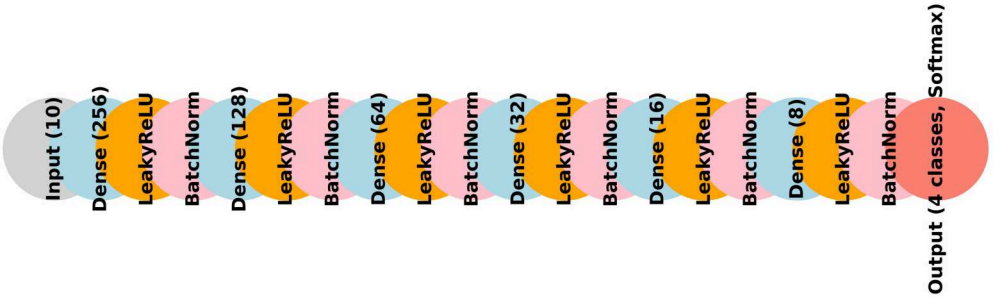

Figure 3. Proposed FCNN architecture.

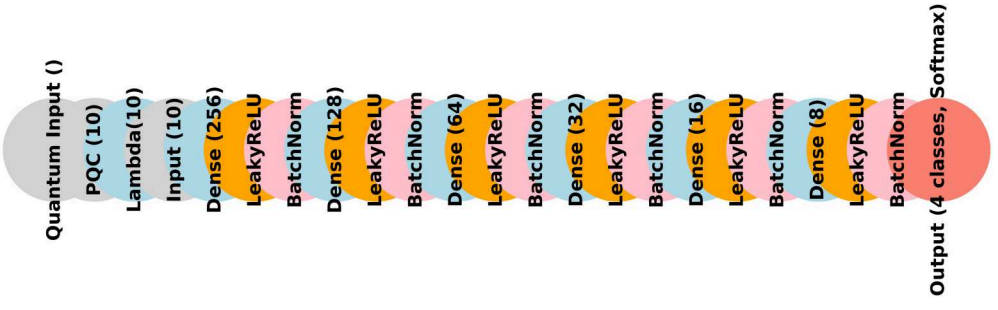

Figure 4. Proposed HQNN architecture.

The measurement returns the probabilistic outcome of bitstrings $\{S_0\ S_1\ S_2 \ldots S_9\}$, where $S_i \in \{0,1\}$.

A lambda layer is used to reshape the PQC output to ensure the output has a consistent shape that can be fed into subsequent classical neural network layers. The proposed classical and hybrid quantum neural network architectures are shown in Figures 3 and 4.

Ablation study

QNNs show varied performance depending on quantum gate variations [63]. Designing and testing of quantum layers with different combinations of gates reveals the impact of each gate on the model's performance. Ablation removes a certain component of the model and replaces it with another component, which eventually leads to differences in the outcome. The measured difference marks the impact of the component on the model's performance. In the proposed work, an ablation study is performed on classical FCNN to determine the best-performing classical component combination. Table 1 outlines the architectures of the proposed classical FCNN models. For the hybrid models, the FCNN1 architecture, which has the fewest parameters among the models, is integrated with a quantum layer. The ablation study is conducted on hybrid quantum neural network architectures by altering the combinations of quantum gates. The proposed hybrid architectures are shown in Table 2.

Table 1. Proposed fully connected neural network models.

Layer	Attribute	FCNN1	FCNN2	FCNN3
Input	Type	Input Layer	Input Layer	Input Layer
	Input Shape	(10,)	(10,)	(10,)
Dense_1	Units	-	512	512
	Activation	-	Leaky ReLU	Leaky ReLU
Dropout_1	Dropout Rate	-	0.2	0.1
Dense_2	Units	256	256	256
	Activation	Leaky ReLU	Leaky ReLU	Leaky ReLU
Dropout_2	Dropout Rate	0.2	0.2	0.1
Dense_3	Units	128	128	128
	Activation	Leaky ReLU	Leaky ReLU	Leaky ReLU
Dropout_3	Dropout Rate	0.2	0.2	0.1
Dense_4	Units	64	64	64
	Activation	Leaky ReLU	Leaky ReLU	Leaky ReLU
Dropout_4	Dropout Rate	0.2	0.2	0.1
Dense_5	Units	32	32	32
	Activation	Leaky ReLU	Leaky ReLU	Leaky ReLU
Dropout_5	Dropout Rate	0.2	0.2	0.1
Dense_6	Units	16	16	16
	Activation	Leaky ReLU	Leaky ReLU	Leaky ReLU
Dropout_6	Dropout Rate	0.2	0.2	0.1
Dense_7	Units	-	8	8
	Activation	-	Leaky ReLU	Leaky ReLU
Dropout_7	Dropout Rate	-	0.2	0.1
Output	Units	4 (Multiclass Classification)	4 (Multiclass Classification)	4 (Multiclass Classification)
	Activation	Softmax	Softmax	Softmax

Results and discussion

Dataset

The proposed work uses four brain tumour classification datasets taken from Kaggle and figshare repositories for training and validating the proposed models. The details of the datasets are listed in Table 3. The Brain Tumour MRI Dataset [78] and Brain Tumour Classification dataset [79] contain 4 classes of MRI brain images: glioma, meningioma, pituitary, and no tumour. The Brain Tumour Dataset [80] contains three classes of images: glioma, meningioma, and no tumour. The Br35H Brain Tumour Detection

Table 2. Proposed hybrid quantum neural network models.

Model	Classical Component	Quantum Components		
		Variational parameter	Superposition	Entanglement
HQNN1	FCNN1	R_X gate	H-Gate	CZ gate
HQNN2	FCNN1	R_Y gate	H-Gate	CZ gate
HQNN3	FCNN1	R_Z gate	H-Gate	CZ gate
HQNN4	FCNN1	R_X gate	H-Gate	C-NOT gate
HQNN5	FCNN1	R_Y gate	H-Gate	C-NOT gate
HQNN6	FCNN1	R_Z gate	H-Gate	C-NOT gate
HQNN7	FCNN1	R_X gate	Did not Applied	CZ gate
HQNN8	FCNN1	R_Y gate	Did not Applied	CZ gate
HQNN9	FCNN1	R_Z gate	Did not Applied	CZ gate
HQNN10	FCNN1	R_X gate	Did not Applied	C-NOT gate
HQNN11	FCNN1	R_Y gate	Did not Applied	C-NOT gate
HQNN12	FCNN1	R_Z gate	Did not Applied	C-NOT gate
HQNN13	FCNN1	R_X gate	Did not Applied	Did not Applied
HQNN14	FCNN1	R_Y gate	Did not Applied	Did not Applied
HQNN15	FCNN1	R_Z gate	Did not Applied	Did not Applied

Table 3. Datasets description.

Dataset	Available at	Number of Images and Classes
Brain Tumour MRI Dataset [78]	https://www.kaggle.com/datasets/masoudnickparvar/brain-tumor-mri-dataset	7022 (4 classes)
Brain Tumour Classification (MRI) [79]	https://www.kaggle.com/datasets/sartajbhuvaji/brain-tumor-classification-mri	3264 (4 classes)
Brain Tumour Dataset [80]	https://figshare.com/articles/dataset/brain_tumor_dataset/1512427	3064 (3 classes)
Br35H:: Brain Tumour Detection 2020 [81]	https://www.kaggle.com/datasets/ahmedhamada0/brain-tumor-detection/data	3000 (2 classes)

2020 [81] contains two classes of MRI brain images, such as tumour and no tumour. The proposed work used the Brain Tumour MRI Dataset to train the FCNN and HQNN models. The best-performing model was trained and validated using the remaining datasets to prove the reliability and versatility of the proposed hybrid model architecture for brain tumour diagnosis.

Experimental setup

The proposed classical and hybrid quantum neural network models were developed and trained with quantum simulators using Jupyter Notebook in Google Colab. The experiments were conducted on the Google Compute Engine with the NVIDIA T4 GPU to accelerate processing. This setup facilitated an efficient model development for the quantum-classical architectures.

Evaluation metrics

Table 4 lists the evaluation metrics used to analyze the performances of the proposed models. Here TP, TN, FP and FN stands for true positives, true negatives, false positives and false negatives. Throughout this article, the metrics are expressed as percentages.

Experimental results

This section discusses experimental results of the proposed FCNN and HQNN models. The models were developed and tested through the ablation study, where the impacts of different components on model performance are analysed. The various experiments conducted with the proposed FCNN and HQNN models, Improved HQNN1 model, and PQCs with varying circuit depths are presented in the following sub-sections.

Fully connected neural network models performance comparison

Table 5 compares the performances of the proposed FCNN models.

From Table 5, the FCNN1 model showed a promising performance with scores over 85% in all the metrics. The FCNN2 model, an extended version of the FCNN1 with two additional dense layers, saw improved performance with scores over 90% in most metrics. Adding the two layers resulted in more computational time for FCNN2 than FCNN1. The FCNN3 model was an enhanced model from FCNN2 with a reduced dropout rate of 0.1. The reduced dropout rate in FCNN3 caused a notable discrepancy

Table 4. Evaluation metrics.

Metric	Formula	Description
Accuracy	$Accuracy = (TP + TN) \div (TP + TN + FP + FN)$	The proportion of correctly classified instances among all instances.
Precision	$Precision = TP \div (TP + FP)$	The proportion of true positives among all predicted positives (how accurate positive predictions are).
Recall	$Recall = TP \div (TP + FN)$	The proportion of true positives among all actual positives (sensitivity of the model).
F1 Score	$F1\ Score = 2 \times (Precision \times Recall) \div (Precision + Recall)$	The harmonic mean of Precision and Recall, balancing the two metrics.
Specificity	$Specificity = TN \div (TN + FP)$	The proportion of true negatives among all actual negatives (how well negatives are identified).
Matthews Correlation Coefficient (MCC)	$MCC = (TP \times TN)(FP \times FN) \div \sqrt{(TP + FP)(TP + FN)(TN + FP)(TN + FN)}$	The measure of classification quality that provides balanced assessment of prediction performance considering true and false positives and negatives.

between its training and validation accuracy (94.20−87.52 = 6.68). However, the model predicted the tumour types better than FCNN1 and FCNN2 in the test data. This improved performance comes with the trade-off of having the longest training time among the models.

Figure 5 shows the models' training and validation accuracy scores for 500 epochs. Among the three models, FCNN2 aligned closely with its training accuracy as epochs progressed, suggesting better generalisation in Figure 5(b). The gap between training and validation accuracy scores started developing in FCNN1 after the 100th epoch in Figure 5(a), while the gap created in FCNN3 after the 50th epoch Figure 5(c). However, FCNN3 performed better in training accuracy than other models; its generalisation needed improvement.

Hybrid quantum neural network models performance comparison

The proposed hybrid quantum models are constructed by integrating the FCNN1 architecture with the shallow parameterized quantum circuits (PQCs). Training 15 hybrid quantum models is a time-consuming task. To reduce the computational time of 15

Table 5. FCNN Models performance.

Model	Train Accuracy	Validation Accuracy	Test Accuracy	F1 Score	Precision	Recall	Specificity	MCC	Elapsed Time(in milliseconds)
FCNN1	86.92	83.36	85.96	85.59	85.55	85.96	95.31	81.23	182263
FCNN2	90.52	90.17	90.08	89.98	89.92	90.08	96.73	86.70	209763
FCNN3	94.20	87.52	91.84	91.78	91.78	91.84	97.30	89.06	232117

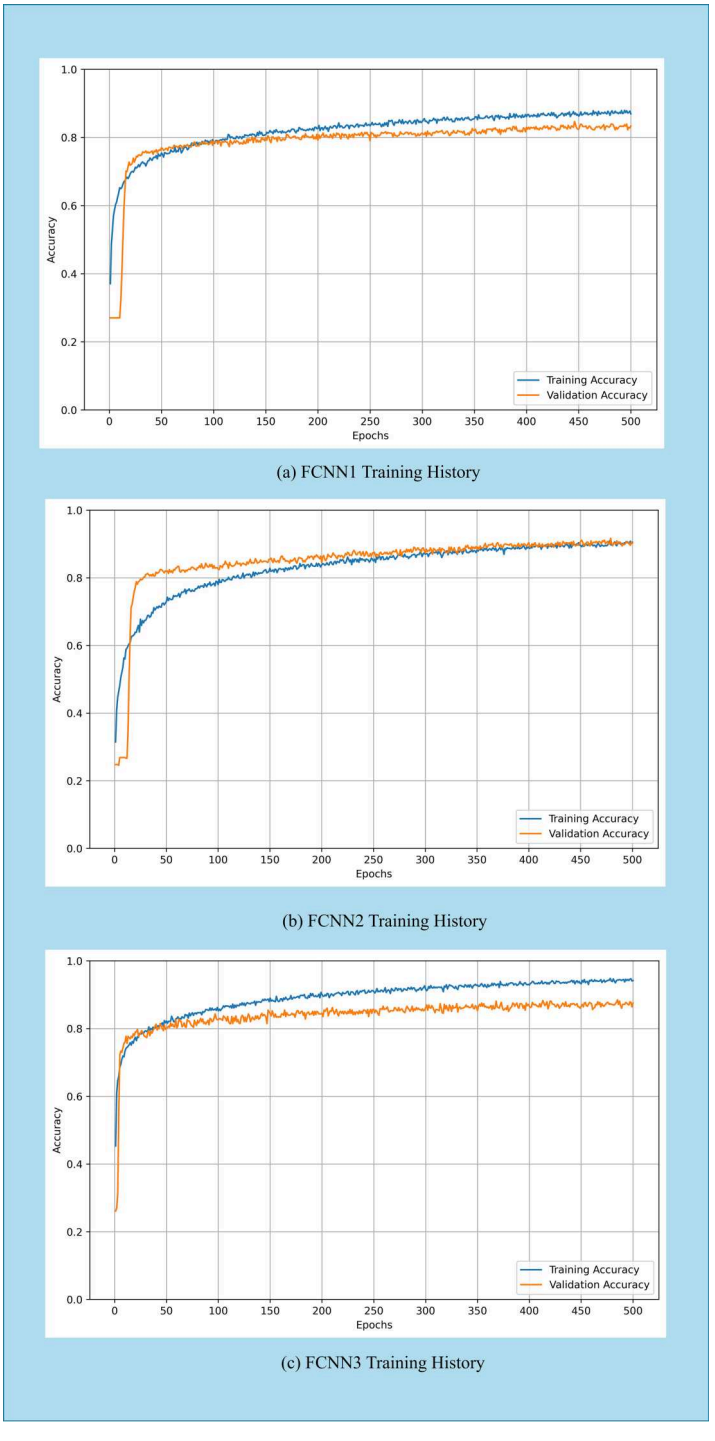

(a) FCNN1 Training History

(b) FCNN2 Training History

(c) FCNN3 Training History

Figure 5. Training Histories of FCNN models.

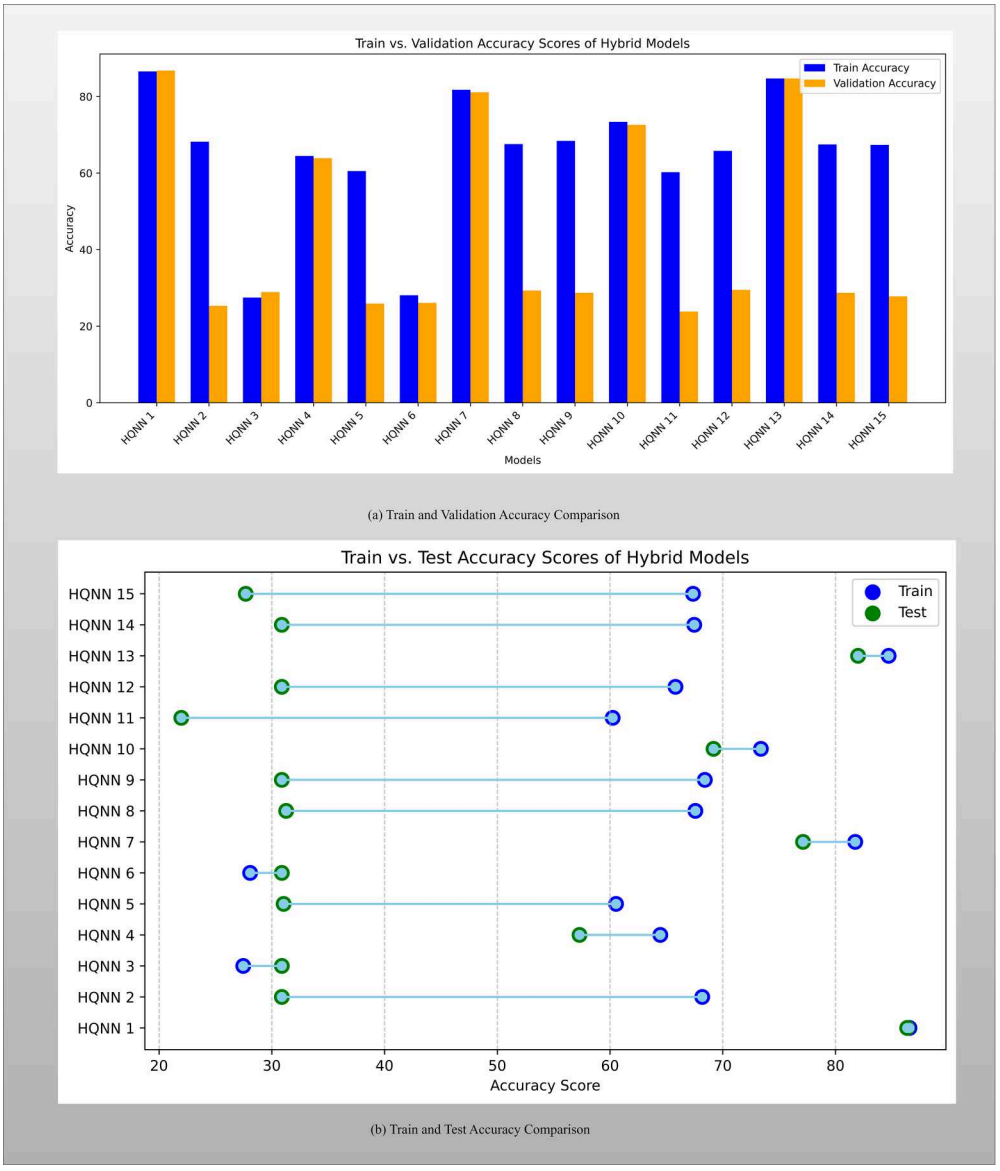

Figure 6. Train, validation, and test accuracy scores comparison of the proposed hybrid models.

hybrid models, FCNN1 is chosen over FCNN3 as it requires the minimal training time. Figure 6 presents a comparison of the training, validation, and test accuracy scores achieved by the hybrid models.

Figure 6(a) compares the training and validation accuracies of the proposed hybrid quantum models. Among the 15 models, HQNN1, HQNN7, and HQNN13 showed superior performance with 86.56%, 81.75%, and 84.71% training accuracy scores. Notably, these three models utilised R_X gates as variational parameters, facilitating more effective processing of input data than models using R_Y or R_Z gates. In the HQNN13 model, PQC was constructed with only R_X rotations, and no entanglement or superposition. In HQNN7, along with R_X

rotations, CZ entanglement was incorporated into the circuit, which saw a slight dip in performance. We created the HQNN1 model with the PQC comprising R_X rotations, CZ entanglement, and H-gate superposition. This resulted in better performance than HQNN7 and HQNN13. The other hybrid models that used R_X rotations are HQNN4 and HQNN10. However, their performance was average as they utilised CNOT gates instead of CZ gates for entanglement. From this, we understand that the PQC with a combination of R_X rotations, CZ entanglement, and H-gate superposition is promising compared to others in the proposed HQNN architecture.

Figure 6(b) shows the differences between training and test accuracies. The data indicate that HQNN1, HQNN7, and HQNN13 exhibit higher test accuracy and better generalisation than other models. From Figure 6(a) and Figure 6(b), the close alignment of validation and test accuracy scores with training accuracy suggests that HQNN1 achieves strong generalisation capabilities, indicating its robustness on unseen data. This ablation shows that the PQCs with R_X rotations help better model generalisation.

The performances of the proposed hybrid quantum models on test data are shown in Table 6.

Table 6 compares all performance metrics for the proposed hybrid models evaluated on the test dataset. The HQNN1 consistently achieved the highest scores across all performance metrics, demonstrating superior effectiveness over other models. Although the HQNN7 and HQNN13 performed near HQNN1 in every metric, they failed in MCC. The higher MCC (81.75%) of HQNN1 showed consistently accurate predictions for both the positive and negative classes. Evidently, the models utilising R_X gates only show a decent MCC score. In contrast, others failed to correctly identify the positive and negative classes with MCC scores of zero and below zero. However, HQNN1 also requires a greater amount of elapsed time for training compared to other models. For elapsed time, the hybrid model HQNN14 completed its training quickly.

Improved HQNN1

HQNN1 proved to be the robust model of the 15 hybrid models in the ablation experiment. From Table 5, FCNN3 is a better performer than FCNN1. Hence, the HQNN1

Table 6. Hybrid models performance comparison.

Models	Gates Combination	Test Accuracy	F1 Score	Precision	Recall	Specificity	MCC	Elapsed Time(in milliseconds)
HQNN1	$R_X + H + CZ$	**86.35**	**85.96**	**85.91**	**86.35**	**95.44**	**81.75**	2082924
HQNN2	$R_Y + H + CZ$	30.89	14.58	9.54	30.89	75	0	2053762
HQNN3	$R_Z + H + CZ$	30.89	14.58	9.54	30.89	75	0	1859715
HQNN4	R_X +H + CNOT	57.29	56.66	56.66	57.82	85.94	43.87	2026640
HQNN5	R_Y +H + CNOT	31.05	15.03	27.05	31.05	75.06	2.61	2003544
HQNN6	$R_Z + H + CNOT$	30.89	14.58	9.54	30.89	75	0	1989365
HQNN7	R_X +CZ	77.12	75.33	76.23	77.12	92.33	69.92	1462704
HQNN8	R_Y +CZ	31.27	17.15	15.16	31.27	75.33	3	1604241
HQNN9	$R_Z + CZ$	30.89	14.58	9.54	30.89	75	0	1711384
HQNN10	R_X +CNOT	69.18	68.49	68.38	69.18	89.66	58.71	1593364
HQNN11	R_Y +CNOT	21.97	10.16	25.19	21.97	74.55	−4.56	1597344
HQNN12	R_Z +CNOT	30.89	14.58	9.54	30.89	75	0	1584287
HQNN13	R_X	82.00	80.53	81.34	81.01	93.61	74.79	1193370
HQNN14	R_Y	30.89	14.58	9.54	30.89	75.00	0	**1124603**
HQNN15	R_Z	27.69	17.62	31.85	27.69	76.39	13.30	1272477

architecture is improved by replacing its classical architecture (FCNN1) with FCNN3, aiming to boost the hybrid model's performance. This approach effectively combines the best-performing classical and quantum components to enhance the hybrid quantum model's capabilities. Figure 7 compares the improved HQNN1 with the performances of other models such as FCNN1, FCNN3, and the original HQNN1.

As shown in Figure 7, HQNN1 performed equally to FCNN1 in all metrics except validation accuracy. Its predictions in validation data were 3.41% better than classical FCNN1. However, the improved HQNN1 outperformed all other models across each performance metric, demonstrating the effectiveness of combining optimal classical and quantum components in the hybrid architecture.

Figure 7 shows that, while the training accuracy of the improved HQNN1 (93.90%) is nearly equal to that of FCNN3 (94.20%), its validation accuracy (92.25%) significantly surpasses FCNN3 (87.52%). Evaluation metrics on test data further reveal that the improved HQNN1 outperforms the classical model. This enhanced performance highlights the advantage of incorporating the proposed shallow parameterised quantum circuits into classical neural networks in terms of performance. However, this improved performance comes at the cost of computational time: as shown in Figure 8, the improved HQNN1 required approximately 9 times the training time of FCNN3. Since the PQC used 10 qubits and the quantum simulation is carried out on classical hardware, the hybrid model takes more time to train than classical models.

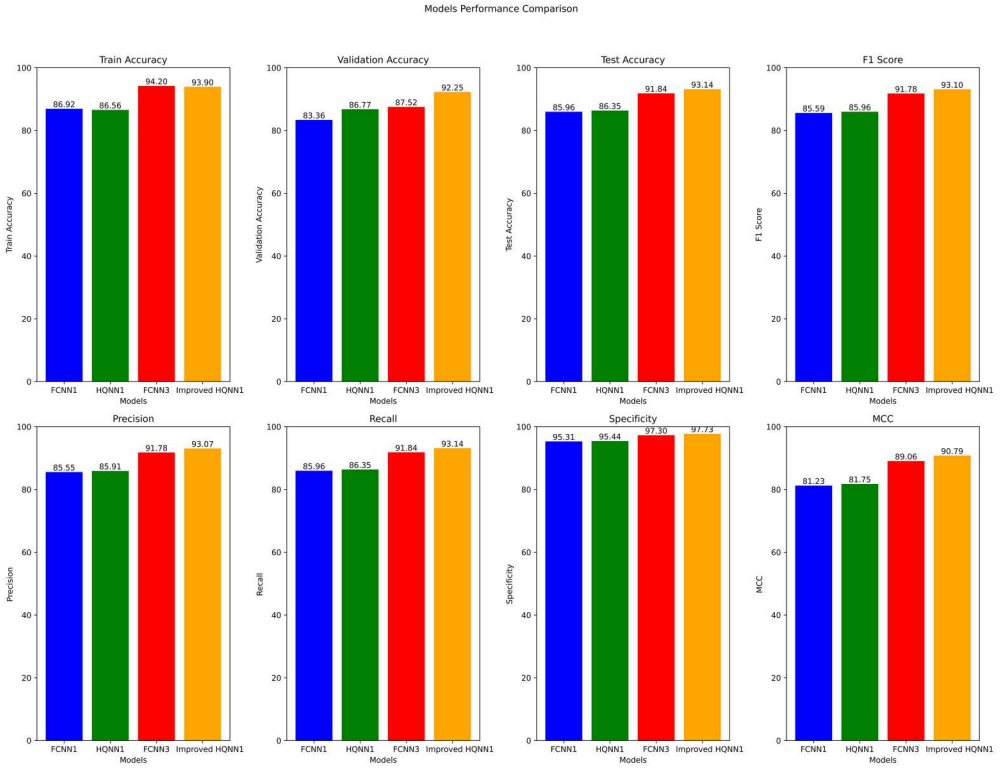

Figure 7. Performance comparison of FCNN1, HQNN1, FCNN3 and improved HQNN1.

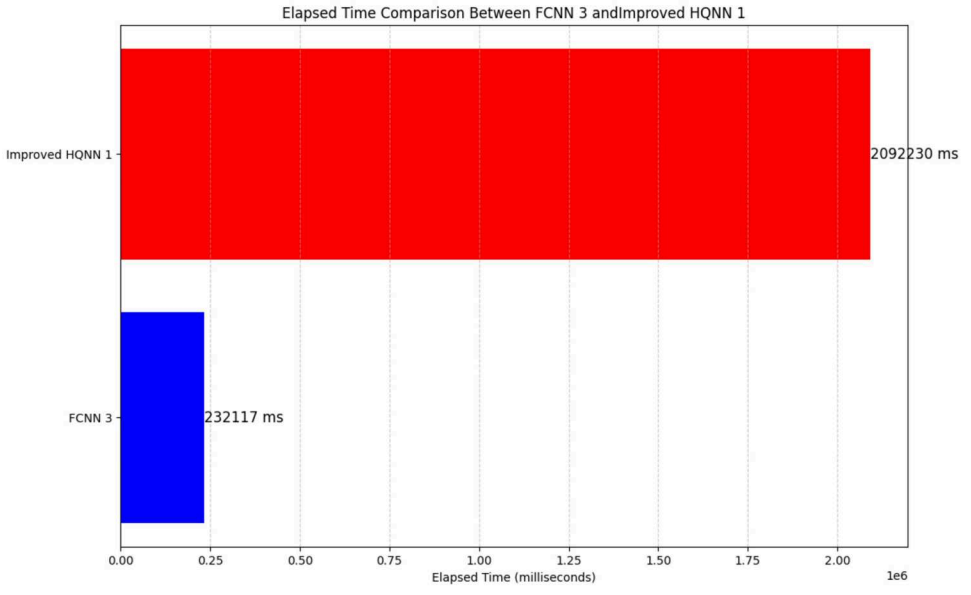

Figure 8. Elapsed time of FCNN3 and improved HQNN1.

The training histories of the proposed FCNN3 and improved HQNN1 for 500 epochs are plotted in Figure 9. In the Improved HQNN1, validation and training accuracies were closely aligned across epochs, even with a 0.1 dropout rate. According to Table 5, the validation accuracies of FCNN2 and FCNN3 were 90.17% and 87.52%, respectively, with dropout rates of 0.2 and 0.1. From Table 1, FCNN2 and FCNN3 had almost similar architectures with the same number of dense layers, neurons, and activation functions. The only difference between them was the dropout rate. FCNN2 used a dropout rate of 0.2, while FCNN3 used 0.1. Dropout reduces the model overfitting by randomly dropping some units of the model during training [31]. The FCNN2 with a 0.2 dropout rate temporarily disabled 20 percent of a layer's neuron weights at a training step to mitigate overfitting. Figure 5(b) shows that the tight alignment of training and validation accuracy curves indicates the perfect generalisation of the FCNN2 model. In FCNN3, the dropout rate was reduced to 0.1, resulting in a significant gap between the model's training and validation performance over 500 epochs. The accuracy plot in Figure 9(a) showed that the FCNN3 model was prone to overfitting and might struggle to generalise effectively to unseen data. Optimising the dropout rate in FCNN3 might enhance the model's performance on validation data. However, the proposed work integrated the FCNN3 with a shallow PQC with Hadamard, RX, and CZ gates, forming the Improved HQNN1 model, which improved the validation accuracy to 92.25% in Figure 9(b). Incorporating the shallow PQC compensated for the reduced 0.1 dropout rate, improved the validation accuracy by 4.73% (92.25−87.52 = 4.73) and mitigated the generalisation issues observed in FCNN3. The shallow PQC in the improved HQNN1 contributed to better regularisation, enhancing its robustness and adaptability to unseen data.

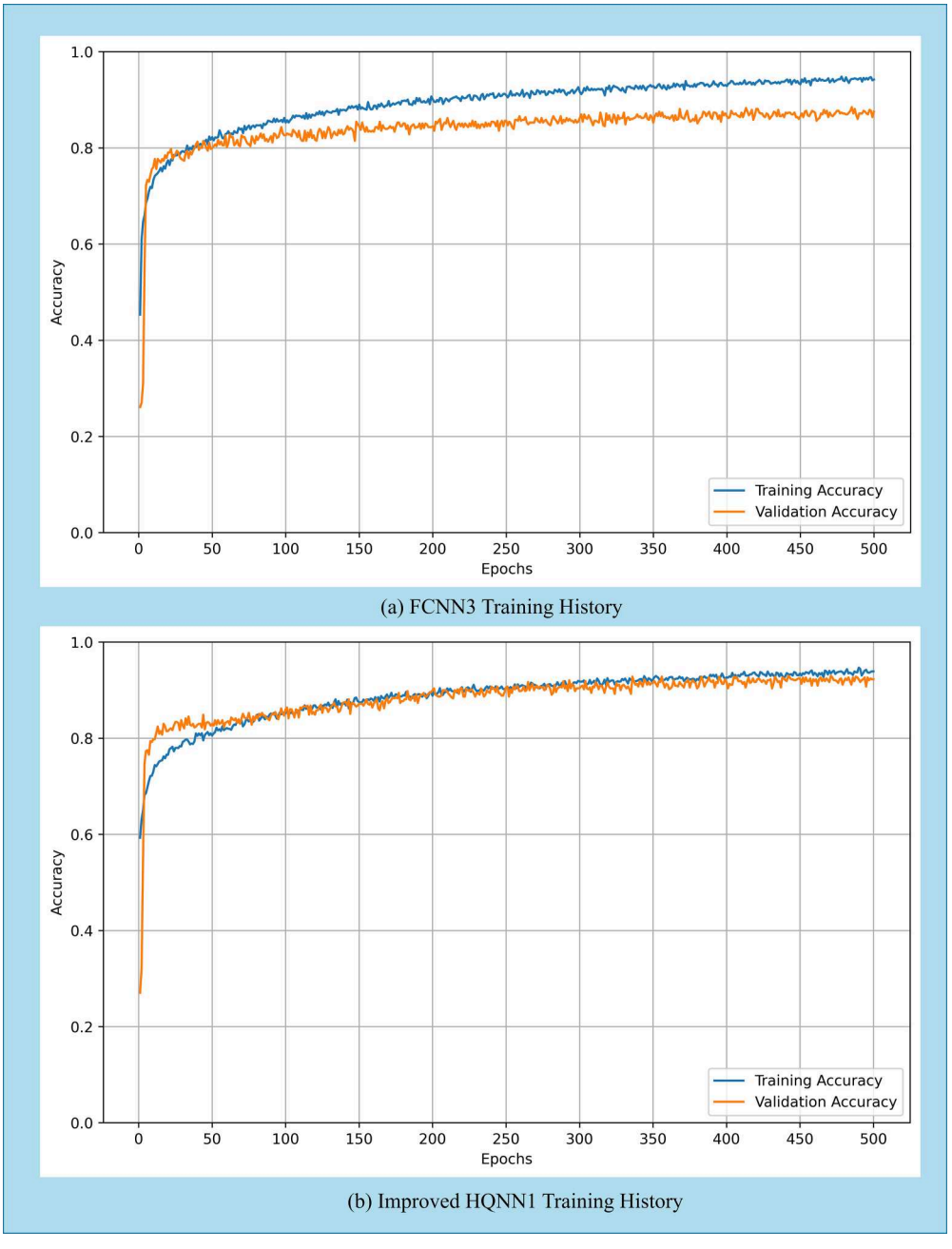

Figure 9. Training histories of FCNN3 and improved HQNN1.

Experimenting with superposition, entanglement, and varying circuit depths

The proposed work analysed the impact of shallow PQCs in the proposed HQNN architectures through an ablation on circuit depth. Here, we experimented with HQNN models by integrating the FCNN3 architecture with different shallow PQCs. We increased the circuit depth of the PQCs through repeated quantum layers. In this ablation, we carried out three experiments with 9 different shallow PQCs, detailed in Table 7.

Table 7. Experimentation details of the circuit depth ablation.

Experiments	PQCs	Parameterised Rotation	Entanglement	Superposition	Number of Quantum Layers
Experiment A	Shallow PQC_1	R_X gate	CZ gate	Not applied	1
	Shallow PQC_2	R_X gate	CZ gate	Not applied	2
	Shallow PQC_3	R_X gate	CZ gate	Not applied	3
Experiment B	Shallow PQC_4	R_X gate	Not applied	H gate	1
	Shallow PQC_5	R_X gate	Not applied	H gate	2
	Shallow PQC_6	R_X gate	Not applied	H gate	3
Experiment C	Shallow PQC_7	R_X gate	CZ gate	H gate	1
	Shallow PQC_8	R_X gate	CZ gate	H gate	2
	Shallow PQC_9	R_X gate	CZ gate	H gate	3

We used R_X rotation gates in the PQCs throughout all the experiments and executed the models for 500 epochs. The training and validation accuracies of the models executed in experiments A, B, and C are plotted in Figures 10–12.

In Figure 10(a), the shallow PQC_1 with entanglement and no superposition resulted in unstable validation accuracy scores over the epochs. As the quantum layers increased in shallow PQC_2 and shallow PQC_3, the instability in the validation performance increased despite the smooth and stable increase in the training scores in Figure 10(b) and (c). Without superposition, the qubits were initialised to their basis states, and entanglement was applied only to the basis states, limiting the PQCs from exploring superposed states. This limited the expressivity of the quantum circuit. The shallow PQCs with entanglement alone failed to generalise to unseen data despite good training accuracy, indicating overfitting specifically with increased quantum layers.

In Figure 11, the validation accuracies improved when superposition was introduced to the shallow PQCs and entanglement was removed. With a single quantum layer in shallow PQC_4, the validation scores in Figure 11(a) were higher than training accuracies at initial epochs, tightly aligned at middle epochs, and a minimal gap between train and validation score developed during final epochs. The gap developed from early mid-epochs in Figures 11(b) and (c) and progressively enlarged until the final epochs as quantum layers increased in shallow PQC_5 and shallow PQC_6. Superposition allowed the shallow PQCs to explore broader quantum state spaces. It helped to steadily improve the validation performance over the epochs, indicating the improved generalisation of the HQNN on unseen data.

In Figure 12, the generalisation gap further reduced when the superposition and entanglement were incorporated into the shallow PQCs. In Figure 12(a), the tight alignment between the train and validation accuracy scores at mid and final epochs shows the reduced overfitting with a single quantum layer in shallow PQC_7. When experimented with two quantum layers in shallow PQC_8, the model saw slightly reduced validation performance in Figure 12(b) compared to Figure 12(a). With three quantum layers in

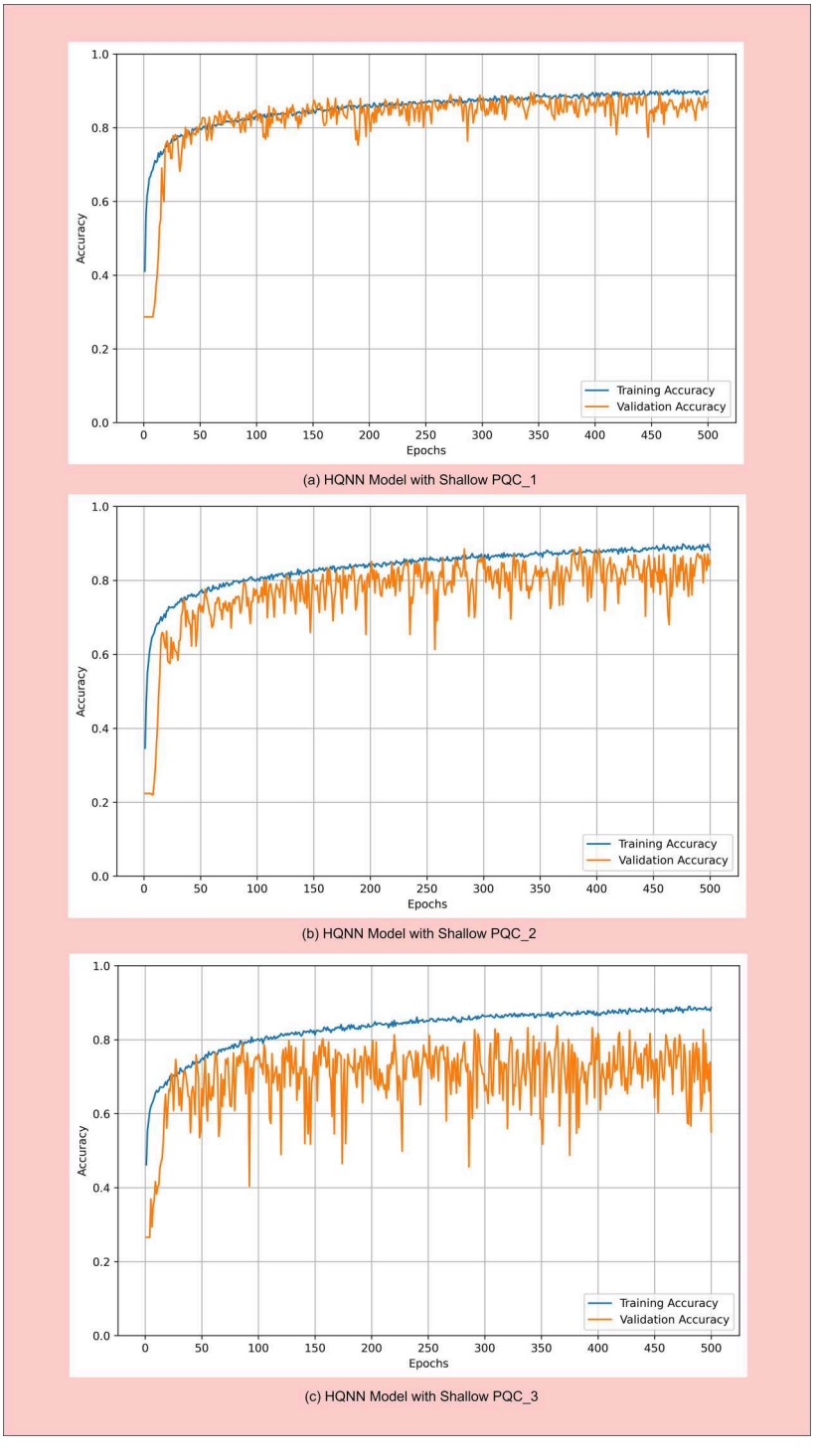

Figure 10. Performance of the proposed hybrid models in experiment A.

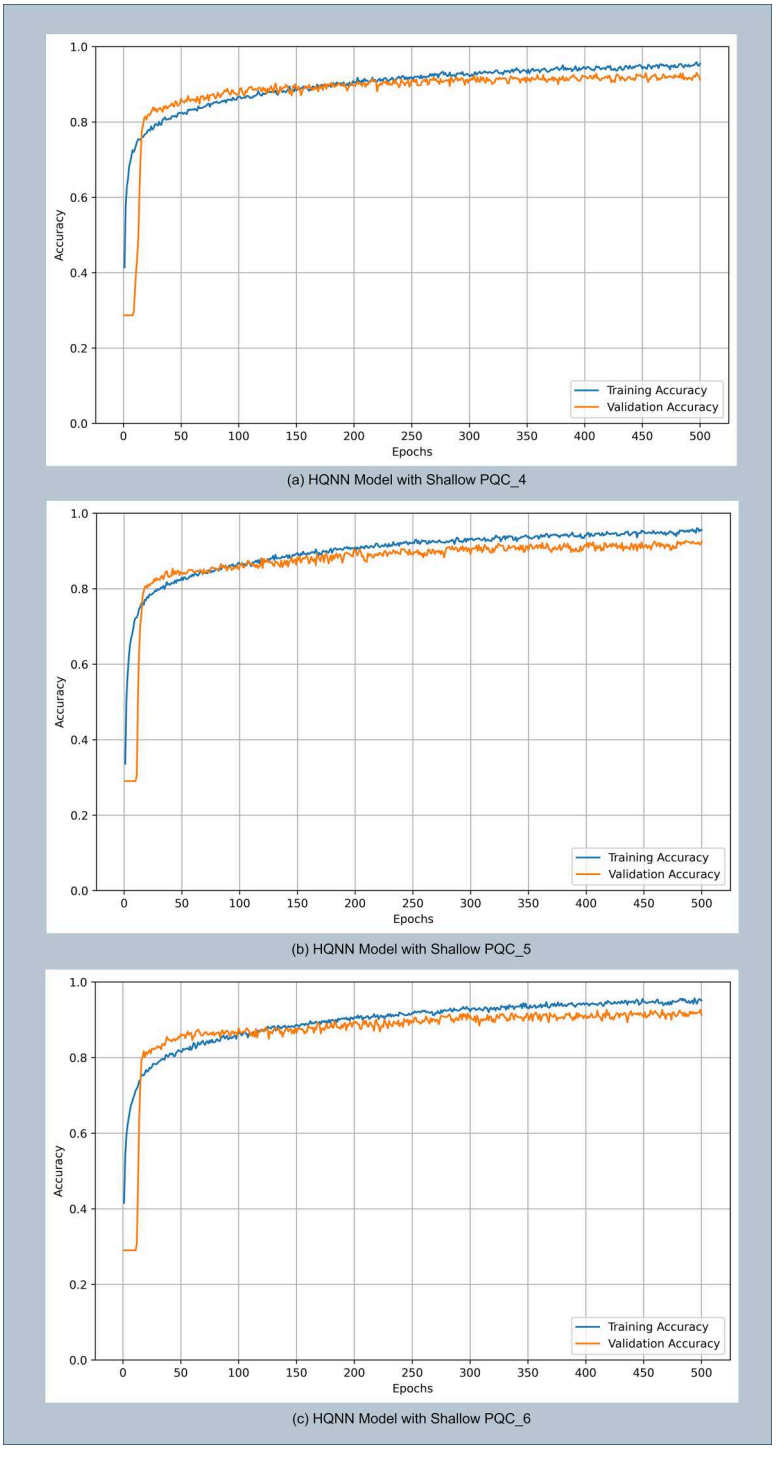

Figure 11. Performance of the proposed hybrid models in experiment B.

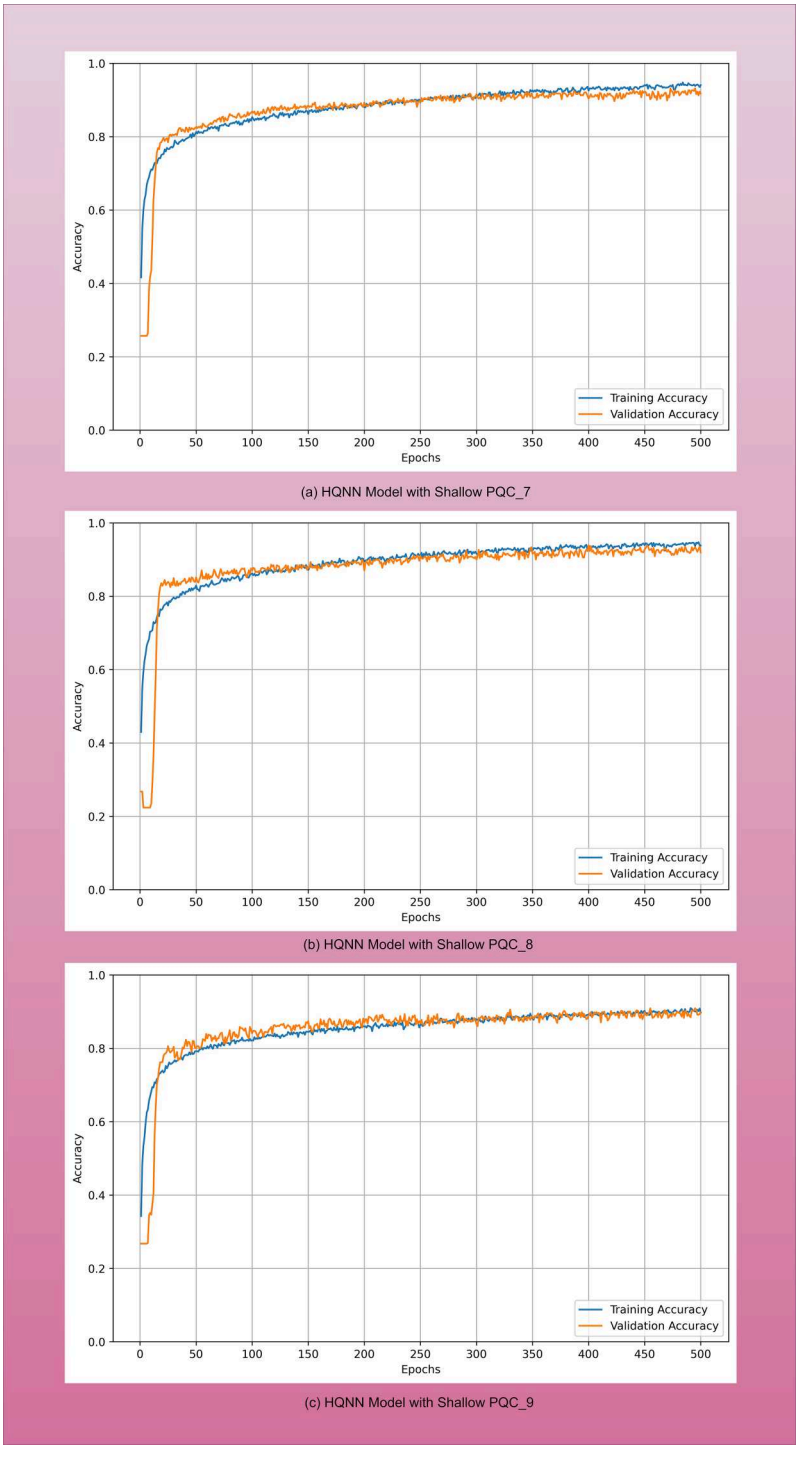

Figure 12. Performance of the proposed hybrid models in experiment C.

shallow PQC_9, both the training and validation accuracies showed a significant drop in Figure 12(c). Compared to single and two quantum layers, the shallow PQC with three quantum layers offered HQNN a strong generalisation but with reduced performance. Superposition enabled quantum parallelism and allowed the model to encode the features into a larger Hilbert space. The CZ entanglement enabled non-classical feature interactions with correlated qubits. The Single-layer shallow PQC with low circuit depth reduced the risk of vanishing gradients and avoided barren plateau. As the layers increased, the circuit was prone to barren plateau, which reduced the performance of the shallow PQC with three quantum layers. From the experiments, the proposed work realised that the shallow PQC_7 with R_X rotation, superposition, entanglement, and single quantum layer offers reliable MRI brain tumour classification performance with better generalisation on unseen data.

The improved HQNN1 performance on versatile MRI brain image datasets

From the experiments, the Improved HQNN1 architecture possesses the best combination of classical and quantum components for brain tumour diagnosis among the proposed classical and hybrid models. Hence, the performance of the model is validated and tested on three more datasets. We used the model to perform specific classification tasks on each dataset: i. Brain tumour type identification with four classes of images ii. Brain tumour type identification with three classes of images iii. Brain tumour detection with two classes of images. Table 8 shows the model's experimental results across different datasets for brain tumour diagnosis. From Table 8, the model's evaluation performance was excellent for binary classification, while it saw reduced performance as the number of classes increased. The MCC scores over 95% for two and three classes of images indicate the model's strong consistency in predicting the positive and negative classes correctly.

SOTA methods comparison

The proposed method is compared with recent state-of-the-art (SOTA) MRI brain tumour classification methods. The proposed HQNN model outperformed the existing classical and quantum models in standard MRI brain tumour datasets with better test accuracy, as shown in Table 9.

The SOTA methods in [69,82,83] were developed for four classes of MRI brain images. In [82], the authors extracted radiomics features from the brain images and trained traditional machine learning classifiers using them, where the KNN classifiers scored better with 91.1% accuracy on test data. In [69], the quantum convolutional layers extracted brain image features. A classical neural network layer further processed the extracted features, achieving 97.8% accuracy. In [83], Saeedi et al. developed an auto-encoder convolutional neural network architecture, where the auto-encoder network processed the brain images, and its output was fed to the convolutional network part for classification.

The methods in [32,56,60] were discussed in the related works section. In [84], the authors developed a lightweight MobileNet architecture with depth-wise separable blocks that achieved 96.95 test accuracy in classifying three classes of MRI brain images. In [85], Abbood et al. experimented with four standard deep learning architectures for brain tumour detection, where the RestNEt50 model outperformed the

Table 8. Dataset-specific experimental results of improved HQNN1 model.

Datasets									
Dataset Name	No. of Classes	Train Accuracy	Validation Accuracy	Test Accuracy	F1 Score	Precision	Recall	Specificity	MCC
Brain Tumour Classification (MRI) [79]	4	91.30	93.12	92.31	92.30	92.31	92.31	97.43	89.76
Brain Tumour Dataset [80]	3	95.47	97.23	96.97	96.98	96.99	96.97	98.5	95.46
Br35H:: Brain Tumour Detection 2020 [81]	2	98.46	97.22	98.17	98.17	98.17	98.17	98.15	96.32

Table 9. Performance comparison with SOTA methods.

Dataset	Authors	Method	Test Accuracy
Brain Tumour Classification Dataset [79]	Pattanaik, B et al. (2022) [82]	KNN classifier	91.1
	Dong, Y et al. (2023) [69]	Hybrid Quantum Classical Neural Network	97.8
	Saeedi, S et al. (2023) [83]	Convolutional autoencoder	90.92
	Proposed work	HQNN	92.31
Brain Tumour Dataset [80]	Khan, M. A. Z et al. (2024) [32]	Quantum Convolutional Neural Network	91.47
	Ticku, A., et al. (2025) [56]	Quantum Convolutional Neural Network	92.13
	Jetlin et al. (2025) [60]	Pyramid Quantum Dilated Convolutional Neural Network	94.1
	Khan et al. (2025) [84]	Modified MobileNet	96.95
	Proposed work	HQNN	96.97
Br35H Brain Tumour Detection 2020 [81]	Abbood et al. (2021) [85]	ResNet50	95.80
	Sadr et al. (2025) [86]	Finetuned-VGG16	97.14
	Mahesha (2023) [87]	Convolutional Neural Network	97.2
	Proposed Work	HQNN	98.17

remaining models with 95.80% accuracy. In [85], the authors combined the pre-trained VGG16 architecture with a customised deep CNN model that scored 97.14% accuracy. Mahesha developed a customised CNN architecture in [86] for binary classification of brain tumours, and the model achieved 97.2% test accuracy.

Discussion

The findings of the proposed work revealed that the R_X gate, as the variational parameter in PQCs, processed the quantum-encoded MRI brain features better than the R_Y and R_Z gates. R_X gate's X-axis transformations on the Bloch sphere are commonly used in quantum data encoding and qubit entanglement processes. R_X gates have proven to be more stable and effective in noisy environments. The proposed work encoded MRI brain image features into quantum states using R_X gates. When the R_X gate was applied as variational parameterisation in PQC, it better aligned with the data structure, facilitating more efficient quantum state manipulation.

The HQNN models required significantly more computational time than purely classical models. Simulating quantum operations on classical hardware is resource-intensive. The computational demand scales exponentially as the number of qubits and operations increases. This substantially strains classical processors, which must emulate each qubit's interactions and operations in detail. These hardware limitations might be reduced as quantum hardware becomes more accessible and efficient, potentially improving simulation speed and resource use.

The experimental results demonstrated the importance of superposition initialisation of qubits in stabilising the validation performance of the model. The experiments also revealed the combination of H-gate superposition and CZ entanglement in PQC with a single quantum layer is effective for generalisation of the proposed HQNN. The proposed work realised the effect of barren plateau in PQCs with the increased layer depth which reduced the performance of the HQNN model significantly.

Due to resource limitations, the proposed PQC architecture could use 10 qubits only. Hence the PCA features are limited to 10. Obtaining the optimal combination of quantum gates and choosing the layer depth are major challenges in designing the PQC. The proposed work performed a detailed empirical ablation study on HQNN models and figured out the advantages of quantum circuits with different gates and layers. However, the proposed ablation experiments are limited to MRI brain images, the proposed method can be fine-tuned and adopted to diverse image classification tasks.

With a quantum machine learning approach, the proposed work focused on identifying the primary brain tumour types, such as glioma, meningioma, and pituitary. The proposed quantum approach can be extended to radiogenomic prediction tasks for glioma brain tumours. The BraTS 2021 challenge dataset [88] introduced a task to predict the methylation status of the O6-methylguanine-DNA methyltransferase (MGMT) gene promoter directly from multi-parametric magnetic resonance imaging (mpMRI) scans. Qureshi et al. developed a two-stage process for radiogenomic classification of the MGMT promoter methylation status [89]. They created a deep learning architecture to extract latent features from the mpMRI scans and fused them with the radiomics features, forming a hybrid feature set. They trained a KNN classifier with these features set that achieved 96.94% test accuracy. Extending our proposed quantum approach to predicting MGMT promoter methylation status can aid in better treatment planning, as it is a crucial predictive biomarker of glioblastoma therapy.

Conclusion

The proposed work designed fifteen shallow PQCs and analysed their impact on HQNN models with various configurations. The classical features were encoded into quantum states using 10-qubit angle encoding circuits. The performances of the HQNN models were analysed through an ablation study. The ablation experiments showed the strong impact of R_X, H, and CZ gates in training the HQNN model without overfitting. The proposed work utilised the shallow PQC to mitigate the overfitting issue found in classical neural network models. The proposed HQNN model showed better generalisation than the classical FCNN models even with 0.1 dropout rate. The improved HQNN1 has demonstrated itself to be the most generalised and accurate model among all proposed architectures, with a stronger ability to generalise to new data than other

models. The experiments on PQCs with increased layer depths proved superior performance and strong generalisation of the HQNN model with the single-layer PQC. The proposed model has outperformed the SOTA models on three different standard MRI brain tumour datasets with 92.31%, 96.97%, and 98.17% test accuracy scores. In the future, a thorough analysis of the expressibility of the PQC in relation to model performance improvement will lead to more accurate MRI brain tumour diagnoses.

Disclosure statement

No potential conflict of interest was reported by the author(s).

Data availability statement

The datasets used for this work are openly available at the corresponding Kaggle and Figshare repositories.

References

[1] Q. Ostrom, M. Price, C. Neff, G. Cioffi, K. Waite, C. Kruchko, and J. Barnholtz-Sloan. CBTRUS statistical report: primary brain and other central nervous system tumors diagnosed in the United States in 2015-2019. Neuro-Oncology, 2022.

[2] S. Khalighi, K. Reddy, A. Midya, K.B. Pandav, A. Madabhushi, and M. Abedalthagafi, *Artificial intelligence in neuro-oncology: advances and challenges in brain tumor diagnosis, prognosis, and precision treatment*. NPJ Precision Oncology *8*(1) (2024), pp. 80.

[3] https://www.cancer.org/cancer/types/brain-spinal-cord-tumors-adults/detection-diagnosis-staging/how-diagnosed.html Tests for brain and spinal cord tumors in adults.

[4] M. Martucci, R. Russo, F. Schimperna, G. D'Apolito, M. Panfili, A. Grimaldi, A. Perna, A.M. Ferranti, G. Varcasia, C. Giordano, and S. Gaudino, *Magnetic resonance imaging of primary adult brain tumors: state of the art and future perspectives*. Biomedicines *11*(2) (2023), pp. 364.

[5] L. Sun, S. Zhang, H. Chen, and L. Luo, *Brain tumor segmentation and survival prediction using multimodal MRI scans with deep learning*. Front. Neurosci. *13* (2019), pp. 810.

[6] G. Katti, S.A. Ara, and A. Shireen, *Magnetic resonance imaging (MRI)–a review*. International Journal of Dental Clinics *3*(1) (2011), pp. 65–70.

[7] S.A. Qureshi, S.E.A. Raza, L. Hussain, A.A. Malibari, M.K. Nour, A.U. Rehman, Fahd N. Al-Wesabi, and A.M. Hilal, *Intelligent ultra-light deep learning model for multi-class brain tumor detection*. Appl. Sci. *12*(8) (2022), pp. 3715.

[8] R. Kaifi, *A review of recent advances in brain tumor diagnosis based on AI-based classification*. Diagnostics *13*(18) (2023), pp. 3007.

[9] G.S. Tandel, A. Balestrieri, T. Jujaray, N.N. Khanna, L. Saba, and J.S. Suri, *Multiclass magnetic resonance imaging brain tumor classification using artificial intelligence paradigm*. Comput. Biol. Med. *122* (2020), pp. 103804.

[10] R. Vankdothu and M.A. Hameed, *Brain tumor segmentation of MR images using SVM and fuzzy classifier in machine learning*. Measurement: Sensors *24* (2022), pp. 100440.

[11] A. Vidyarthi, R. Agarwal, D. Gupta, R. Sharma, D. Draheim, and P. Tiwari, *Machine learning assisted methodology for multiclass classification of malignant brain tumors*. IEEE. Access. *10* (2022), pp. 50624–50640.

[12] S. Kumar, S. Choudhary, A. Jain, K. Singh, A. Ahmadian, and M.Y. Bajuri, *Brain tumor classification using deep neural network and transfer learning*. Brain Topogr. *36*(3) (2023), pp. 305–318.

[13] T. Rahman and M.S. Islam, *MRI brain tumor detection and classification using parallel deep convolutional neural networks*. Measurement: Sensors *26* (2023), pp. 100694.
[14] N. Saranya and D.K. Renuka, *Brain tumor classification using convolution neural network*. J. Phys.: Conf. Ser. 1916(1) (2021, May), pp. 012206.
[15] L. Brunese, F. Mercaldo, A. Reginelli, and A. Santone, *An ensemble learning approach for brain cancer detection exploiting radiomic features*. Comput. Methods Programs Biomed. *185* (2020), pp. 105134.
[16] D. Xiao, Z. Zhao, J. Liu, X. Wang, P. Fu, J.M. Le Grange, J. Wang, X. Guo, H. Zhao, J. Shi, P. Yan, and X. Jiang, *Diagnosis of invasive meningioma based on brain-tumor interface radiomics features on brain MR images: a multicenter study*. Front. Oncol. *11* (2021), pp. 708040.
[17] M.Z. Zafar, S.M. Adnan, W. Ahmad, J. Ikram, and J. Rashid, *Brain tumor detection and classification using geometrical shapes as texture descriptors*. Techn J Univ Eng Technol Taxila *24*(1) (2019), pp. 83–89.
[18] B.H. Asodekar, S.A. Gore, and A.D. Thakare, *Brain tumor analysis based on shape features of MRI using machine learning*, 2019 5th International Conference on Computing, Communication, Control and Automation (ICCUBEA), 2019, September. (pp. 1–5). IEEE.
[19] M.R. Ismael and I. Abdel-Qader, *Brain tumor classification via statistical features and back-propagation neural network*, 2018 IEEE International Conference on Electro/Information Technology (EIT), 2018, May. (pp. 0252–0257). IEEE.
[20] J. Amin, M. Sharif, M. Raza, T. Saba, and M.A. Anjum, *Brain tumor detection using statistical and machine learning method*. Comput. Methods Programs Biomed. *177* (2019), pp. 69–79.
[21] A. Saboor, J.P. Li, A. Ul Haq, U. Shehzad, S. Khan, R.M. Aotaibi, and S.A. Alajlan, *DDFC: deep learning approach for deep feature extraction and classification of brain tumors using magnetic resonance imaging in E-healthcare system*. Sci. Rep. *14*(1) (2024), pp. 6425.
[22] S. Al-Otaibi, A. Rehman, A. Raza, J. Alyami, and T. Saba, *CVG-Net: novel transfer learning based deep features for diagnosis of brain tumors using MRI scans*. PeerJ Computer Science *10* (2024), pp. e2008.
[23] A. Ghosh, B. Soni, and U. Baruah, *Transfer learning-based deep feature extraction framework using fine-tuned efficientnet b7 for multiclass brain tumor classification*. Arab. J. Sci. Eng. *49*(9) (2024), pp. 12027–12048.
[24] X. Zhao, L. Wang, Y. Zhang, X. Han, M. Deveci, and M. Parmar, *A review of convolutional neural networks in computer vision*. Artif. Intell. Rev. *57*(4) (2024), pp. 99.
[25] A. Hatamizadeh, V. Nath, Y. Tang, D. Yang, H.R. Roth, and D. Xu, *Swin unetr: swin transformers for semantic segmentation of brain tumors in mri images*, in *International MICCAI Brainlesion Workshop*, A. Crimi, and S. Bakas, eds., Springer International Publishing, Cham, 2021, September. pp. 272–284.
[26] M.F. Almufareh, M. Imran, A. Khan, M. Humayun, and M. Asim, *Automated brain tumor segmentation and classification in MRI using YOLO-based deep learning*. IEEE. Access. *12* (2024), pp. 16189–16207.
[27] M.A. Ilani, D. Shi, and Y.M. Banad, *T1-weighted MRI-based brain tumor classification using hybrid deep learning models*. Sci. Rep. *15*(1) (2025), pp. 7010.
[28] W.J. Zhang, W.T. Chen, C.H. Liu, S.W. Chen, Y.H. Lai, and S.D. You, *Feasibility study of detecting and segmenting small brain tumors in a small MRI dataset with self-supervised learning*. Diagnostics *15*(3) (2025), pp. 249.
[29] F.R. Hencya, S. Mandala, T.B. Tang, and M.S.M. Zahid, *A Transfer Learning-Based Model for Brain Tumor Detection in MRI Images*, *Jurnal Nasional Teknik Elektro*, *12*(2) 2023, Bandung.
[30] L. Alzubaidi, J. Zhang, A.J. Humaidi, A. Al-Dujaili, Y. Duan, O. Al-Shamma, and L. Farhan, *Review of deep learning: concepts, CNN architectures, challenges, applications, future directions*. J. Big. Data. *8* (2021), pp. 1–74.
[31] N. Srivastava, G. Hinton, A. Krizhevsky, I. Sutskever, and R. Salakhutdinov, *Dropout: a simple way to prevent neural networks from overfitting*. The Journal of Machine Learning Research *15*(1) (2014), pp. 1929–1958.
[32] M.A.Z. Khan, N. Innan, A.A.O. Galib, and M. Bennai. Brain tumor diagnosis using quantum convolutional neural networks. *arXiv preprint arXiv:2401.15804*, 2024.

[33] de Paula Neto, F. M., Gustavo Filho, I. S., and Monteiro, C. A. (2020, July). Approaches to avoid overfitting in a quantum perceptron. In 2020 international Joint Conference on Neural Networks (IJCNN) (pp. 1–8). IEEE.
[34] J. Jiang, Y. Zhao, R. Li, C. Li, Z. Guo, B. Fan, and X. Zhang, *Strong generalization in quantum neural networks*. Quantum Inf. Process. *22*(12) (2023), pp. 428.
[35] M. Schuld and N. Killoran, *Quantum machine learning in feature Hilbert spaces*. Phys. Rev. Lett. *122*(4) (2019), pp. 040504.
[36] B. Matthew, S. Karkala, S. Hossain, M. Krishnapatnam, A. Aggarwal, Z. Zahir, and V. Shah. Quantum machine learning for material science simulations: opportunities and challenges, 2025.
[37] H.Y. Huang, M. Broughton, M. Mohseni, R. Babbush, S. Boixo, H. Neven, and J.R. McClean, *Power of data in quantum machine learning*. Nat. Commun. *12*(1) (2021), pp. 2631.
[38] D. Arthur and P. Date, *Hybrid quantum-classical neural networks*, 2022 IEEE International Conference on Quantum Computing and Engineering (QCE), 2022, September. (pp. 49–55). IEEE.
[39] M. Kashif and S. Al-Kuwari, *Demonstrating quantum advantage in hybrid quantum neural networks for model capacity*, 2022 IEEE International Conference on Rebooting Computing (ICRC), 2022, December. (pp. 36–44). IEEE.
[40] M. Kashif, E. Sychiuco, and M. Shafique, *Investigating the effect of noise on the training performance of hybrid quantum neural networks*, 2024 International Joint Conference on Neural Networks (IJCNN), 2024, June. (pp. 1–10). IEEE.
[41] X.B. Nguyen, H.Q. Nguyen, H. Churchill, S.U. Khan, and K. Luu, *Quantum visual feature encoding revisited*. Quantum Machine Intell *6*(2) (2024), pp. 61.
[42] M. Kashif, A. Marchisio, and M. Shafique. Computational advantage in hybrid quantum neural networks: myth or reality?. *arXiv preprint arXiv:2412.04991*, 2024.
[43] S. Barua, M. Rahman, S. Khaled, M.J. Sadek, R. Islam, and S. Siddique. QuXAI: explainers for hybrid quantum machine learning Models. *arXiv preprint arXiv:2505.10167*, 2025.
[44] J.R. McClean, S. Boixo, V.N. Smelyanskiy, R. Babbush, and H. Neven, *Barren plateaus in quantum neural network training landscapes*. Nat. Commun. *9*(1) (2018), pp. 4812.
[45] M. Cerezo, A. Sone, T. Volkoff, L. Cincio, and P.J. Coles, *Cost function dependent barren plateaus in shallow parametrized quantum circuits*. Nat. Commun. *12*(1) (2021), pp. 1791.
[46] S. Wang, E. Fontana, M. Cerezo, K. Sharma, A. Sone, L. Cincio, and P.J. Coles, *Noise-induced barren plateaus in variational quantum algorithms*. Nat. Commun. *12*(1) (2021), pp. 6961.
[47] K. Wada, R. Raymond, Y. Sato, and H.C. Watanabe, *Sequential optimal selections of single-qubit gates in parameterized quantum circuits*. Quantum Sci. Technol. *9*(3) (2024), pp. 035030.
[48] R. Meyes, M. Lu, C.W. de Puiseau, and T. Meisen. Ablation studies in artificial neural networks. *arXiv preprint arXiv:1901.08644*, 2019.
[49] S. Sheikholeslami, M. Meister, T. Wang, A.H. Payberah, V. Vlassov, and J. Dowling, Autoablation: automated parallel ablation studies for deep learning. In Proceedings of the 1st Workshop on Machine Learning and Systems (2021, April), pp. 55–61.
[50] M. Basthikodi, M. Chaithrashree, B.M. Ahamed Shafeeq, and A.P. Gurpur, *Enhancing multi-class brain tumor diagnosis using SVM and innovative feature extraction techniques*. Sci. Rep. *14*(1) (2024), pp. 26023.
[51] M.R. Shoaib, J. Zhao, H.M. Emara, A.S. Mubarak, O.A. Omer, F.E. Abd El-Samie, and H. Esmaiel, *Improving brain tumor classification: an approach integrating pre-trained CNN models and machine learning algorithms*. Heliyon *11*(10) (2025), e33471.
[52] S. Pal, R.P. Singh, and A. Kumar, *Analysis of hybrid feature optimization techniques based on the classification accuracy of brain tumor regions using machine learning and further evaluation based on the institute test data*. Journal of Medical Physics *49*(1) (2024), pp. 22–32.
[53] Y. Pande and J. Chaki, *Brain tumor detection across diverse MR images: an automated triple-module approach integrating reduced fused deep features and machine learning*. Res Eng. *25* (2025), pp. 103832.

[54] T. Felefly, C. Roukoz, G. Fares, S. Achkar, S. Yazbeck, P. Meyer, M. Kordahi, F. Azoury, D.N. Nasr, E. Nasr, G. Noël, and Z. Francis, *An explainable MRI-radiomic quantum neural network to differentiate between large brain metastases and high-grade glioma using quantum annealing for feature selection*. J. Digit Imaging *36*(6) (2023), pp. 2335–2346.
[55] T. Kumar, D. Kumar, and G. Singh, *Brain tumour classification using quantum support vector machine learning algorithm*. IETE. J. Res. *70*(5) (2024), pp. 4815–4828.
[56] A. Ticku, V. Sangwan, S. Balani, S. Jha, S. Rawat, A. Rathee, and D. Yadav, *Advancing neuroimaging with quantum convolutional neural networks for brain tumor detection*. Int. J. Inf. Technol. 17(9) (2025), pp. 5759–5766.
[57] E. Akpinar and M. Oduncuoglu. Beyond limits: charting new horizons in Glioma Tumor Classification through Hybrid Quantum Computing with The Cancer Genome Atlas (TCGA) Data. *Available at SSRN 4756044*, 2024.
[58] R. Choudhuri and A. Halder, *Brain MRI tumour classification using quantum classical convolutional neural net architecture*. Neural Computing and Applications *35*(6) (2023), pp. 4467–4478.
[59] M.S. Ullah, M.A. Khan, A. Masood, O. Mzoughi, O. Saidani, and N. Alturki, *Brain tumor classification from MRI scans: a framework of hybrid deep learning model with Bayesian optimization and quantum theory-based marine predator algorithm*. Front. Oncol. *14* (2024), pp. 1335740.
[60] C.P. Jetlin, *PyQDCNN: pyramid QDCNNet for multi-level brain tumor classification using MRI image*. Biomed. Signal. Process. Control. *100* (2025), pp. 107042.
[61] K.A.K.W. Dewage, R. Hasan, B. Rehman, and S. Mahmood, *Enhancing brain tumor detection through custom convolutional neural networks and interpretability-driven analysis*. Information *15*(10) (2024), pp. 653.
[62] P. Ganguly and A. Ghosh. Efficient brain tumor classification with lightweight CNN architecture: a novel approach. *arXiv preprint arXiv:2502.01674*, 2025.
[63] S.B. Son, H. Baek, and S. Park, *Effect of gate variations on MNIST classification in QNN: experimental study and analysis*. 한국통신학회논문지 *49*(2) (2024), pp. 254–263.
[64] C. Shorten and T.M. Khoshgoftaar, *A survey on image data augmentation for deep learning*. J. Big. Data. *6*(1) (2019), pp. 1–48.
[65] J.M. Johnson and T.M. Khoshgoftaar, *Survey on deep learning with class imbalance*. J. Big. Data. *6*(1) (2019), pp. 1–54.
[66] M. Rath and H. Date, *Quantum data encoding: a comparative analysis of classical-to-quantum mapping techniques and their impact on machine learning accuracy*. EPJ Quantum Technol. *11*(1) (2024), pp. 72.
[67] D. Ranga, A. Rana, S. Prajapat, P. Kumar, K. Kumar, and A.V. Vasilakos, *Quantum machine learning: exploring the role of data encoding techniques, challenges, and future directions*. Mathematics *12*(21) (2024), pp. 3318.
[68] P. Hu, Y. Li, R.S. Mong, and C. Singh, *Student understanding of the Bloch sphere*. Eur. J. Phys. *45*(2) (2024), pp. 025705.
[69] Y. Dong, Y. Fu, H. Liu, X. Che, L. Sun, and Y. Luo, *An improved hybrid quantum-classical convolutional neural network for multi-class brain tumor MRI classification*. J. Appl. Phys. *133*(6) (2023), pp. 064401.
[70] A. Wang, D. Mao, X. Li, T. Li, and L. Li, *HQNet: A hybrid quantum network for multi-class MRI brain classification via quantum computing*. Expert. Syst. Appl. *261* (2025), pp. 125537.
[71] C. Zhao and X.S. Gao, *QDNN: deep neural networks with quantum layers*. Quantum Machine Intelligence *3*(1) (2021), pp. 15.
[72] A. Senokosov, A. Sedykh, A. Sagingalieva, B. Kyriacou, and A. Melnikov, *Quantum machine learning for image classification*. Machine Learning: Science and Technology *5*(1) (2024), pp. 015040.
[73] M. Alam, S. Kundu, R.O. Topaloglu, and S. Ghosh, *Quantum-classical hybrid machine learning for image classification (iccad special session paper)*, 2021 IEEE/ACM International Conference On Computer Aided Design (ICCAD), 2021, November. (pp. 1–7). IEEE.

[74] Y. Trochun, S. Stirenko, O. Rokovyi, O. Alienin, E. Pavlov, and Y. Gordienko, *Hybrid classic-quantum neural networks for image classification*, 2021 11th IEEE International Conference on Intelligent Data Acquisition and Advanced Computing Systems: Technology and Applications (IDAACS), 2021, September. (Vol. 2, pp. 968–972). IEEE.
[75] M. Benedetti, E. Lloyd, S. Sack, and M. Fiorentini, *Parameterized quantum circuits as machine learning models*. Quantum Science and Technology *4*(4) (2019), pp. 043001.
[76] Y. Liu, K. Kaneko, K. Baba, J. Koyama, K. Kimura, and N. Takeda, *Analysis of parameterized quantum circuits: on the connection between expressibility and types of quantum gates*. IEEE Trans Quantum Eng. 6 (2025), pp. 1–12.
[77] S. Bravyi, D. Gosset, and R. König, *Quantum advantage with shallow circuits*. Science *362*(6412) (2018), pp. 308–311.
[78] Msoud Nickparvar. Brain tumor MRI dataset [Data set]. Kaggle. doi:10.34740/KAGGLE/DSV/2645886; dataset available at https://www.kaggle.com/datasets/sartajbhuvaji/brain-tumor-classification-mri, 2021.
[79] S. Bhuvaji, A. Kadam, P. Bhumkar, S. Dedge, and S. Kanchan. Brain tumor classification (MRI) [Data set]. Kaggle. doi:10.34740/KAGGLE/DSV/1183165; dataset available at https://www.kaggle.com/datasets/masoudnickparvar/brain-tumor-mri-dataset, 2020.
[80] J. Cheng. brain tumor dataset. figshare. Dataset. doi:10.6084/m9.figshare.1512427.v8; dataset available at https://www.kaggle.com/datasets/ahmedhamada0/brain-tumor-detection, 2017.
[81] Ahmed Hamada. Br35H:: Brain tumor detection 2020 [Dataset]. Kaggle. Available at https://www.kaggle.com/datasets/ahmedhamada0/brain-tumor-detection/data, 2020.
[82] B. Pattanaik, K. Anitha, S. Rathore, P. Biswas, P. Sethy, and S. Behera, *Brain tumor magnetic resonance images classification based machine learning paradigms*. Współczesna Onkologia *26*(4) (2022), pp. 268–274.
[83] S. Saeedi, S. Rezayi, H. Keshavarz, and R. Niakan Kalhori, *MRI-based brain tumor detection using convolutional deep learning methods and chosen machine learning techniques*. BMC Med. Inform. Decis. Mak. *23*(1) (2023), pp. 16.
[84] S.U.R. Khan, M. Zhao, and Y. Li, *Detection of MRI brain tumor using residual skip block based modified MobileNet model*. Cluster. Comput. *28*(4) (2025), pp. 248.
[85] A.A. Abbood, Q.M. Shallal, M.A. Fadhel, and Q.M. Shallal, *Automated brain tumor classification using various deep learning models: a comparative study*. Indonesian J. Electric. Eng. Comput. Sci. 22(1) (2021), pp. 252–259.
[86] H. Sadr, M. Nazari, S. Yousefzade-Chabok, H. Emami, R. Rabiei, and A. Ashraf, *Enhancing brain tumor classification in MRI images: a deep learning-based approach for accurate classification and diagnosis*. Image. Vis. Comput. 159 (2025), p. 105555.
[87] Y. Mahesha, *Identification of brain tumor images using a novel machine learning model*, in *International Conference on Information, Communication and Computing Technology*, G. Ranganathan, G. A. Papakostas, and Á. Rocha, eds., Springer Nature Singapore, Singapore, 2023, May. pp. 447–457.
[88] U. Baid, S. Ghodasara, S. Mohan, M. Bilello, E. Calabrese, E. Colak, and S. Bakas. The rsna-asnr-miccai brats 2021 benchmark on brain tumor segmentation and radiogenomic classification. *arXiv preprint arXiv:2107.02314*, 2021.
[89] S.A. Qureshi, L. Hussain, U. Ibrar, E. Alabdulkreem, M.K. Nour, M.S. Alqahtani, F.M. Nafie, A. Mohamed, G.P. Mohammed, and T.Q. Duong, *Radiogenomic classification for MGMT promoter methylation status using multi-omics fused feature space for least invasive diagnosis through mpMRI scans*. Sci. Rep. *13*(1) (2023), pp. 3291.

Philosophical Magazine

ISSN: 1478-6435 (Print) 1478-6443 (Online) Journal homepage: www.tandfonline.com/journals/tphm20

Quantifying the organisation in cancer cell partitioning noise

Mattia Miotto, Giovanna Peruzzi, Giorgio Gosti & Giancarlo Ruocco

To cite this article: Mattia Miotto, Giovanna Peruzzi, Giorgio Gosti & Giancarlo Ruocco (22 May 2025): Quantifying the organisation in cancer cell partitioning noise, Philosophical Magazine, DOI: 10.1080/14786435.2025.2502399

To link to this article: https://doi.org/10.1080/14786435.2025.2502399

PHILOSOPHICAL MAGAZINE
https://doi.org/10.1080/14786435.2025.2502399

Taylor & Francis
Taylor & Francis Group

Quantifying the organisation in cancer cell partitioning noise

Mattia Miotto [a], Giovanna Peruzzi[a], Giorgio Gosti [b] and Giancarlo Ruocco[a,c]

[a]Center for Life Nano & Neuro Science, Italian Institute of Technology, Rome, Italy; [b]Institute of Heritage Science, National Research Council (CNR-ISPC), Monterotondo, Italy; [c]Department of Physics, Sapienza University of Rome, Rome, Italy

ABSTRACT

Phenotypic heterogeneity in genetically identical cancer cell populations arises due to extrinsic and intrinsic sources of biological noise. In particular, partitioning noise, i.e. fluctuations in the cellular components during cellular division, is regarded as one of the major enhancers of phenotypic variability as such fluctuations can lead to dramatic changes in the cell state and thus to transitions between different phenotypes. The resulting plasticity increases the heterogeneity of tumors and changes their ability to resist treatments. Here, we show how to quantify the extent of fluctuations in the partitioning of different cellular components during the division of human leukemia cells. In particular, comparing the outcomes of a multi-fluorescent stain experiment with the predictions of a minimal statistical model, we found that a correlated binomial statistic explains the partition of cell cytoplasm and mitochondria together with their observed correlations. In perspective, our model can be applied to study the organisation in the partitioning of a wide range of cellular components paving the way to a better understanding of noise-driven cellular processes.

ARTICLE HISTORY
Received 19 June 2024
Accepted 2 April 2025

KEYWORDS
Partitioning noise; phenotypic heterogeneity; cancer cells; correlated binomial distribution; mathematical model

1. Introduction

Partitioning (or inheritance) noise is an umbrella term enclosing the variegate and complex set of molecular processes resulting in fluctuations of the cellular components, inherited by daughter cells after division [1]. Together with other sources of stochasticity coming from e.g. the gene expression/regulation machinery and from fluctuations in the growth/division processes [2], such biological noise contributes to creating and sustaining phenotypic heterogeneity of non-genetic origin in cellular populations [3–6]. While most of the research efforts up to now have been devoted to studying gene expression noise and fluctuations in cell cycle duration [2,7], several pieces of evidence showed

CONTACT Mattia Miotto mattia.miotto@roma1.infn.it Center for Life Nano & Neuro Science, Italian Institute of Technology, Viale Regina Elena 261 Rome, Italy

that under specific cases, noise in the segregation of cell components may be the dominant contribution [7].

Experiments to quantify partitioning noise rely mainly on timelapse microscopy imaging of fluorescently labelled cells at division [8,9]. This allows tracking the segregation of the cell elements, at the cost of requiring large sets of division events. Recently, we developed a protocol based on flow cytometry and cell sorting. Live-cell fluorescent dyes were used to mark representative cellular compartments (e.g. cytoplasm, mitochondria, and membrane), and the proliferation of the population together with the partitioning of the fluorescent markers between daughters cells were followed via flow cytometry measurements [10]. Using a flow cytometer, our method permits the simultaneous acquisition of both fluorescent signals associated with the used dyes and of the intensity of the forward scattered light, that provides a proxy for the cell size [11].

Analyzing the dynamics of the fluorescence intensity at different time points during the proliferation of the cell population (see Methods for details), we found that the partition statistics of cytoplasm, mitochondria, and membrane in Jurkat T-cell were compatible with biased Bernulli processes [10]. Notably, the simultaneous acquisition of the fluorescent signals of all the used dyes permitted the quantification of the correlation in the partitioning of the markers. Preliminary analyses showed that the observed correlations were not compatible with uncorrelated binomial processes, vouching for the presence of coupled fluctuations.

Here, we sought a model of correlated partitioning to quantify the observed covariance in the partitioning of couples of cellular components. We first derived analytical approximated expressions for the covariance of random variables that stochastically halved while cells proliferate. Next, we performed a set of proliferation experiments on populations of Jurkat T-cells to demonstrate the validity of our approach to extract information about the organisation in the partitioning of cytoplasmic molecules and mitochondria during division. Comparing the experimental results with the prediction of the correlated bivariate binomial model, we found that mitochondria and cytoplasmic material are partitioned with a positive correlation between daughter cells. Our experimental and theoretical apparatus can be readily applied to measure correlation in the partitioning of different cellular elements and cell types.

2. Results

2.1. Model for correlated partitioning noise

Along the line of Peruzzi *et al.* [10], we aim to develop a minimal model for the inheritance of cellular components able to account for correlation in the

segregation of two given components. Given a cell population having an initial distribution of labelled components, $P_0(x_1, x_2)$ (where x_1, and x_2 can be any two cellular elements whose partitioning we want to follow), each division event will result in the creation of two daughter cells, each carrying a fraction of the labelled components present in the mother cell. Taking a snapshot of the distribution of the marked components at a certain time, t, after the labelling procedure, the distribution will be given by:

$$P_t(x_1, x_2) = \sum_g \omega_g(t) P_g(x_1, x_2) \tag{1}$$

where P_g is the distribution of marked components of the cells that divided g times since the start of the experiments (i.e. being of generation g with respect to the initial cells that are considered as the generation zero) and $\omega_g(t)$ is the relative fraction of cells that divided g times at time t, with $\sum_g \omega_g(t) = 1$ for each time. We assume that cell division times do not depend on the number of marked components. Supposing no loss of labelled components (i.e. fluorescence) in the division process, the distribution composed by daughter cells is expected to have half the mean of the mother one. Thus, starting from an initial population with a sufficiently narrow variance, we could identify the different generations and measure their moments. In particular, we are interested in the covariance of x_1 and x_2 as a function of the generations:

$$\sigma_g(x_1, x_2) = E[x_1 x_2]_{P_g} - E[x_1]_{P_g} E[x_2]_{P_g} = \int \mathrm{d}x_1 \mathrm{d}x_2 (x_1 x_2 - < x_1 >_g < x_2 >_g) P_g(x_1, x_2) \tag{2}$$

where $E[x]_{P_g} = < x >_g$ represents the average of the stochastic variable x given its probability distribution $P(x)_g$. To make analytical progress, we start by noting that the population of cells of a certain generation, g, is given by the superposition of 2^g sub-populations, which can be associated with the sequence of an inherited fraction of marked components: for instance, the first generation of cells is composed by two sub-populations, the daughter cells that inherited fractions p_1 and p_2 of the x_1 and x_2 elements possessed by the mother cells and those that got the remaining $(1 - p_1)$ and $(1 - p_2)$ portions. The second generation is composed of four sub-populations and so on (see Figure 1(a) for a sketch). It is straightforward to show that:

$$\sigma_g(x_1, x_2) = \left(\frac{1}{2}\right)^g \sum_{k=1}^{2^g} \left(\sigma_g^k(x_1, x_2) + < x_1 >_g^k < x_2 >_g^k\right) - < x_1 >_g < x_2 >_g \tag{3}$$

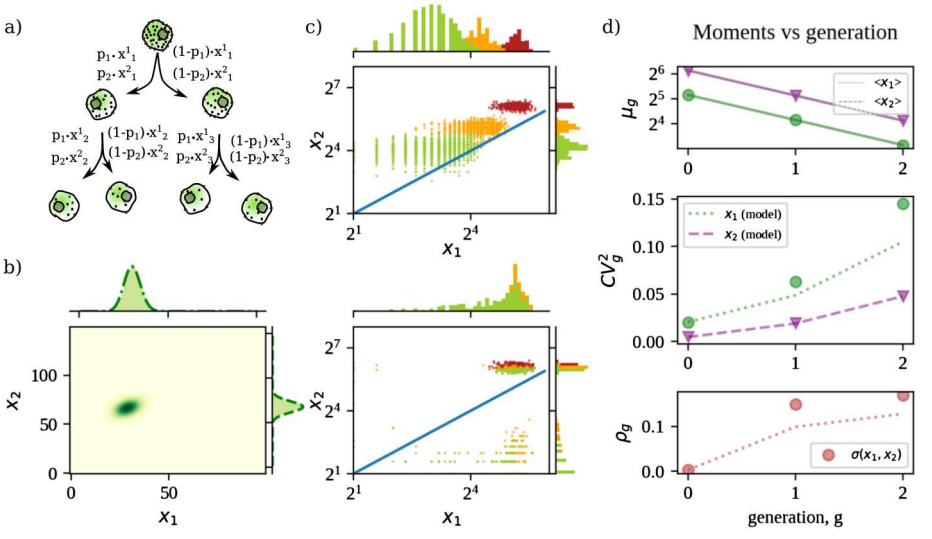

Figure 1. Correlated bivariate binomial model. (**a**) Schematic representation of the partitioning of two cellular components during a cell division process: at each division, the components x_i^1 and x_i^2 are divided between the two daughter cells, one inheriting fractions p_1 and p_2 of the mother components, while the other the remaining amounts. (**b**) Probability distribution of inheriting a set (x_1, x_2) of components from a mother cell having components $X_1 = 70$, $X_2 = 150$. Marginal distributions are represented as green-shaded curves on the top and right sides of the colormap. (**c**) Scatter plot representation of the proliferation of an initial population of cells (red), where each cell of the starting population divides two times, producing generation 1 (orange) and 2 (green). Marginal distributions are shown on the top and right sides. (**d**) From top to bottom, comparison between cell distribution mean, coefficient of variation, and Pearson correlation as a function of the generation obtained via numerical simulations (panel c) and from analytical results (Equations 4,3).

and

$$< x >_g = \left(\frac{1}{2}\right)^g \sum_{k=1}^{2^g} < x >_g^k \tag{4}$$

Using the laws of total expectation and variance, we can express each term in the summations as functions of previous generations. In fact,

$$< x >_g^{(p)} = \int \mathrm{d}x x P_g^{(p)} = \int \mathrm{d}y \int \mathrm{d}x x P(x|y, p) P_{g-1}(y) \tag{5}$$

and, similarly,

$$\sigma_g^{(p)}(x_1, x_2) = < \sigma(x_1, x_2|y_1, y_2) >_{g-1} + \sigma(< x_1|y_1 >, < x_2|y_2 >)_{g-1} \tag{6}$$

It remains to explicit a functional form for the transition probability, $P(x_1, x_2|y_1, y_2, p_1, p_2)$ and its marginals, $P(x_1|y_1, p_1)$ and $P(x_2|y_2, p_2)$. Peruzzi *et al.* [10] found that the marginal probabilities are well approximated by binomial distributions having $p_1 \sim 0.42$ and $p_1 \sim 0.50$ for mitochondria and

cytoplasmic elements, respectively (see Figure 1(a)). Thus, we opted for the bivariate binomial distribution proposed by Biswas and Hwang [12] (see Figure 1(b)):

$$P(x_1, x_2|y_1, y_2, p_1, p_2, \alpha) = \binom{y_1}{x_1} p_1^{x_1} (1-p_1)^{(y_1-x_1)} f(x_2|x_1) \tag{7}$$

where

$$f(x_2|x_1) = \frac{1}{(1+\alpha)^{y_1}} \sum_{j_1,j_2,j_3} \binom{x_1}{j_1}\binom{y_1-x_1}{j_2}\binom{y_2-y_1}{j_3} N_1 N_2 N_3 \tag{8}$$

with $N_1 = (p_2 + \alpha(p_2 - p_1) + \alpha)^{j_2}$, $N_2 = (1 - p_2 - \alpha(p_2 - p_1))^{(x_1-j_1)}(p_2 + \alpha(p_2 - p_1))^{j_2}$, and $N_3 = (1 - p_2 - \alpha(p_2 - p_1) + \alpha)^{(y_1-x_1-j_2)} p_2^{j_3} (1-p_2)^{(y_2-y_1-j_3)}$. Such distribution is defined for $y_1 < y_2$ and has the following properties: (i) it has binomial distributed marginals and (ii) produces couples of stochastic variables whose correlation depends on the parameter α. The latter modulates the covariance in the sampled components as $\sigma(x_1, x_2) = y_1(\frac{\alpha}{1+\alpha})p_1(1-p_1)$.

Using Equations (7), (5) reduces to $< x >_g^{(p)} = p_1 < x >_{g-1}^{(p)}$, while Equation (6) can be recast as:

$$\begin{aligned} \sigma_g^{(p)}(x_1, x_2) &= \mathcal{A} < y_1 >_{g-1}^{(p)} + p_1^2 p_2^2 \sigma_{g-1}^{(p)}(y_1, y_2) \quad \text{with} \\ \mathcal{A} &= \frac{\alpha}{1+\alpha} p_1(1-p_1), \end{aligned} \tag{9}$$

where we assumed that the probability of finding a cell having a number of marked elements $x_1 > x_2$ is vanishingly small.

Plugging the obtained expressions for the means and covariances of the subpopulations in Equation (3) and doing some straightforward calculations (see Methods), one gets an expression for the covariance as a function of the generations that depends on the means and covariance of the starting distribution, and the three parameters of the bivariate binomial model:

$$\sigma_g(x_1, x_2) = \mathcal{A}\mu_1^0 \left(\frac{1}{2}\right)^{g-1} \left(\frac{1-(2\mathcal{B})^g}{1-2\mathcal{B}}\right) + \mathcal{B}^g(\sigma_0 + \mu_1^0\mu_2^0) - \left(\frac{1}{2}\right)^{2g} \mu_1^0\mu_2^0 \tag{10}$$

with $\mathcal{B} = \frac{p_1p_2 + (1-p_1)(1-p_2)}{2}$. From Equation (10), we can finally get to the expression for the Pearson coefficient as $\rho[x_1, x_2] = \frac{\sigma_g(x_1, x_2)}{\sqrt{\sigma_g(x_1, x_1)\sigma_g(x_1, x_1)}}$.

2.2. Role of the model parameters on the observed correlation

The obtained expression for the Pearson correlation depends on the initial means and covariance and the three parameters defining the bivariate binomial model, i.e. the partition biases p_1 and p_2, and the α parameter. In Figure 2, we explored the behaviour of the generation correlation upon varying these

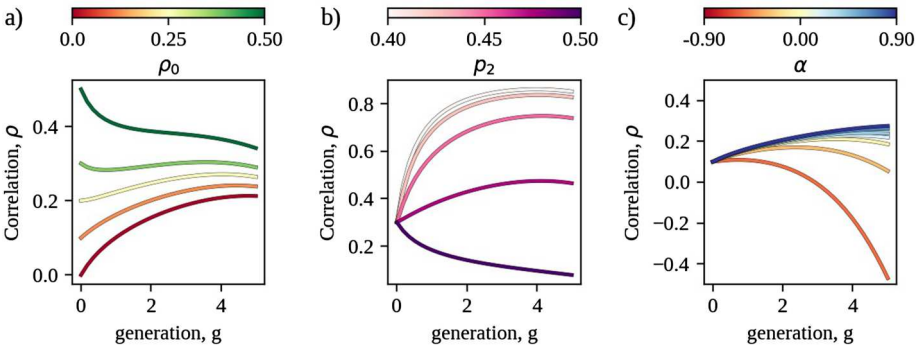

Figure 2. Correlation dependence on model parameters. (**a**) Pearson correlation as a function of the generation upon varying the correlation of the initial population. (**b**) Same as in panel (a) but upon varying p_2. (**c**) Same as in panel (a) but for different values of the bivariate binomial α parameter.

parameters. In particular, Figure 2(a) displays the Pearson correlation as a function of the cell generations for different values of the initial correlation while keeping all other parameters fixed. Given the initial value, the correlation showed by the subsequent subpopulations can be higher or lower than the initial one depending on the binomial parameter. This can be seen by looking at the behaviour of the correlation upon variation of the partition parameters. As shown in Figure 2, fixing p_1 to 0.4 and varying p_2, one can see that the correlation in the subsequent generations reaches higher values for $p \leq 0.45$, while it drops to zero in case of symmetric division ($p_2 = 0.5$). Interestingly, the correlation reaches negative values for $p_2 > 0.5$. This happens because the bivariate binomial partition tends to introduce an overall correlation in the divided daughter cell population whenever the partition is not symmetric (p_1 and $p_2 = 0.5$). The population of cells in each generation is given by the superposition of the two subpopulations composed of the daughter cells produced by the division of the mother cells of the previous generation: if both p_1 and p_2 are lower than 0.5 the division will produce a positively correlated distribution of daughter cells since those that inherited fractions (p_1, p_2) of the mother components will have lower components with respect to their sisters' subpopulation that inherited fractions ($1 - p_1$, $1 - p_2$). If instead, the bias is higher than 0.5, one subpopulation will have a higher number of one component (say component 1) and lower numbers of component 2, while for the subpopulation of their sisters will be the opposite, resulting in an overall anticorrelated daughter distribution. Notably, this behaviour arises even if the is no correlation in the partitioning of the components inside each subpopulation of cells belonging to the same generations. (i.e. $\alpha = 0$). Finally, Figure 2c shows the generation correlation for different values of the α parameter in the range $(-0.9, 0.9)$, i.e. for negatively to positively correlated subpopulations (see the example in Figure 1(b)), while other parameters are kept fixed. Depending on the choice

of the remaining parameters, a stable positive correlation is observed for $\alpha = 0$. If $\alpha > 0$, the observed positive correlation progressively increases, doubling the values shown at $\alpha = 0$ for distant generations (g>3).

2.3. Use of fluorescence as a proxy for copy numbers

Equation (3) describes the expected behaviour of the covariance between two kinds of marked cell components as they get diluted after each division event according to Bernoulli statistics. From an experimental viewpoint, cellular components are marked via specific fluorescent dyes that bind to the components. The experimental readout is the total fluorescence intensity of each cell, $\mathcal{I}$. In the regime where sample auto-fluorescence is negligible, $\mathcal{I}$ is assumed to be proportional to the number of marked elements, $\mathcal{I} \propto f \cdot N$, with f being a scaling factor linked to both the used dyes and experimental setup. Equation (10) depends on the first and second moments of the initial distributions of the marked cellular components. In terms of measured intesities, we have $\tilde{\mu}_i^0 = f\mu_i^0$ and $\tilde{\sigma}_0(\tilde{x}_i, \tilde{x}_j) = f^2\sigma_0(x_i, x_j)$ with $i, j \in (1, 2)$ for the first and second moments, respectively. Due to the presence of the first term of Equation (10), the covariance of the marked elements at g>0 is not simply proportional to that of the measured intensity. Thus, the effect of the scaling factor can not be eliminated e.g. by simply considering ratios like σ_g/σ_0. To probe the consequences of this aspect on our capability to extract information from the data, we studied the behaviour of measured signals assuming different scaling factors. Figure 3 shows the variance of one marker as a function of the generations varying f up to three orders of magnitude. The four panels correspond to different choices of the Coefficient of Variation of the initial marked distribution, $CV = \sqrt{(\sigma_0/\mu_0^2)}$ and the segregation bias, p. As one can see from Figure 3(a), the overall trend of the variance is preserved for different choices of the scaling factor. The values of the normalised variance are within the typical experimental error associated with such measurements. As p gets closer to 0.5, i.e. to symmetric division, the scaling factor required to have well-defined variance trends increases to about 100 for the same value of the initial Coefficient of Variation (CV). Changing the initial variance to mean ratio, one can use Equation (3) with fluorescence signals even for compounds present in tens of copy numbers per cell or having low scaling factors.

2.4. Simultaneous measure of component partitioning via kinetics flowing experiments

Along the line of Peruzzi *et al.* [10], we performed a live-cell experiment using Jurkat T-cell, a leukemia cell line. In particular, we used CellTrace™ Violet stain (CTV) and MitoTracker® Green FM (MITO) as fluorescent tags for

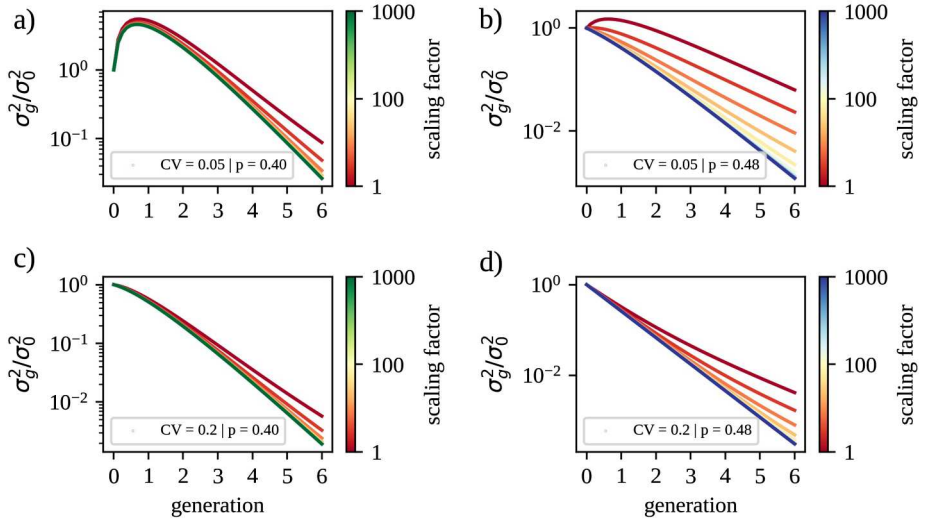

Figure 3. Scaling behaviours. (**a**) Variance of the components distribution of cells in the same generation as a function of the generations. The initial population has a mean of 100 compounds, a Coefficient of Variation of 0.05, and divides according to a binomial model with $p = 0.40$. Different plots are obtained rescaling the initial population distribution by a factor f in the interval $1-10^3$. (**b**) Same as in panel (a) but for $p = 0.48$. (**c**) Same as in panel (a) but for $CV = 0.2$ (**d**) Same as in panel (b) but for $CV = 0.2$.

cytoplasm and mitochondria, respectively. As described in both Methods and Ref. [10], we first sorted cells to select an initial population having the desired distribution, i.e. we selected cells displaying a CTV fluorescence signal higher than the MITO one and set the gating strategy to have CV lower than 0.5 for both channels. Monitoring the evolution of the distribution of the marker in time, we obtained the dynamics shown in Figure 4(a). In particular, each grey dot in the scatter plots corresponds to a cell for which both CTV and MITO fluorescences have been acquired. Comparing the snapshots taken at 0, 18, 24, and 36 h, one sees that the initial distribution is formed by one peak, while after 18 h two peaks are distinguishable, one located approximately at the same position as the one found at time zero, and another having half the mean of the other for both markers. The newly formed peak is composed of all cells that have been divided once since the start of the experiment. At 24 h, there are still two peaks, whose relative weights are dominated by the generation 1 subpopulation; finally, after 36 h, four subpopulations can be identified. To quantitatively assign each cell to one subpopulation, we performed a Gaussian Mixture clustering as described in the Methods, which identified the distributions shown in the top and right plot of Figure 4(a) and as coloured ellipsoids in the panels.

2.5. Analysis of cytoplasmic and mitochondria partitioning

Via the Gaussian Mixture fitting, we quantified the first two moments (mean, and covariance) of the distribution of the inherited fluorescence intensity for each

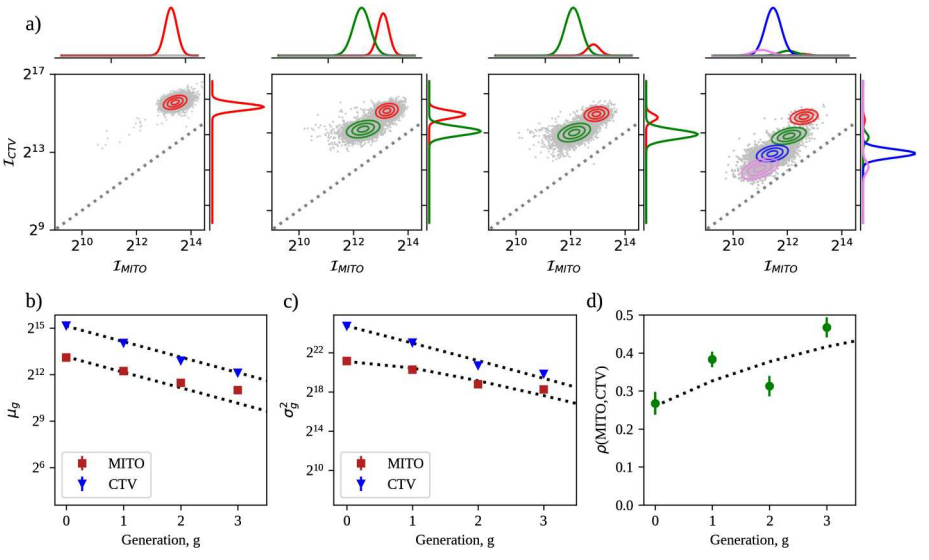

Figure 4. Experimental data vs model predictions. (**a**) Dot plot of the intensity of MITO vs CTV, measured at different times (hours) in one of the three experiments with simultaneous MITO and CTV markers. Gaussian Mixture fit is represented with different colours corresponding to different generations. (**b**) Mean value of the intensity of the fluorescent markers as a function of the generations, obtained through the Gaussian Mixture procedure (points) and as the best fit of Equation (4) (dotted line). Dark blue triangles and red squares correspond to the mean of the intensity for CTV and MITO, respectively. (**c**) Same as in (b) but for the intensity variances. (**d**) Pearson correlations between the MITO and CTV intensities as a function of the generations. Green dots represent the mean correlation for each generation, while the dotted line shows the best fit of Equation (10).

generation of cells and compared them with the predictions of our model. In particular, Figure 4(b) shows the mean fluorescence intensity for cytoplasm (blue triangles) and mitochondria (red squares) markers as a function of the observed generations. The dotted lines represent the best fits for the two marker types using Equation (4). Indeed, the means halves at each generation, starting from their initial values of $\mu_2^0 = 8700 \pm 100$ and $\mu_2^0 = 35,200 \pm 500$. Similarly, Figure 4(c) reports the variance of the fluorescence intensity for cytoplasm (blue triangles) and mitochondria (red squares) markers as a function of the observed generations, while the Pearson correlation between CTV and MITO (green dots) is displayed in Figure 4(d). The best fit (dotted lines) of Equation (3) for both variances and covariance is obtained for $\sigma_1^0 = 5300 \pm 200$, $p_1^0 = 0.42 \pm 0.01$, $\sigma_2^0 = 3600 \pm 200$, $p_2^0 = 0.49 \pm 0.01$, $\sigma_{12}^0 = 4200 \pm 100$, and $\alpha = 0.1 \pm 0.1$. Note that the best-fit parameters are those yielding the minimum of the residual of the three independent terms of the covariance when considered simultaneously.

3. Discussion

Coupled inheritance of cellular phenotypes, like growth rate and cell cycle duration, have been suggested as the minimal ingredient for explaining non-trivial

behaviours shown by cell populations, like correlation across lineages, memory of previous generations, and responses to environmental stress [13–17]. From a physics point of view, the state of a cell, i.e. its manifested phenotype, can be represented by the numbers of all species of molecules present inside the cell. In this framework, observed phenotypes are stable states in the dynamics of the interaction network that comprises all these molecular species. Phenotypes can change in response to e.g. external stimuli triggering transitions to different stable states [5,18,19]. Apart from external stimuli, transitions can be driven also by fluctuations in the levels of certain cell fate-determinant molecules due to stochasticity in the process of cell growth and division [20,21]. In particular, both division and partitioning noises can provoke such phenotypic transitions depending on the extent of the produced fluctuations [22]. Asymmetric division of cell fate determinants is a well-established mechanism for cell differentiation during development as biased segregation of older compounds is often used by bacteria to obtain rejuvenation of the population [23]. Organisation in the partitioning fluctuations may serve cells as an additional layer of control to drive phenotypic transitions.

Here, we showed how the experimental protocol introduced by Peruzzi *et al.* [10] can be used to quantify the extent of noise in the partitioning of cellular components and its correlation. In particular, we first derived an analytical expression for the covariance of the inherited cellular elements as a function of the generations in the assumption that the division process obeys correlated Bernoulli statistics. Exploring the behaviour of the correlation as a function of the model parameters, we showed that a nontrivial trend emerges as a function of the two binomial biases, p_1 and p_2, without the need for directly correlated sub-population of cells ($\alpha = 0$). Using live-cell fluorescent dyes able to selectively mark cell cytoplasm and mitochondria, we measured the simultaneous dilution of CTV and MitoTraker during the proliferation of a population of Jurkat T-cells. Quantifying the correlation between the fluorescence intensity of the two dyes in different generations, we were able to compare experimental data with the prediction of the bivariate binomial model. Our results show that the observed correlation is explained if (i) cell cytoplasm is partitioned with a p of ~ 0.49, while (ii) mitochondria are divided asymmetrically with a bias of $p \sim 0.42$ and (iii) the partitions are -weakly- coupled by a binomial correlation coefficient of $\alpha \sim 0.1$. Notably, correlation in the presence of one symmetrically dividing element continuously diminishes to zero. Thus, monitoring the correlations allows for a refinement in the determination of the segregation bias of each cellular element. Overall, our method may serve as a valuable tool for delving into the complexities of cellular organisation and shedding light on the mechanisms influencing phenotypic outcomes across successive generations. The found direct coupling between the partitionings may reflect the presence of geometrical/spatial constraints during the division process, dictated for instance by the overall size of the cell [9], which are worthy of further

investigations. In conclusion, we showed how population-level, flow cytometry-based measurements can be readily applied to quantify the partitioning organisation of cellular elements. This opens up opportunities for understanding the nontrivial processes, like the long-range correlations observed in the phenotypes of distant generations within mammalian cell lineages.

4. Materials and methods

4.1. Cell culture

E6.1 Jurkat cells were used as a cell model for proliferation study and maintained in RPMI-1640 complete culture media containing 10% FBS, penicillin/streptomycin plus glutamine at 37 °C in 5% CO_2. Cells were passaged 2 times prior to amplification for the experiment. Cells were then harvested, counted, and washed twice in serum-free solutions and re-suspended in pre-warmed PBS for further staining.

4.2. Cells fluorescent dye labelling

To monitor cell proliferation through dye dilution, indicating the daughter progeny post a completed cell cycle, cells were subjected to staining with CellTrace™ Violet stain and MitoTracker® Green FM following the manufacturer's instructions. The employment of two distinct cell markers, representing cytoplasm and mitochondria, enabled a multi-variable analysis of proliferation. In each experiment, Fixable Viability Stain 780 (FVS780) was utilised to assess cell viability and confirm low dye toxicity.

CTV dye (C34557, Life Technologies, Paisley, UK), commonly used for monitoring multiple cell generations, was used as per the manufacturer's instructions. Complete media was introduced to the cell suspension for an additional 5-min incubation before the final wash in PBS. MitoTracker® Green FM (M7514, Molecular Probes, Eugene, USA), a green-fluorescent mitochondrial stain, was used at a concentration of 20 nM (stock 20 μM in DMSO) in PBS for 30 min in a water bath at 37^{o}C, with mixing every 10 min. The cells were then washed once in PBS. The live/dead staining, Fixable Viability Stain 780 (565388, BD Biosciences, San Jose, USA), was performed with a 1/1000 dilution in PBS for 10 min at RT. For each experiment, a new aliquot of the viability marker was used.

4.3. Cell sorting

Jurkat cells labelled with dyes underwent sorting using a FACSAriaIII (Becton Dickinson, BD Biosciences, USA), which was equipped with Near UV 375nm, 488nm, 561nm, and 633nm lasers and operated with FACSDiva software (BD

Biosciences version 6.1.3). Data analysis was conducted using FlowJo software (Tree Star, version 9.3.2 and 10.7.1).

In the analysis workflow, cells were initially gated on live cells based on viability dye exclusion, followed by exclusion of doublets using morphology parameters-both side and forward scatter, area versus width (A versus W). The unstained sample served as a reference to establish background fluorescence for each channel. For each fluorochrome, a sorting gate was established around the maximum peak of fluorescence of the dye distribution [24]. This approach ensured that the collected cells were enriched for the highest fluorescence intensity across all the markers used as per the experimental setup, including CellTrace and/or MitoTracker.

Subsequent to isolation, a portion of the sorted cells were reanalysed on the same instrument to assess post-sorting purity and population width. The results demonstrated an enrichment exceeding 99% for each sample.

4.4. Cell culture for dye dilution assessment

The sorted cell population was plated in a single well of a 6-well plate (BD Falcon) at a density of approximately 1×10^6 cells per well and maintained in culture for a duration of up to 72 h. To track multiple cell divisions, samples of the cell population were analysed at intervals of 18, 24, 36, 48, 60, and 72 h using the LSRFortessa flow cytometer. To establish the kinetic time zero, a small aliquot of the sorted cells was promptly analysed at the flow cytometer prior to culturing. The unstained sample served as a reference for setting background fluorescence, as described previously. Upon each collection of cells for analysis, an equivalent volume of fresh media was replenished in the culture well.

4.5. Expectation–maximisation and the Gaussian mixture model

We employed the Expectation–Maximisation (EM) algorithm for the detection of clusters within Gaussian Mixture Models [25], from which extracted the mean and covariance of each generation. The EM algorithm comprises two main steps: the Expectation (E) step and the Maximisation (M) step.

In the E-step, for each data point $\mathbf{f}$, we utilised our current estimates of π_g, μ_g, and σ_g to calculate the posterior probability that each cell belongs to generation g, given its fluorescence intensity measurement $\mathbf{f}$, denoted as $\gamma_g = \mathrm{P}(g|\,\mathbf{f})$.

Moving to the M-step, we leveraged the fact that the gradient of the log-likelihood of $p(\mathbf{f_i})$ with respect to π_g, μ_g, and σ_g could be computed. Consequently, the optimal values of π_g, μ_g, and σ_g were expressed in terms of γ_g. It was demonstrated that, under certain smoothness conditions, the iterative computation of the E-step and M-step led to locally optimal estimates of the parameters π_g, μ_g, and σ_g, along with the return of the posterior probability γ_g, which indicates the weight of each point belonging to one of the clusters.

In this context, we applied this model for cluster analysis to detect peaks corresponding to different generations. The normal assumption is the least biased choice for inferring the mean and the covariance of a bivariate distribution according to the maximum entropy principle [26,27]. Subsequently, we estimated π_g, $\mathrm{E}[f_g]$, and $\mathrm{Var}[f_g]$ from these clusters.

Acknowledgments

The authors are indebted to Andrea De Martino for fruitful and enjoyable discussions.

Disclosure statement

No potential conflict of interest was reported by the author(s).

Funding

This research was partially funded by grants from ERC-2019-Synergy Grant (ASTRA, n. 855923); EIC-2022-PathfinderOpen (ivBM-4PAP, n. 101098989); Project 'National Center for Gene Therapy and Drugs based on RNA Technology' (CN00000041) financed by NextGeneration EU PNRR MUR-M4C2-Action 1.4-Call 'Potenziamento strutture di ricerca e creazione di campioni nazionali di R&S' (CUP J33C22001130001).

ORCID

Mattia Miotto http://orcid.org/0000-0002-0043-8921
Giorgio Gosti http://orcid.org/0000-0002-8571-1404

References

[1] Q.A. Justman, *An explicit source for extrinsic noise*, Cell. Syst. 1 (2015), pp. 308–309.
[2] D. Huh and J. Paulsson, *Random partitioning of molecules at cell division*, Proc. Natl. Acad. Sci. 108 (2011), pp. 15004–15009.
[3] M.B. Elowitz, A.J. Levine, E.D. Siggia, and P.S. Swain, *Stochastic gene expression in a single cell*, Science 297 (2002), pp. 1183–1186.
[4] M. Miotto, E. Marinari, A. De Martino, and E. Aurell, *Competing endogenous RNA crosstalk at system level*, PLoS Comput. Biol. 15 (2019), Article ID e1007474.
[5] M. Miotto, M. Rosito, M. Paoluzzi, V. de Turris, V. Folli, M. Leonetti, G. Ruocco, A. Rosa, and G. Gosti, *Collective behavior and self-organization in neural rosette morphogenesis*, Front. Cell. Dev. Biol. 11 (2023), Article ID 1134091.
[6] M. Miotto and L. Monacelli, *Genome heterogeneity drives the evolution of species*, Phys. Rev. Res. 2 (2020), Article ID 043026.
[7] D. Huh and J. Paulsson, *Non-genetic heterogeneity from stochastic partitioning at cell division*, Nat. Genet. 43 (2010), pp. 95–100.
[8] M. Borsa, N. Barandun, F. Gräbnitz, I. Barnstorf, N.S. Baumann, K. Pallmer, S. Baumann, D. Stark, M. Balaz, N. Oetiker, F. Wagen, C. Wolfrum, A.K. Simon, N. Joller, Y. Barral, R. Spörri, and A. Oxenius, *Asymmetric cell division shapes naive and virtual memory t-cell immunity during ageing*, Nat. Commun. 12 (2021), Article ID 2715.

[9] D. Caudo, C. Giannattasio, S. Scalise, V. de Turris, F. Giavazzi, G. Ruocco, G. Gosti, G. Peruzzi, and M. Miotto, *Robust assessment of asymmetric division in colon cancer cells*. eLife 14 (2025), Article ID 104528.
[10] G. Peruzzi, M. Miotto, R. Maggio, G. Ruocco, and G. Gosti, *Asymmetric binomial statistics explains organelle partitioning variance in cancer cell proliferation*, Commun. Phys. 4 (2021), Article ID 188.
[11] M. Miotto, S. Scalise, M. Leonetti, G. Ruocco, G. Peruzzi, and G. Gosti, *A size-dependent division strategy accounts for leukemia cell size heterogeneity*, Commun. Phys. 7 (2024), Article ID 248.
[12] A. Biswas and J.S. Hwang, *A new bivariate binomial distribution*, Stat. Probab. Lett. 60 (2002), pp. 231–240.
[13] J.F. Markham, C.J. Wellard, E.D. Hawkins, K.R. Duffy, and P.D. Hodgkin, *A minimum of two distinct heritable factors are required to explain correlation structures in proliferating lymphocytes*, J. R. Soc. Interface 7 (2010), pp. 1049–1059.
[14] K.R. Duffy, C.J. Wellard, J.F. Markham, J.H.S. Zhou, R. Holmberg, E.D. Hawkins, J. Hasbold, M.R. Dowling, and P.D. Hodgkin, *Activation-induced b cell fates are selected by intracellular stochastic competition*, Science 335 (2012), pp. 338–341.
[15] E.E. Kuchen, N.B. Becker, N. Claudino, and T. Höfer, *Hidden long-range memories of growth and cycle speed correlate cell cycles in lineage trees*, eLife 9 (2020), Article ID e51002.
[16] C. Enrico Bena, M.D. Giudice, A. Grob, T. Gueudré, M. Miotto, D. Gialama, M. Osella, E. Turco, F. Ceroni, A.D. Martino, and C. Bosia, *Initial cell density encodes proliferative potential in cancer cell populations*, Sci. Rep. 11 (2021), pp. 1–11.
[17] S. Scalise, G. Gosti, G. Ruocco, G. Peruzzi, and M. Miotto, *Probing leukemia cells behavior under starvation*, arXiv (2024)
[18] N. Moris, C. Pina, and A.M. Arias, *Transition states and cell fate decisions in epigenetic landscapes*, Nat. Rev. Genet. 17 (2016), pp. 693–703.
[19] M. Miotto, G. Ruocco, and M. Paoluzzi, *Non-equilibrium phase transitions in hybrid Voronoi models of cell colonies*, arXiv (2024)
[20] M.K. Delgado and C. Cabernard, *Mechanical regulation of cell size, fate, and behavior during asymmetric cell division*, Curr. Opin. Cell Biol. 67 (2020), pp. 9–16. http://dx.doi.org/10.1016/j.ceb.2020.07.002
[21] A. De Martino, T. Gueudré, and M. Miotto, *Exploration-exploitation tradeoffs dictate the optimal distributions of phenotypes for populations subject to fitness fluctuations*, Phys. Rev. E 99 (2019), Article ID 012417.
[22] S. Tripathi, P. Chakraborty, H. Levine, M.K. Jolly, and A. Onufriev, *A mechanism for epithelial-mesenchymal heterogeneity in a population of cancer cells*, PLoS Comput. Biol. 16 (2020), Article ID e1007619.
[23] A.B. Lindner, R. Madden, A. Demarez, E.J. Stewart, and F. Taddei, *Asymmetric segregation of protein aggregates is associated with cellular aging and rejuvenation*, Proc. Natl. Acad. Sci. 105 (2008), pp. 3076–3081. http://dx.doi.org/10.1073/pnas.0708931105
[24] A. Filby, J. Begum, M. Jalal, and W. Day, *Appraising the suitability of succinimidyl and lipophilic fluorescent dyes to track proliferation in non-quiescent cells by dye dilution*, Methods 82 (2015), pp. 29–37.
[25] A.P. Dempster, N.M. Laird, and D.B. Rubin, *Maximum likelihood from incomplete data via the em algorithm*, J. R. Stat. Soc. Ser. B: Stat. Methodol. 39 (1977), pp. 1–22.
[26] M. Miotto and L. Monacelli, *Entropy evaluation sheds light on ecosystem complexity*, Phys. Rev. E98 (2018), Article ID 042402.
[27] M. Miotto and L. Monacelli, *Tolomeo, a novel machine learning algorithm to measure information and order in correlated networks and predict their state*, Entropy 23 (2021), Article ID 1138.

Philosophical Magazine

ISSN: 1478-6435 (Print) 1478-6443 (Online) Journal homepage: www.tandfonline.com/journals/tphm20

Modelling of nanosensors based on localised surface plasmon resonance

Aida Firoozi, Reza Khordad & Hamid Reza Rastegar Sedehi

To cite this article: Aida Firoozi, Reza Khordad & Hamid Reza Rastegar Sedehi (2023) Modelling of nanosensors based on localised surface plasmon resonance, Philosophical Magazine, 103:22, 2054-2071, DOI: 10.1080/14786435.2023.2255143

To link to this article: https://doi.org/10.1080/14786435.2023.2255143

Published online: 13 Sep 2023.

PHILOSOPHICAL MAGAZINE
2023, VOL. 103, NO. 22, 2054–2071
https://doi.org/10.1080/14786435.2023.2255143

Taylor & Francis
Taylor & Francis Group

Modelling of nanosensors based on localised surface plasmon resonance

Aida Firoozi[a], Reza Khordad[a] and Hamid Reza Rastegar Sedehi[b]

[a]Department of Physics, College of Sciences, Yasouj University, Yasouj, Iran; [b]Department of Physics, College of Sciences, Jahrom University, Jahrom, Iran

ABSTRACT

To design nanosensors based on localised surface plasmon (LSP), a structure is considered consisting of metal nanoparticles and study the influence of nanoparticles size, material, geometry, and background refractive index (RI) on its performance. We propose a nanosensor based on nanoplasmonic and investigate its sensitivity. The boundary element method is employed to calculate the extinction cross-section and sensitivity of the proposed sensor. We study the effect of various parameters on LSP resonance. Our calculations about extinction, scattering, and absorption spectra have been compared with experimental data. According to the comparison, it is deduced the boundary element method provides acceptable results. It is shown that the proposed nanosensor is very sensitive to the variation of sample RI. Moreover, it is possible to adjust the required spectral range by changing the geometry and material of nanoparticles. Here, the highest sensitivity is obtained for cubic nanoparticles made of silver.

ARTICLE HISTORY
Received 18 January 2023
Accepted 27 August 2023

KEYWORDS
Nanosensor; boundary element method; plasmonic

1. Introduction

In recent decades, the rapid development of nanoplasmonic science and the possibility of making objects in the nanoscale have opened the way for the control of electromagnetic waves at the nanoscale. Nanostructures can be used in the manufacture of optical instruments in nano-dimensions and also in various fields such as nanoplasmonics, nano-biotechnology, medicine, etc. Plasmonic materials such as gold, silver, copper, and aluminium are used to make plasmonic nanoparticles. These types of nanoparticles interact with the incident light to create a strong electromagnetic field around them which causes the formation of a localised surface plasmon. When an electromagnetic wave radiates on a metal surface, the electric field of the radiation wave oscillates the electrons in the conduction band. The group oscillation of conduction band electrons is called surface plasmon [1].

CONTACT Reza Khordad rezakh2025@yahoo.com Department of Physics, College of Sciences, Yasouj University, 75918, Yasouj, Iran

When light is radiated on a metal nanoparticle, the plasmon created is localised and confined at the nanoparticle surface due to the limited surface area and volume of the nanoparticle. It creates a strong electromagnetic field around the nanoparticles, which is called a localised surface plasmon [1,2]. If the frequency of the incident light is equal to the normal frequency of this oscillating motion, the LSP resonance occurs. The LSPR depends on parameters such as geometry, dimension, etc. [3–5],

There are several ways to diagnose bacteria and different diseases. Efforts to develop and improve the performance of biosensors have led to the development of various types of biosensors. The basis of a sensor is to detect and react with a compound or compounds, and to display the results as an electrical, optical, and chemical message. One of the most notable applications of plasmonic resonance in biosensors is as a useful tool for bioanalysis, early detection in medicine [6], environmental monitoring [7], and food industry safety [8]. As we know, cancer is the second most common cause of death worldwide. For this reason, today, researchers in universities and industrial centres are active in the field of research on biosensors, which has led to the construction of accurate and sensitive biosensors to identify biological targets [9–13]. The ultimate goal of biosensors is to identify targets in the fastest time and with the least possible sample size for detection. Glucose sensors are currently one of the most successful biosensors on the market. Easy production, reasonable price, and portability are other advantages of this type of sensor.

To achieve the highest sensitivity of the sensors, this requires calculating the extinction cross section by the full vector solution of Maxwell equations. To solve the equation, there are various computational methods such as finite differential time domain (FDTD) [14,15], multiple multipole method [15], finite element method [16], and boundary element method (BEM) [17].

Among the computational methods, the FDTD is of special importance due to its ability to solve Maxwell equations in the time domain. This method studies the interaction of light with different materials (linear, nonlinear, homogeneous, inhomogeneous, isotropic, anisotropic, etc.). However, one of the disadvantages of this method is that it is time-consuming and requires the use of very small divisions to obtain accurate answers. Therefore, here, we have chosen the BEM to calculate the sensitivity of the sensors. The way presented in this paper is to use plasmonic nanoparticles with various geometries to enhance the nanosensor sensitivity based on LSP. Here, using the boundary element method, the effect of sizes, material, geometry of nanoparticles, and the RI of the environment are studied on the extinction cross-section. We show that by fine-tuning these parameters, the sensitivity of nanosensor based on LSP can be significantly increased.

2. Simulation details

The BEM is used to acquire our numerical data. The BEM is a semi-analytic approach in the frequency range. In this method, we first discretise the object's surface into small elements. The Helmholtz wave equation for a homogeneous substance is written as the following equation.

$$(\nabla^2 + k_j^2)G_j(\boldsymbol{r}, \boldsymbol{r}') = -4\pi\delta(\boldsymbol{r} - \boldsymbol{r}') \tag{1}$$

where G is the Green function as below

$$G_j(\boldsymbol{r}, \boldsymbol{r}') = \frac{e^{i\boldsymbol{k}_j.(\boldsymbol{r}-\boldsymbol{r}')}}{|\boldsymbol{r} - \boldsymbol{r}'|} \tag{2}$$

where $k_j = \sqrt{\varepsilon_j}k$ and $k = \omega/c$ are the wave numbers in the environment and vacuum, respectively, and c is the speed of light.

The wave equations of the vector and scalar potentials are expressed by

$$\nabla^2\varphi + k^2\varepsilon\varphi = -4\pi\rho \tag{3}$$

$$\nabla^2 A + k^2\varepsilon A = -4\pi J \tag{4}$$

The following equations can be obtained by solving the Equations. (3) and (4)

$$\varphi_j(\boldsymbol{r}) = \varphi_j^e(\boldsymbol{r}) + \oint G_j(\boldsymbol{r}, \boldsymbol{r}')\sigma_j(\boldsymbol{r}')d\boldsymbol{S} \tag{5}$$

$$A_j(\boldsymbol{r}) = A_j^e(\boldsymbol{r}) + \oint G_j(\boldsymbol{r}, \boldsymbol{r}')h_j(\boldsymbol{r}')d\boldsymbol{S} \tag{6}$$

Here, σ_j and h_j are the surface charge and current distributions, respectively.

By knowing A and φ, and inserting them in the following equation

$$\boldsymbol{E} = ik\boldsymbol{A} - \nabla\varphi, \qquad \boldsymbol{H} = \nabla \times \boldsymbol{A} \tag{7}$$

One can determine an electric and magnetic field in the whole space.

By using electric and magnetic fields, the extinction cross-section is determined by

$$C_{ext} = -\frac{1}{n_b}\oint Re\{\hat{\boldsymbol{n}}(\boldsymbol{E} \times \boldsymbol{H}_{inc}^* + \boldsymbol{E}_{inc}^* \times \boldsymbol{H})\}d\boldsymbol{S} \tag{8}$$

In the BEM, the object surface is discretised into small elements (see Figure 1).

The computational space studied in this paper is shown in Figure 2. The nanostructure consists of two spherical nanoparticles with diameter D and two cubic nanoparticles with length L which are at a distance of 10 nm from each other in an environment with a RI of n and under plane wave radiation. Johnson and Christie's laboratory data were used for the refractive index of gold and silver nanoparticles.

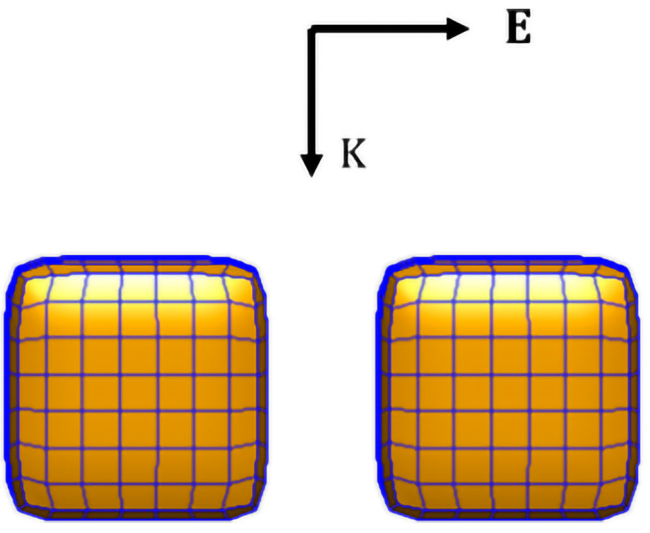

Figure 1. Display of elementalisation of a nanoparticle in computational space.

The sensor sensitivity is obtained by the following relation

$$S = \frac{\Delta\lambda}{\Delta n} = \frac{\lambda_2 - \lambda_1}{n_2 - n_1} \tag{9}$$

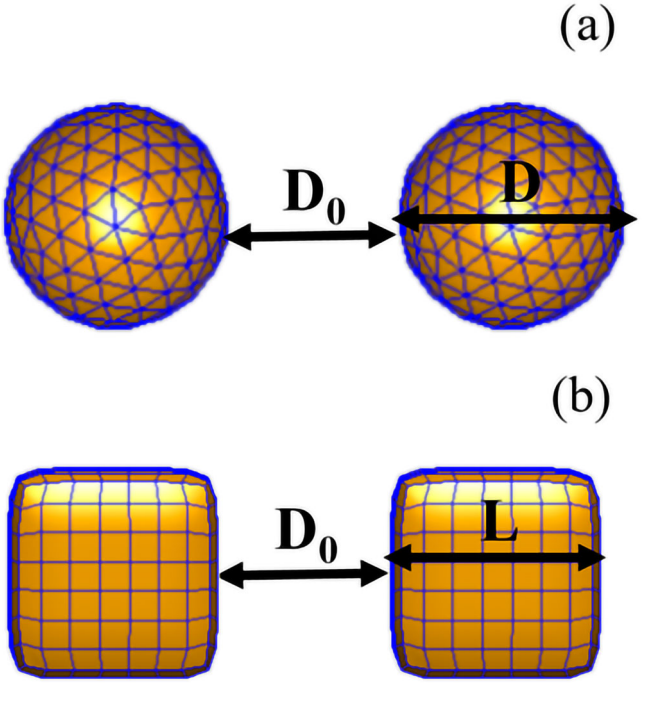

Figure 2. Schematic of the used nanoparticles. (a) spherical, and (b) cubic nanoparticles.

where $\Delta\lambda$ is the variations of the absorption wavelength of the extinction cross-section and Δn is the variations in the RI of the environment in which the nanoparticle is located [18].

Another relation that is calculated in this paper is the enhancement factor (EF), which is shown in the following equation [18]

$$EF = \frac{(\lambda_D)_{n_2} - (\lambda_D)_{n_1}}{(\lambda_0)_{n_2} - (\lambda_0)_{n_1}} \tag{10}$$

In the above relation, λ_D is the absorption wavelength of the coupled (dimer) nanoparticles and λ_0 is the absorption wavelength of a single nanoparticle.

3. Numerical results

Nanosensors based on LSP resonance strongly depend on the material, sizes, and geometry of the nanoparticle and the environment in which the nanoparticle is located. Therefore, in this section, we will calculate these factors and examine their effect on the sensitivity of the sensors.

Figure 3 shows the extinction cross section versus wavelength for a single gold spherical nanoparticle and dimer gold spherical nanoparticles located in two environments with refractive index of 1 and 1.33. The relative shift of

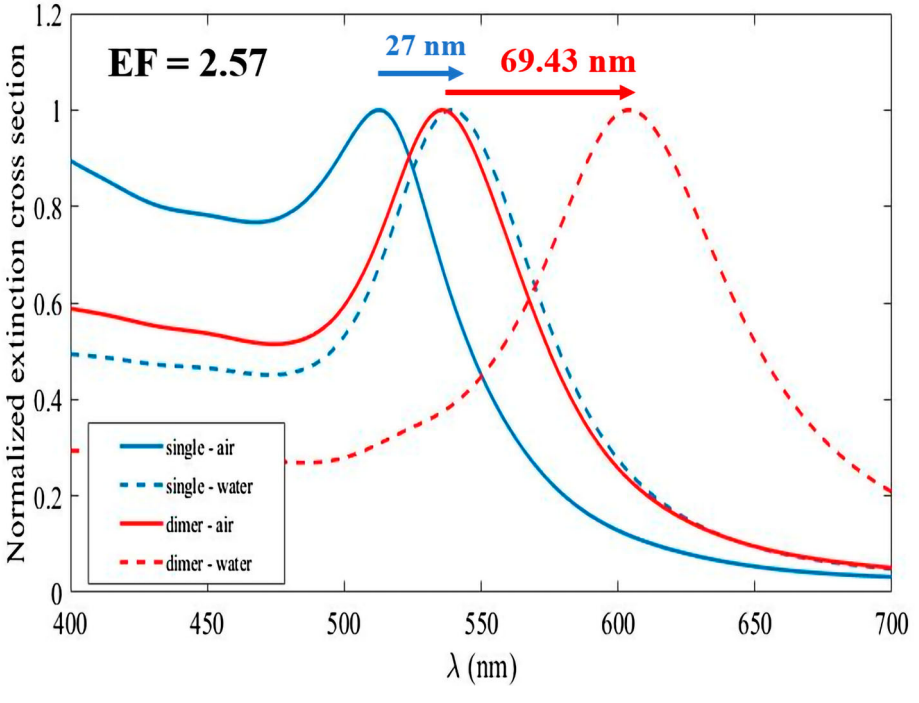

Figure 3. Extinction cross section versus wavelength for single and dimer gold spherical nanoparticles in two environments with refractive index 1 and 1.33.

the absorption wavelength of a single spherical nanoparticle in environments with two different refractive indices is 27 nm and for coupled spherical nanoparticles is 70 nm. According to Equation (10), the EF calculated for these conditions is 2.57.

Figure 4 displays the dimensionless relative wavelength shift parameter $\frac{\Delta\lambda}{\lambda_0}$ versus the dimensionless number $\frac{D}{D_0}$ for gold dimer spherical nanoparticles in two different environments with refractive indices as 1 and 1.33. It is seen that with increasing the number $\frac{D}{D_0}$, the parameter $\frac{\Delta\lambda}{\lambda_0}$ is reduced. Also, at a fixed $\frac{D}{D_0}$, the parameter $\frac{\Delta\lambda}{\lambda_0}$ increases when the refractive index is enhanced.

In Figure 5, the EF is plotted ersus the number $\frac{D}{D_0}$ for gold dimer spherical nanoparticles. It is observed that the EF is reduced with increasing the number $\frac{D}{D_0}$.

Figure 6 shows the extinction cross section versus wavelength for gold coupled spherical nanoparticles with diameter $D = 90\,\text{nm}$ and $D_0 = 10\,\text{nm}$. The RI of the environment has been chosen as 1 and 1.33 in this figure. It can be seen from the figure that the peak position of LSPR shifts towards a higher wavelength with increasing the RI. By using Equation (9), we can obtain the sensitivity as $242\,\frac{\text{nm}}{\text{RIU}}$.

In order to calculate more accurately, in Figure 7, the peak shift of resonant wavelength has been plotted versus distance between gold spherical

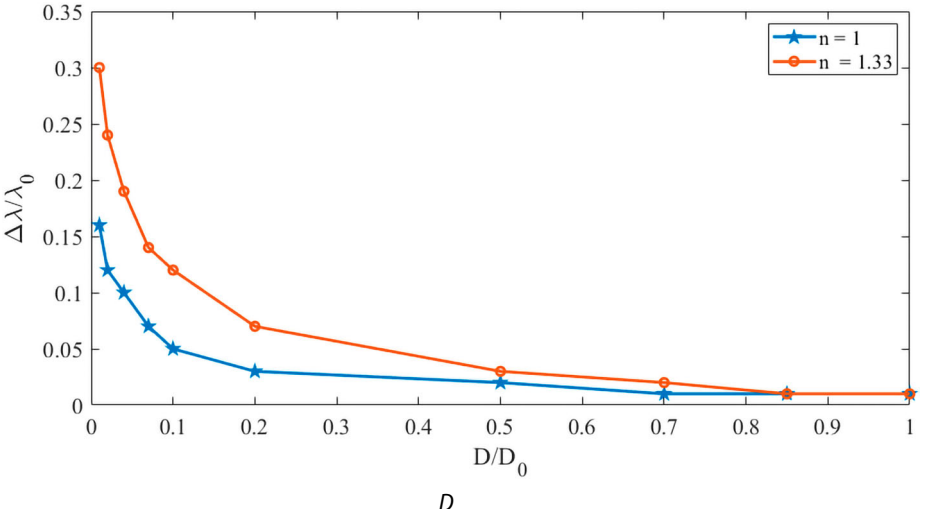

Figure 4. Relative wavelength shift versus $\frac{D}{D_0}$ for gold dimer spherical nanoparticles in two environments with refractive index 1 and 1.33.

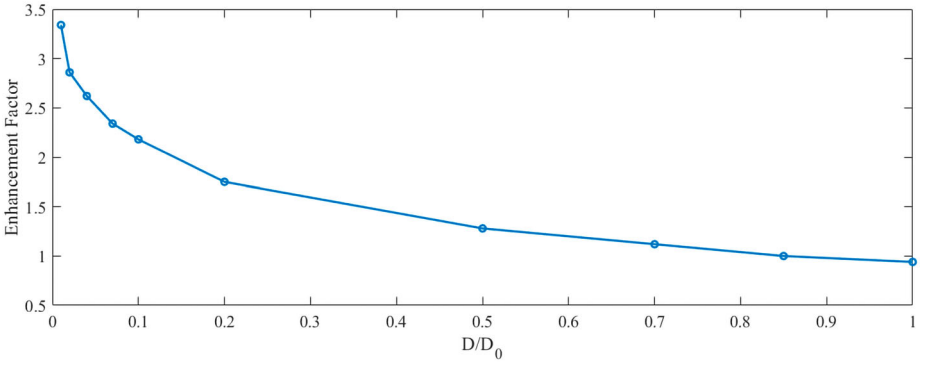

Figure 5. The enhancement factor (EF) versus $\frac{D}{D_0}$ for gold dimer spherical nanoparticles.

nanoparticles for different diameters as 50, 70, and 90 nm. As expected, the curve slope decreases with increasing nanoparticle distance.

In order to study the enhancement of sensor sensitivity, we investigate the effect of nanoparticle geometry on the sensitivity. For this goal, we use the cubic nanoparticles in our calculations. Figure 8 demonstrates the extinction cross section versus wavelength for cubic gold coupled nanoparticles with a size of 90 nm and a distance of 10 nm. The curves have been plotted for two

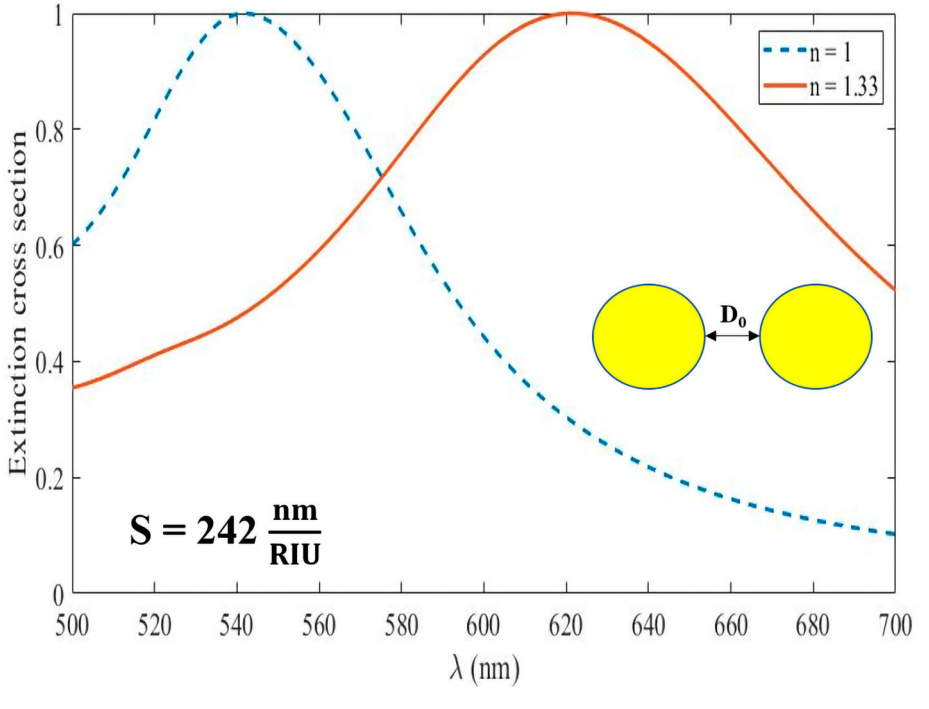

Figure 6. Extinction cross section versus wavelength for gold dimer spherical nanoparticles with diameter of 90 nm in two environments with refractive index 1 and 1.33. The sensitivity is also displayed in the figure.

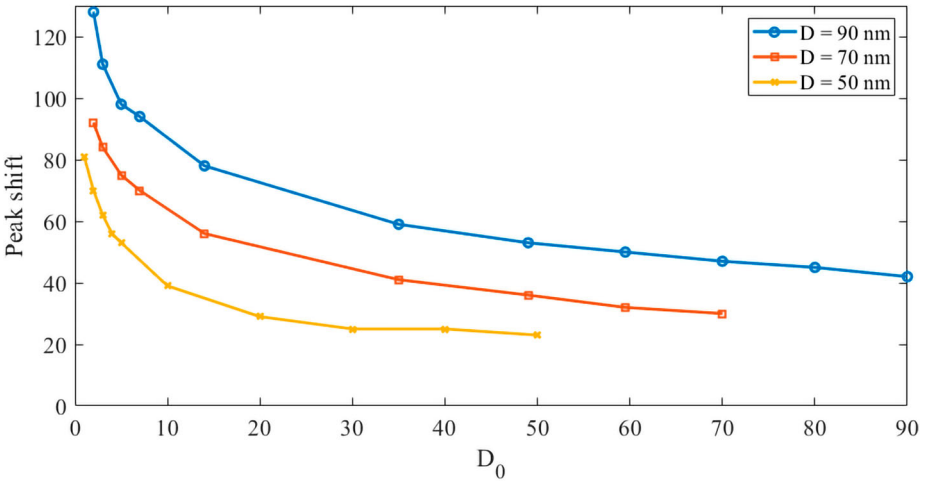

Figure 7. The wavelength shifts versus distance between spherical gold nanoparticles for different diameters.

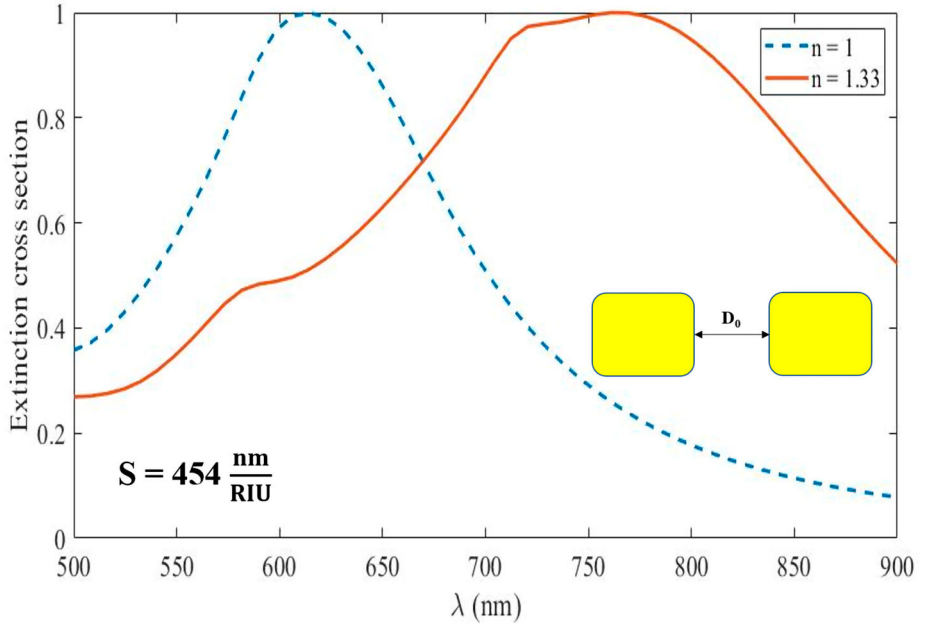

Figure 8. Extinction cross section versus wavelength for gold dimer cubic nanoparticles with a length of 90 nm in two environments with refractive index 1 and 1.33. The sensitivity is also displayed in the figure.

different refractive indices. By using Equation (9), we can obtain the sensitivity as $454\,\frac{\text{nm}}{\text{RIU}}$.

Figure 9 presents the peak shift of resonant wavelength versus distance between cubic gold nanoparticles for different lengths as 50, 70, and 90 nm.

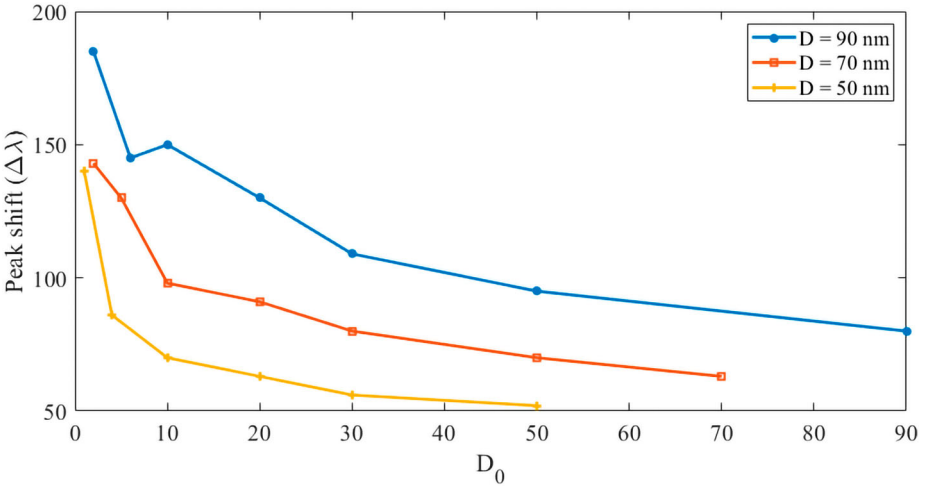

Figure 9. The wavelength shifts versus the distance between cubic gold nanoparticles for different lengths.

As the distance between the cubic nanoparticles increases, the peak shift decreases. Therefore, in order to achieve the highest sensitivity, the nanoparticles must be very close to each other.

One of the most important factors in the sensitivity of the sensor is the nanoparticle material. In order to investigate the effect of nanoparticle material on the sensitivity of sensors, we considered the silver spherical dimer nanoparticles and in the same conditions. In Figure 10, we have examined the extinction cross section versus wavelength for two different refractive indices as 1 and 1.33. It is seen from Figure 10 that the peak position of LSPR shifts towards a higher wavelength with raising the RI. The sensitivity calculated for silver spherical nanoparticles is $369\frac{\text{nm}}{\text{RIU}}$. With regard to the value of sensitivity for silver spherical nanoparticles, we deduce that the sensitivity depends on nanoparticle material. The nanoparticle material has a significant effect on improving the sensitivity of sensor. The sensitivity of silver spherical nanoparticles is bigger than gold nanoparticles.

Figure 11 displays peak shift versus the distance between silver spherical coupled nanoparticles for three different diameters. As we can see, the peak shift decreases as the nanoparticle distance increases. The figure shows that the peak shift strongly depends on the nanoparticles distance and their diameters. Therefore, achieving the highest sensitivity of the sensor requires selecting an appropriate distance through optimisation methods. Of course, in practice, there are limitations that cannot bring the two nanoparticles as close as desired.

Figure 12 shows the extinction cross section versus wavelength for silver cubic dimer nanoparticles with s length of 90 nm located at a distance of 10 nm from each other. The curves have been plotted for two different

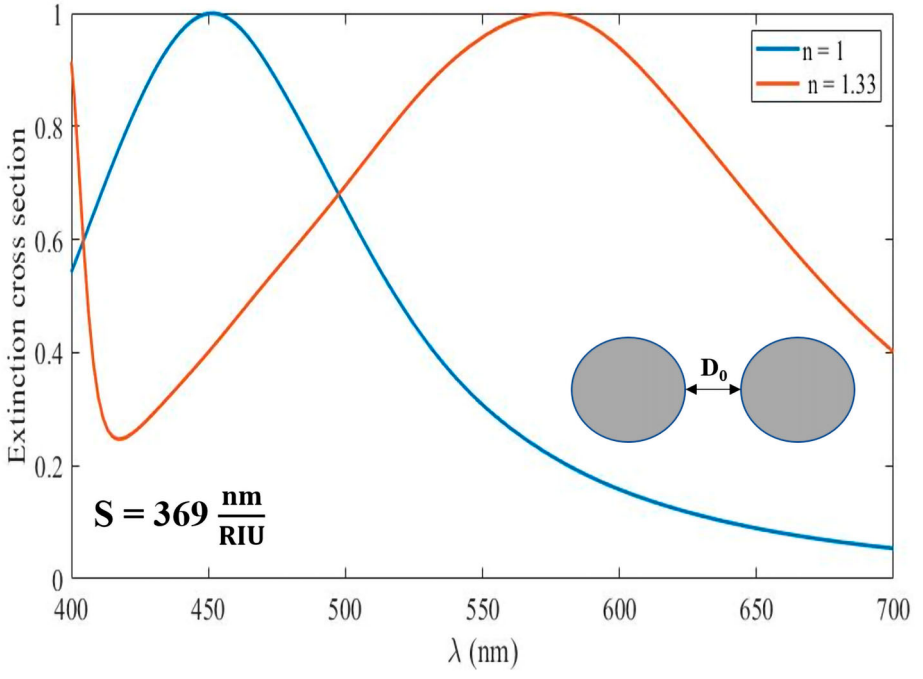

Figure 10. The same as Figure 6, but for silver nanoparticles.

refractive indices as 1 and 1.33. The sensitivity was calculated for this figure as $533\frac{\text{nm}}{\text{RIU}}$. With comparing the previous conditions, we find that the sensitivity has increased significantly.

In Figure 13, we have presented the peak shift versus the distance between two silver nanoparticles for various cubic nanoparticle lengths as 70, 80, and 90 nm.

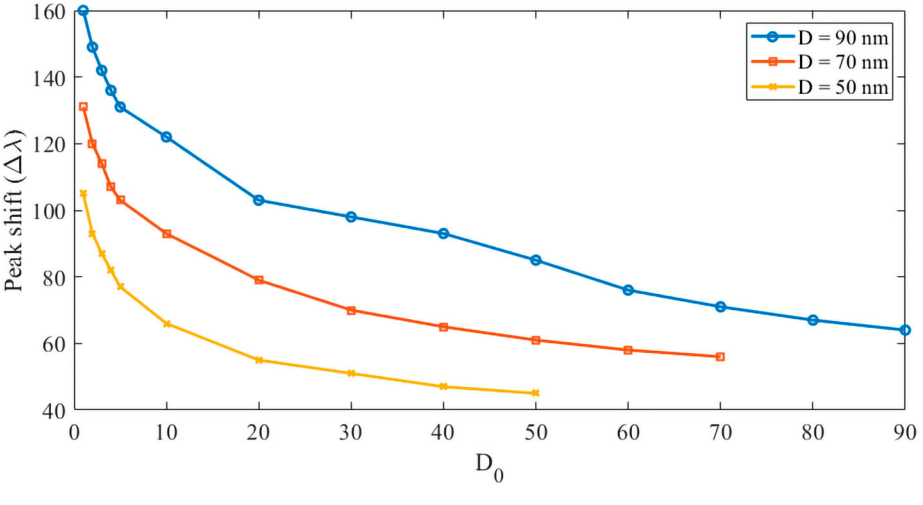

Figure 11. The same as Figure 7, but for silver nanoparticles.

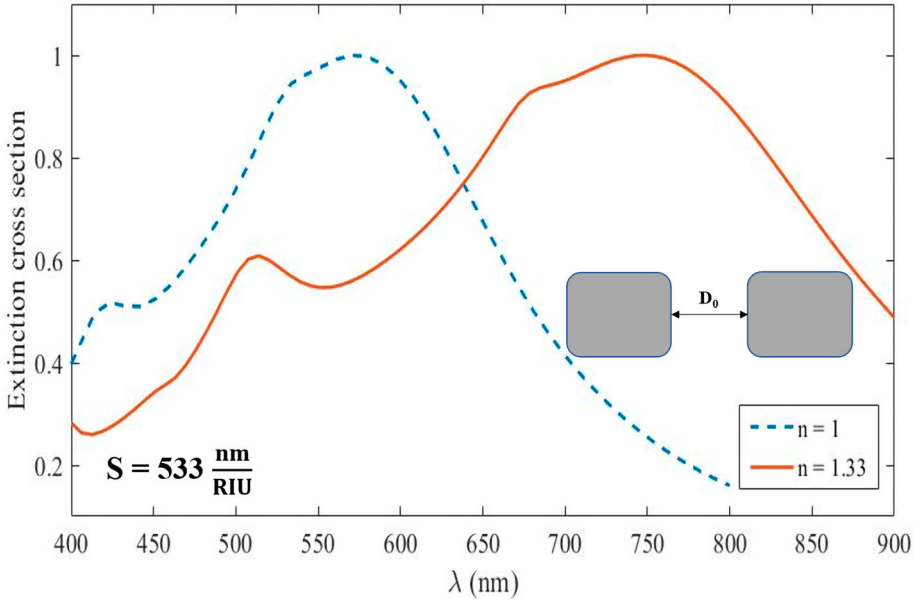

Figure 12. The same as Figure 8, but for silver nanoparticles.

As the results show, the peak shift reduces with increasing the nanoparticles distance. Also, the peak shift decreases with enhancing the nanoparticle sizes.

In Figure 14, the sensitivity of the nanosensor with spherical, and cubic geometries is calculated versus the distance between the nanoparticles. As can be seen, the sensitivity decreases as the distance between the nanoparticles increases. In addition, with the increase in the nanoparticles size, the sensitivity increases. When the distance between the nanoparticles is 1 nm, the sensitivity of spherical nanoparticles with a diameter of 40, 50, and 60 nm is 238, 266, and 304 nm/RIU, respectively. Also, when the distance between cubic nanoparticles

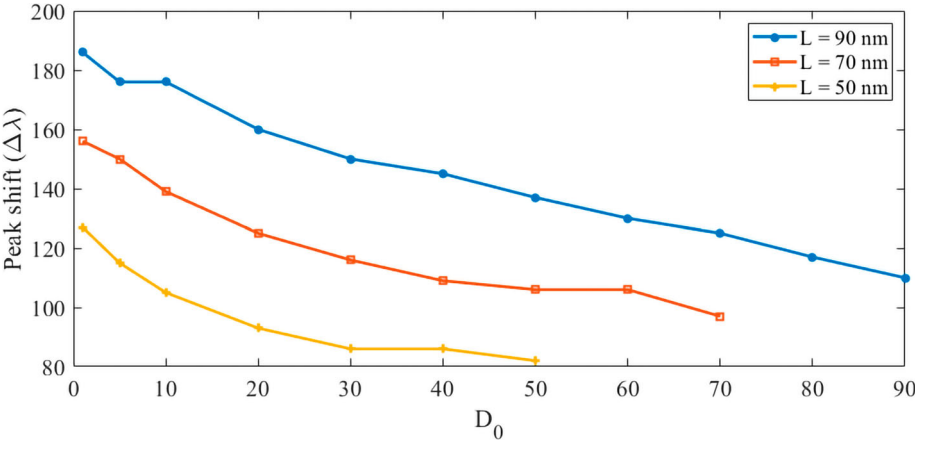

Figure 13. The same as Figure 9, but for silver nanoparticles.

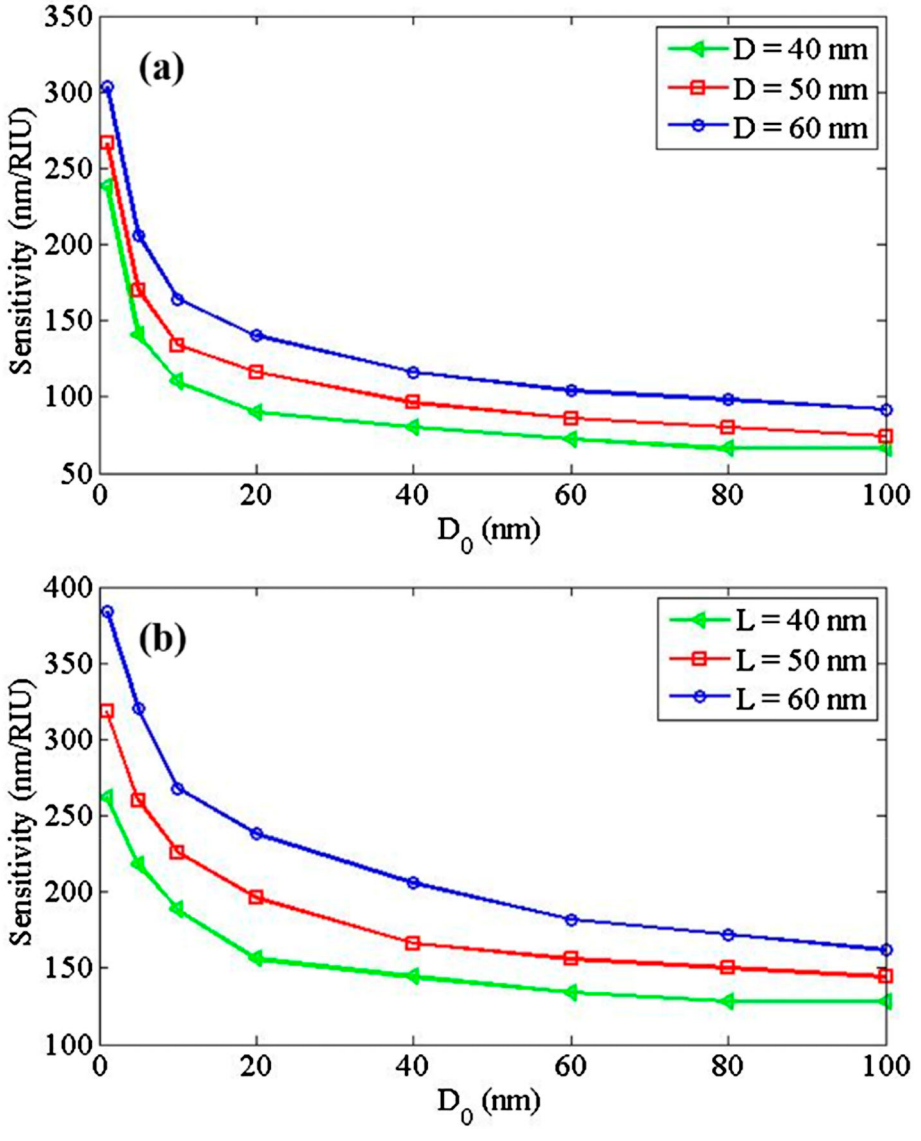

Figure 14. The sensitivity of gold nanoparticles versus the distance between the nanoparticles. (a) spherical and (b) cubic nanoparticles.

is 1 nm, the sensitivity of nanoparticles with a length of 40, 50, and 60 nm is 262, 318, and 384 nm/RIU, respectively.

It is well known that the performance of a nanosensor can be measured using the figure of merit (FoM). It is defined as

$$\mathrm{FoM} = \frac{\mathrm{S}}{\mathrm{FWHM}}$$

where S is the sensitivity and FWHM is full width at half maximum.

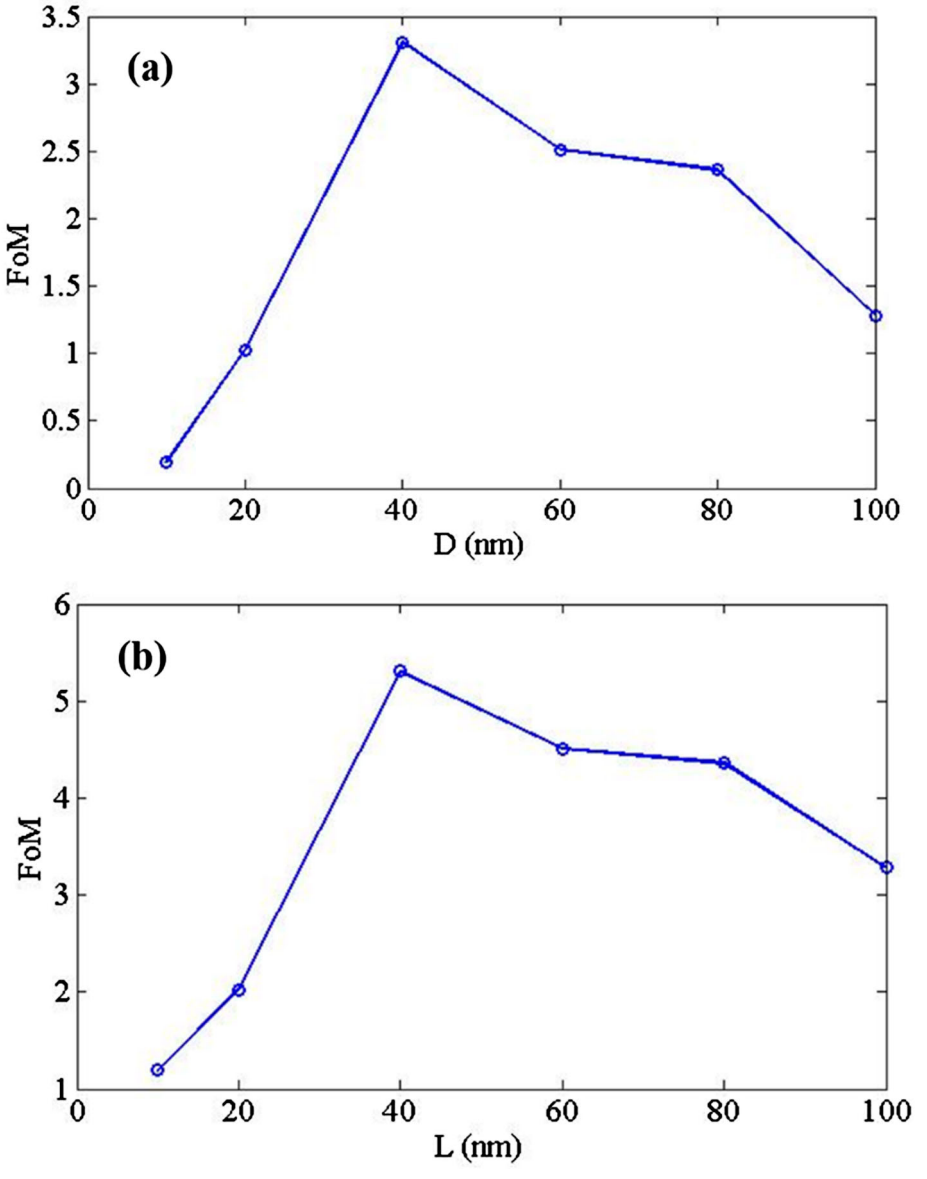

Figure 15. FoM of gold nanoparticles as a function of nanoparticles size. (a) spherical, and (b) cubic nanoparticles.

Figure 15 displays the calculated FoM versus the size of gold nanoparticles. The results have been presented for the spherical, and cubic nanoparticles. It is seen that when the diameter of spherical nanoparticles is 40 nm, the value of FoM reaches 31.3 1/RIU. Also, when the length of cubic nanoparticles is 40 nm, the value of FoM reaches 5.31 1/RIU. The value of FoM for the nanoparticles with a size larger than 40 nm gradually decreases because the FWHM increases and causes a decrease in FoM.

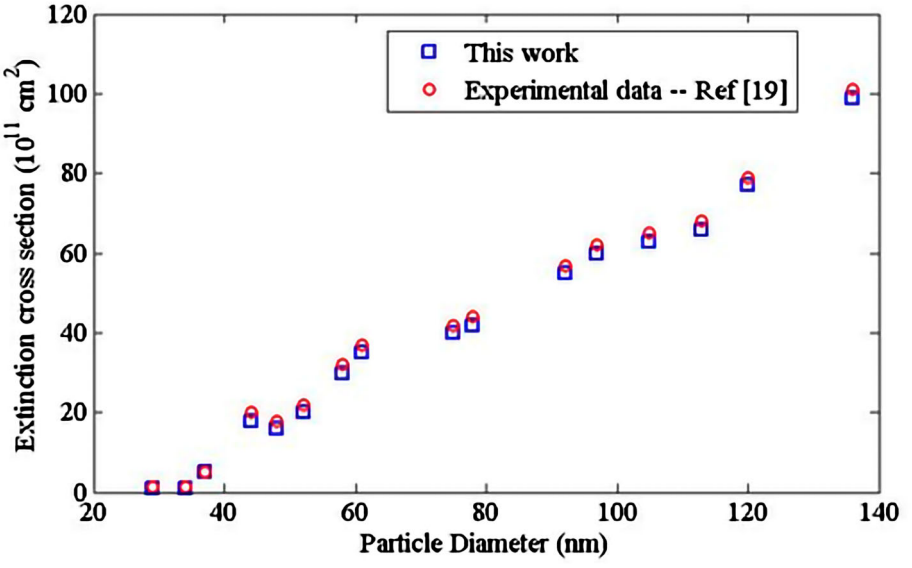

Figure 16. The extinction cross-section of spherical gold nanoparticles versus the nanoparticle's diameter.

To check the accuracy of our calculations, we compared our results with the experimental available data in Ref. [19]. Figure 16 demonstrates the extinction cross-section as a function of gold nanoparticles diameter. As can be seen, the cross section increases by raising the diameter. Our results have been compared with the experimental data [19]. It can be seen that there is good agreement.

We have also calculated the extinction, scattering, and absorption spectra of the gold nanoparticles and compared with experimental data [19]. To compare, we have selected the diameter of nanoparticles as 120, and 136 nm. Figure 17 (a)–(c) corresponds to the nanoparticles with a diameter 120 nm. In Figure 17(d)–(f), the nanoparticle diameter is 136 nm. As can be seen, the calculated absorption spectra for both diameters have the best agreement with the experimental data [19]. At lower wavelengths, the calculated scattering, and extinction spectra for both diameters have good agreement with experimental data [19].

4. Conclusions

In this study, we have examined the effect of various factors on the performance of nanosensors based on the LSPR. We have found that the sensitivity of the metal nanoparticles can be adjusted by changing the geometry, material, and sizes. By comparing gold and silver nanoparticles, it was found that silver nanosensor is more sensitive than gold. We have also studied the geometry of nanoparticles in this work. Nanoparticles with spherical and cubic geometry were

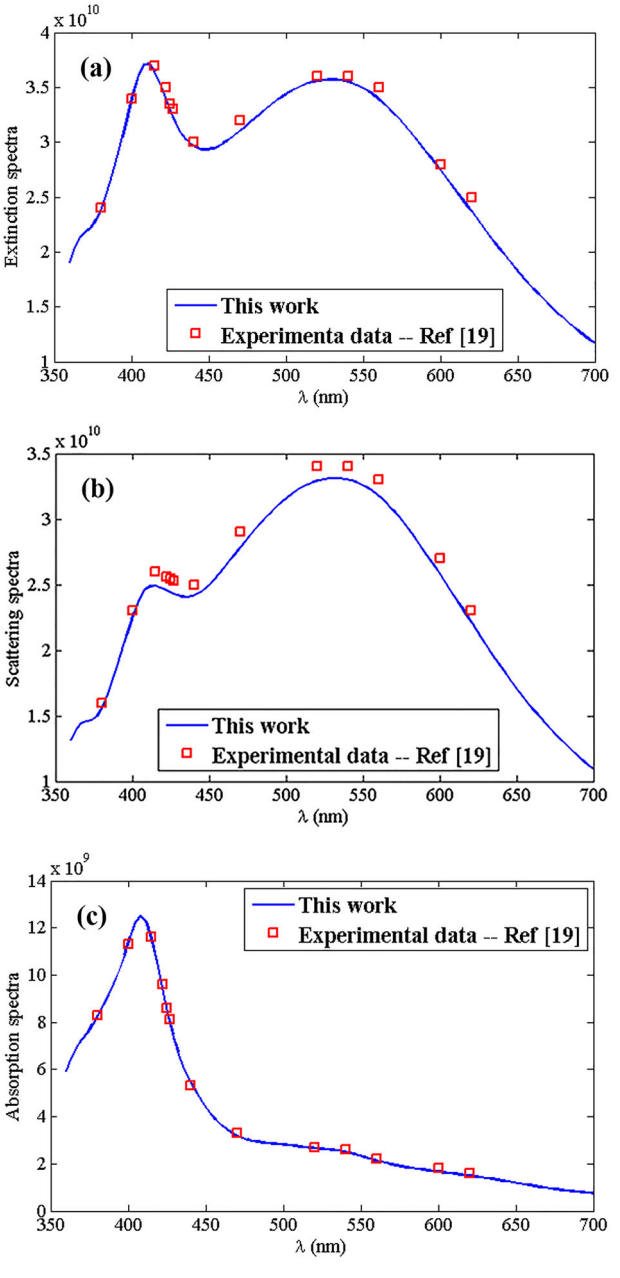

Figure 17. The extinction, scattering, and absorption spectra versus the wavelength for the spherical gold nanoparticles. The figures (a)–(c) correspond to the diameter of 120 nm. In the figures (d)–(f), the diameter is 136 nm.

examined. We have shown that by using a nanosensor with cubic geometry, the sensitivity of the sensor is higher. In the next step, the effect of nanoparticle sizes was investigated. It has been shown that with increasing nanoparticle sizes, the peak shift increases. In general, the proposed nanosensor, in addition

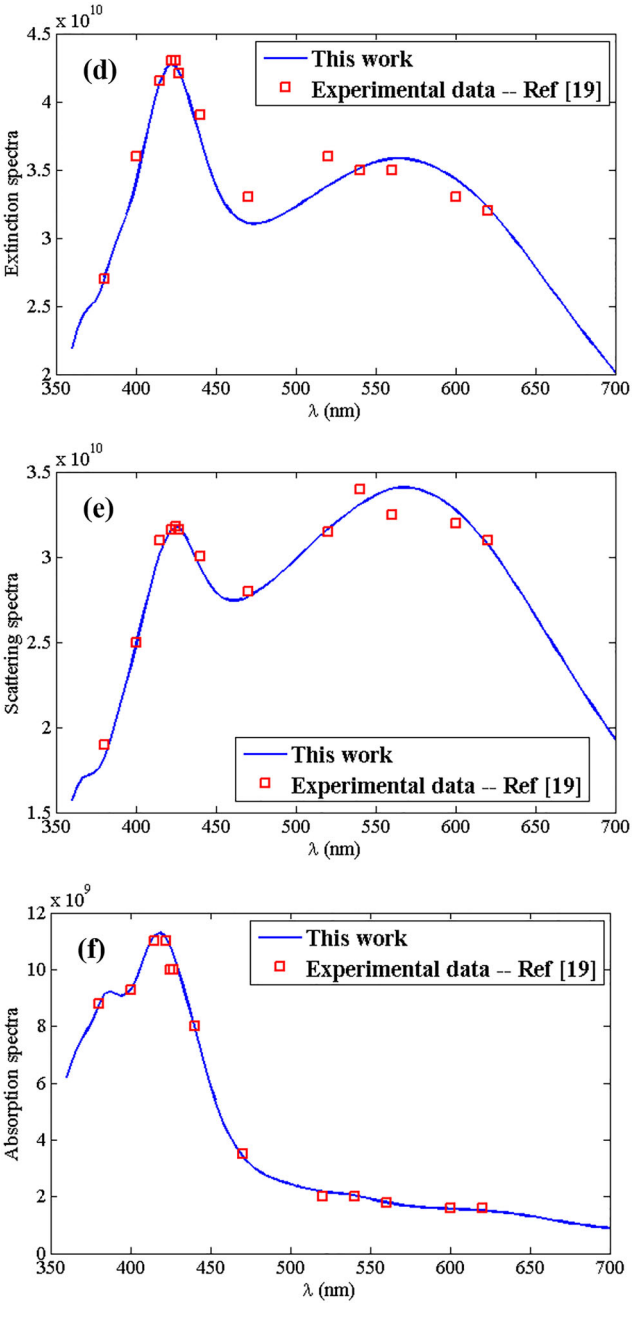

Figure 17 *Continued*

to being highly sensitive to refractive index changes, provides the possibility of changing the wavelength range to suit the sample under study. Using these results, it is possible to predict the appropriate laboratory configuration to achieve the desired sensor sensitivity.

Data availability statement

The data that supports the findings of this study are available from the corresponding author upon reasonable request.

Disclosure statement

No potential conflict of interest was reported by the authors.

Funding

The authors declare that no funds, grants, or other support were received during the preparation of this manuscript.

References

[1] L. Novotny and B. Hecht, *Principles of Nano-Optics*, Cambridge University Press, New York, 2006.

[2] H. Sari, F. Ungan, E. Kasapoglu, S. Sakiroglu, and I. Sökmen, *Intense laser-induced electronic and optical properties in double finite oscillator potential*. Philos. Mag. 99 (2019), pp. 2444–2456.

[3] S. D'Agostino, F. Della Sala, and L.C. Andreani, *Dipole-excited surface plasmons in metallic nanoparticles: Engineering decay dynamics within the discrete-dipole approximation*. Phys. Rev. B. 87 (2013), p. 205413.

[4] A. Firoozi, R. Khordad, and H. R. Rastegar Sedehi, *Study of enhanced sensitivity of nanosensors by using gold bowtie nanoparticles*, J. Nonlinear Opt. Phys. Mater. (2023). doi:10.1142/S0218863523500571.

[5] A. Mohammadi, V. Sandoghdar, and M. Agio, *Gold, copper, silver and aluminum nanoantennas to enhance spontaneous emission*, J. Comput. Theor. Nanosci. 6 (2009), pp. 2024–2030.

[6] S. Barizuddin, S. Bok, and S. Gangopadhyay, *Plasmonic sensors for disease detection – A review*. J. Nanomed. Nanotechnol. 7 (2016), p. 1000373.

[7] W. Li, Y. Qiu, L. Zhang, L. Jiang, Z. Zhou, H. Chen, and J. Zhou, *Aluminum nanopyramid array with tunable ultraviolet–visible–infrared wavelength plasmon resonances for rapid detection of carbohydrate antigen 199*. Biosens. Bioelectron. 79 (2016), pp. 500–507.

[8] M. Li, S.K. Cushing, and N. Wu, *Plasmon-enhanced optical sensors: A review*. Analyst. 140 (2015), pp. 386–406.

[9] T. Fu, C. Du, Y. Chen, R. Zhang, Y. Zhu, L. Sun, and D. Shi, *Enhanced RI sensitivity and SERS performances of individual Au nanobipyramid dimers*. Plasmonics 16 (2021), pp. 485–491.

[10] A. Firoozi, R. Khordad, and H.R. Rastegar Sedehi, *Effects of geometry and size of noble metal nanoparticles on enhanced refractive index sensitivity*. Appl. Phys. A 128 (2022), p. 1074.

[11] K. Lv, Q. Wei, T. Zhu, X. Zhao, Z. Li, Y. Xu, S. Chen, Z. Li, X. Fan, W. Lu, M. Shao, B. Man, H. Li, and C. Yang, *Sensitive flexible biosensor based on the three-dimensional layered AgNFs@graphene nanohybrids*. Sens. Actuators, B. 336 (2021), pp. 129737.

[12] A. Firoozi, R. Khordad, and H.R. Rastegar Sedehi, *Nanosensors sensitivity based on localized surface plasmons created in bimetallic nanoshells*. Mod. Phys. Lett. B 37 (2023). doi:10.1142/S0217984923500938.
[13] A. Firoozi, R. Khordad, and H.R. Rastegar Sedehi, *Study of the sensitivity of Au@$Cu_{2-x}S$ conical nanoshell sensors based on localized surface plasmons*. Indian J. Phys. (2023). doi:10.1007/s12648-023-02741-9.
[14] A. Firoozi, R. Khordad, A. Mohammadi, and T. Jalali, *Plasmon-exciton interactions in a spheroidal multilayer nanoshell for refractive index sensor application*. Eur. Phys. J. Plus. 136 (2021), pp. 1073.
[15] A. Taflove and S.C. Hagness, *Computational Electrodynamics: The Finite-Difference Time-Domain Method*, Artech House, New York, 2005.
[16] C. Hafner, *Post-modern Electromagnetics*, John Wiley, London, 1999.
[17] P. Cao, H. Chen, H. Zhang, L. Cheng, and T. Niu, *High-sensitivity refractive index of Au@$Cu_{2-x}S$ core–shell nanorods*. RSC Adv. 8 (2018), pp. 35005.
[18] A. Bonyár, I. Csarnovics, and G. Szántó, *Simulation and characterization of the bulk refractive index sensitivity of coupled plasmonic nanostructures with the enhancement factor*. Photonics Nanostruct.-Fundam. Appl. 31 (2018), pp. 1–7.
[19] D.D. Evanoff and G. Chumanov, *Size-controlled synthesis of nanoparticles. 2. Measurement of extinction, scattering, and absorption cross sections*. J. Phys. Chem. B 108 (2004), pp. 13957–13962.

Philosophical Magazine

ISSN: 1478-6435 (Print) 1478-6443 (Online) Journal homepage: www.tandfonline.com/journals/tphm20

A self-excitation point process model for quantifying nanoparticle agglomeration

Samarth Motagi, James Harris, Alberto Mello, Foram Madiyar & Sirish Namilae

To cite this article: Samarth Motagi, James Harris, Alberto Mello, Foram Madiyar & Sirish Namilae (2024) A self-excitation point process model for quantifying nanoparticle agglomeration, Philosophical Magazine, 104:22, 1011-1035, DOI: 10.1080/14786435.2024.2374530

To link to this article: https://doi.org/10.1080/14786435.2024.2374530

PHILOSOPHICAL MAGAZINE
2024, VOL. 104, NO. 22, 1011–1035
https://doi.org/10.1080/14786435.2024.2374530

Taylor & Francis
Taylor & Francis Group

A self-excitation point process model for quantifying nanoparticle agglomeration

Samarth Motagi, James Harris, Alberto Mello, Foram Madiyar and Sirish Namilae

Department of Aerospace Engineering, Embry-Riddle Aeronautical University, Daytona Beach, FL, USA

ABSTRACT

Nanoparticle agglomeration refers to the spontaneous clustering of nanoparticles caused by the attractive forces. Agglomeration impacts the physical and mechanical properties of nanoparticles and their composites. Understanding and controlling nanoparticle agglomeration is crucial for optimizing various applications, from nanomedicine to nanoelectronics. In this work, we formulated a self-exciting point process model to analyse nanoparticle agglomeration based on microstructural input. The model is utilised to categorise a specific set of points within the microstructure as either independent (dispersed) or dependent (agglomerated), along with their respective probabilities. We employed this approach to study two distinct scenarios: (a) Agglomeration in experimentally generated microstructures of titanium nanoparticles, and (b) Analysing agglomeration patterns in simulated microstructures of carbon nanotube networks, generated using a stochastic microstructure model. We obtain a quantitative understanding of the connection between the sonication duration and the level of agglomeration in titanium nanoparticles. As the sonication period increases, both the agglomeration percentage and the size of the agglomerates decrease. Furthermore, our analysis of simulated carbon nanotube microstructures, including equiaxed and rope-like agglomeration, shows a close alignment between results obtained from the point process model and those generated by the stochastic microstructure model.

ARTICLE HISTORY
Received 20 October 2023
Accepted 19 June 2024

KEYWORDS
Nanoparticle agglomeration; self-excitation point process model; titanium nanoparticles; carbon nanotubes

1. Introduction

Nanoparticles often possess distinct physical and chemical characteristics that differ from bulk materials, giving rise to unique behaviours. Agglomeration is one such phenomenon where nanoparticles come together, forming larger assemblies through spontaneous clustering or aggregation. The different factors that contribute to nanoparticle agglomeration, include van der Waals

CONTACT Sirish Namilae email-namilaes@erau.edu Department of Aerospace Engineering, Embry-Riddle Aeronautical University, Daytona Beach, FL, USA

forces, electrostatic interactions, surface chemistry, solvent effects, and external factors like temperature and pH [1–4]. Agglomeration of nanoparticles leads to several outcomes, including reduced surface area [5], altered optical properties [6], change in mechanical properties [7], and loss of homogeneity [8].

Various characterisation methods have been used to study nanoparticle agglomeration, such as dynamic light scattering [9], transmission electron microscopy (TEM) [10], scanning electron microscopy (SEM) [11], atomic force microscopy (AFM) [12], and spectroscopic methods [13]. Verleysen et al. [14] employed a quantitative approach for assessing stable dispersions, which involves TEM imaging in conjunction with semi-automated image analysis. This methodology yields number-based distributions of key parameters, allowing for the measurement of size, shape, and surface characteristics of TiO_2 particles in their unbound, aggregated, and agglomerated states. Rao et al. [15] employed AFM to analyse the morphology, dimensions, and size distribution of various ceramic nanoparticle agglomerates. Jia et al. [16] performed real-time sizing during the colloidal processing of metal oxide nanoparticles (MONs) using dynamic light scattering.

Modelling of nanoparticle agglomeration involves mathematical or computational approaches to simulate how nanoparticles cluster together, considering factors like size, shape, surface charge, environmental conditions, and external forces. Models often based on stochastic methods are used to understand agglomeration kinetics, predict agglomerate size distributions, and assess nanoparticle dispersion stability. Kim et al. [17] investigated the aggregation kinetics of gold nanoparticles through a combination of experimental methods and Monte Carlo simulations. This study predicts the time needed for the initial color change in a gold nanoparticle suspension, offering insights into the design and optimisation of colorimetric sensors utilizing gold nanoparticle aggregation. Liu et al. [18] applied a constant-number Direct Simulation Monte Carlo (DSMC) model to study nanoparticle agglomeration in aqueous suspensions. They used classical Derjaguin–Landau–Verwey–Overbeek (DLVO) theory, factoring in Brownian motion's effect on collision frequency. The model's outcomes aligned closely with dynamic light scattering measurements for particle size distribution and average agglomerate size. Morán et al. [19] introduce a new method to enhance the accuracy of Monte Carlo simulations for predicting dynamics and agglomeration of suspended nanoparticles. This approach incorporates persistent distance and time steps based on Langevin dynamics simulations and a probability model for particle displacements. Gbaguidi et al. [20,21] employed a two-dimensional Monte Carlo percolation model to investigate the impact of carbon nanotube (CNT) agglomeration on the electrical and electromechanical properties of both monofiller and hybrid nanocomposites. Bhoi et al. [22] developed a mathematical population balance model to characterize the evolution of Al_2O_3 nano-agglomerates

in a spouted bed. Agglomeration process is simulated using an Equipartition of Kinetic Energy (EKE) kernel, signifying the equal distribution of kinetic energy among particles, enabling collective formation into agglomerates. In contrast, for breakage, two distinct functions are employed: the Dirac delta function indicating immediate and concentrated particle breakage, and a function representing confined uniform binary breakage, where particles break into fragments with a uniform size distribution. The model exhibits good agreement with experimental observations concerning the temporal evolution of both the area and volume-weighted average sizes of nano-agglomerates, as well as their final size distribution.

In addition to stochastic methods, approaches like Molecular Dynamics have been used to understand the interparticle forces that contribute to agglomeration. Liao et al. [23] employed molecular dynamics simulations to investigate the factors that impact the formation of agglomeration structures in Cu–Ar nanofluids. Wang et al. [24] conducted equilibrium molecular dynamics simulations and the Schmidt–Ott equation to analyse the fractal dimensions of the nanoparticle aggregations with various morphologies. The findings suggested that achieving lower fractal dimensions can lead to enhanced thermal conductivity. Alian et al. [25] conducted molecular dynamic simulations that considered both the curvature and agglomeration of carbon nanotubes to analyse their influence on the interfacial strength and load transfer capacity in thermoset nanocomposites.

In this study, we introduce a new approach based on point process modelling to analyse nanoparticle agglomeration. A point process model is a statistical framework used to describe and analyse the spatial or temporal distribution of points or events in a particular region or over a specific period. Hawkes process, also known as self-exciting point process, is a branching point process model [26]. It describes a random sequence of clustered events or points wherein the presence of one point (or event) increases the likelihood of subsequent points (or events) occurring in its spatial or temporal vicinity. While the application of self-exciting point process models originated in the field of earthquake analysis to categorise mainshock and aftershock events from earthquake data, it has found applications across diverse domains. These domains include crime event analysis [27], tweet popularity prediction [28], epidemiological studies [29], as well as the analysis of instances involving mass killings and school shootings [30], email network [31], and financial data analysis [32].

The Hawkes process is parameterised by two functions, the background intensity, which describes the average rate of occurrence of events in the absence of any previous events. The excitation function, which describes how the occurrence of an event affects the probability of subsequent events. The parameters of self-exciting point process models can be estimated from data. This allows the models to be used to make predictions about future

events. Self-exciting point process models are a powerful tool for analysing sequences of events. They have been used to make significant contributions to a wide range of fields.

Hawkes point process model used in this study has the ability to capture spatial and temporal clustering, account for intensity variation, and facilitate statistical inference and prediction. Therefore, these models offer a novel statistical framework that can analyse the characteristics of agglomeration processes, making it a potentially effective approach. While this model has not yet been used in materials science and can bring a fresh perspective and could possibly be adapted to other similar materials science problems.

We apply this approach to analyse nanoparticle agglomeration in two distinct contexts: (a) experimentally generated microstructures of titanium nanoparticles, and (b) simulated microstructures of carbon nanotube agglomeration derived from a stochastic microstructure model. Experimental micrographs of titanium nanoparticles with various degrees of agglomeration were achieved by subjecting solutions with the same concentration to different durations of ultrasonic treatment. Simulated CNT microstructures exhibiting a range of agglomeration patterns for carbon nanotubes, including both equiaxed and rope-like morphologies were obtained using a stochastic microstructure model. Using these micrographs, we extracted the nanoparticle locations and applied a point process model to analyse the nanoparticle agglomeration. Our findings indicate that the point process model is an effective tool for analysing agglomeration and holds potential for further applications in nucleation-growth processes in materials science.

2. Methodology

2.1. Generation of experimental microstructures

99.9% pure spherical titanium nanoparticles – product number 1121XH from SkySpring Nanomaterials Inc., were procured for utilisation in this study. To prepare the nanoparticle solution, 0.001 g of titanium nanoparticle powder was combined with 8 ml of isopropyl alcohol (IPA), resulting in a solution with a concentration of 0.125 mg/ml. The SCILOGEX MX-T6-S Analog Tube Roller was employed to disperse titanium nanoparticles in the solution and reduce agglomeration. The nanoparticle solution inside a vial with SiC balls was placed within the tube roller for 24 h, operating at a speed of 50 rpm, effectively breaking apart the nanoparticle clusters and reducing the size of the agglomerates. Additionally, ultrasonication is employed to further break apart the nanoparticle agglomerates. Ultrasonication produces high-frequency sound waves within the liquid medium, resulting in the formation of pressure waves and cavitation bubbles. As these bubbles collapse, they generate micro-turbulence and shear forces, effectively dispersing and breaking the agglomerated nanoparticles [33]. Consequently, ultrasonication facilitates the

even distribution of nanoparticles throughout the liquid medium, serving as an effective measure to prevent or reduce agglomeration. Different levels of agglomeration were achieved by subjecting individual solutions to ultrasonic treatment for different durations with 5, 10, 20, 30, 60, 90 and 120 min. Subsequently, 40 µl droplets of each solution were dispersed onto an epoxy polymer substrate using a micro-pipette. The solution was immediately deposited onto the substrate within a minute of ultrasonication to prevent reagglomeration. To facilitate solvent evaporation, the prepared samples were subjected to a temperature of 50°C using an Aluminium top hotplate. The resulting micrographs displayed differing levels of nanoparticle agglomeration in the samples. Notably, the application of one hour or more of ultrasonic treatment duration was correlated with the uniform dispersion of the nanoparticles across the sample. Conversely, shorter durations of ultrasonic treatment resulted in a more noticeable agglomeration in the samples, as shown in Figure 1. When the as-prepared nanoparticle solution without sonication is used to generate microstructures, large agglomerates are present.

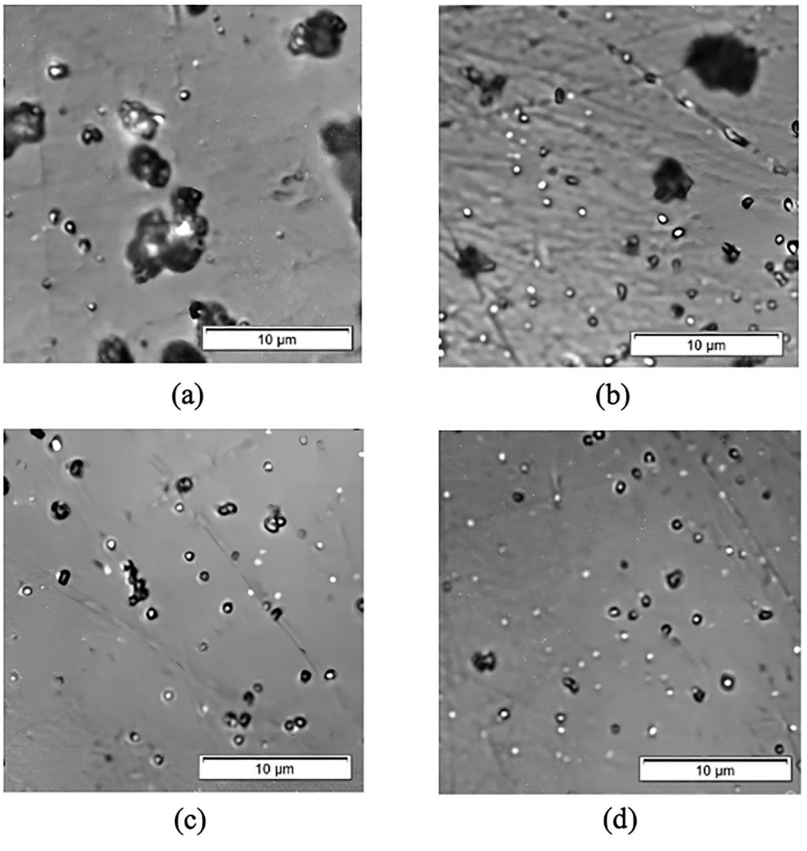

Figure 1. Titanium nanoparticles dispersed on the substrate at different sonication times (a) 5 min (b) 30 min (c) 1 h and (d) 2 h.

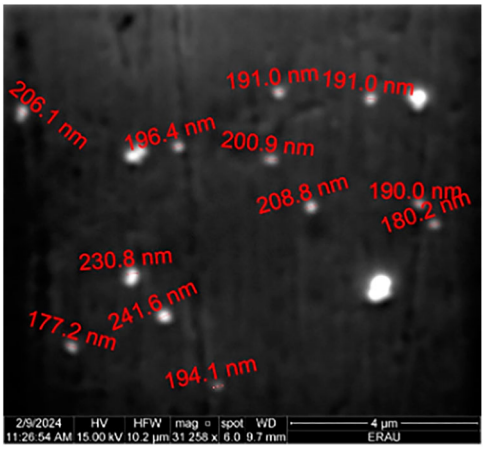

Figure 2. SEM micrograph of the nanoparticles after ultrasonication for 120 min.

The agglomerates reduce in size with increasing sonication duration. Additional sonication time did not reduce the particle size further. This particle size is measured using dynamic light scattering (DLS) measurements. After two hours of sonication, we observe that particles of about 200 nm size and are uniformly distributed.

We performed SEM micrographic analysis to further characterise the particle size distribution after ultrasonication for 120 min as shown in Figure 2. Scanning electron microscopy ascertained that the average particle size of titanium nanoparticles is 197 nm. Particle size is also confirmed using Dynamic Light Scattering – Malvern Zetasizer ZS90 to measure the size of particles in an IPA solution at 25°C. The technique relies on analysing the fluctuations in light scattering intensity caused by the Brownian motion of particles suspended in a liquid. By analysing the intensity fluctuations, DLS can determine the size of the particles in the solution, typically in the range of a few nanometres to a few micrometres. After 120 min of ultrasonication, the DLS measurements recorded a particle size of 195.37 nm and a zeta potential of −32.5 mV. This closely matches SEM analysis.

2.2. Generation of simulated microstructures

Simulated microstructures of agglomerated CNTs were generated using a stochastic microstructural model. These CNTs were generated within a Representative Area Element (RAE) with dimensions (L_x and L_y). Each CNT took the form of a line segment with a midpoint (x_{ic}, y_{ic}), a starting point (x_1^i, y_1^i), and an endpoint (x_2^i, y_2^i). Additionally, the length and polar angle of each CNT were represented by l_i and $Ø_i$, respectively. Different microstructures are generated by stochastically varying all of these parameters, simulating the complexity found in real-world microstructures. To calculate the volume fraction, all the

CNTs in the RAE are assumed to have a uniform diameter D_{CNT}. The CNT volume fraction is defined as the ratio of the total volume encompassed by all the CNTs ($\pi \times r_0^{i2} \times l_i$) to the area of the RAE ($L_x \times L_y$). To achieve the desired CNT volume fraction, nanotubes were added to the RAE until the specified volume fraction was attained. The centre of each CNT consistently falls within the confines of the RAE. In some instances, CNTs may intersect with one or even both edges of the RAE. To handle this situation, we employed periodic boundary conditions. These conditions efficiently relocated any line segments that extended beyond the RAE's boundaries, placing them on the opposite side of the RAE to ensure that they always remained contained within the RAE. The microstructure generation is described in detail in [34].

We modify this approach to generate microstructures featuring different quantities and morphologies of CNT agglomerates. This process begins with the generation of a seed layer consisting of completely randomised and uniformly distributed fillers. Subsequently, we introduce additional fillers in a manner that results in the formation of agglomerates around a portion of the initial seed layer. The total volume fraction of CNTs (V_f) within the RAE is determined by summing the volume fractions of both agglomerated (V_f^{agg}) and non-agglomerated CNTs $(V_f^{non-agg})$. The agglomeration level or volume fraction of agglomeration is then modelled by $\xi_{agg} = V_f^{agg}/V_f$. Two distinct microstructural configurations were generated by varying parameters related to agglomeration: the rope-like and equiaxed agglomerates. The formation of these structures was governed by two key parameters, ξ_{agg} and α_{agg}. The agglomeration parameter, ξ_{agg}, dictated the proportion of CNTs that were organised into agglomerates. For instance, when $\xi_{agg} = 0$, CNTs are uniformly distributed throughout the representative area element without any agglomeration. As ξ_{agg} increased, the degree of agglomeration increased. When $\xi_{agg} =$ 10%, in the first step the CNTs are uniformly distributed throughout the RAE without any agglomeration and then the additional small fraction of CNT fillers is added which results in the formation of agglomerates. Similar, procedure is carried out for varying levels of CNT agglomeration. The agglomeration angle, α_{agg}, is used to model the spatial arrangement of CNTs within an agglomerate. The newly added CNTs are positioned at a randomly varied angle between 0 and α_{agg} with respect to one of the pre-existing CNTs in the microstructure. When $\alpha_{agg} = 0°$, CNTs within an agglomerate are all aligned in parallel, resulting in the formation of rope-like agglomerates within the microstructure. Conversely, when $\alpha_{agg} = 180°$, CNTs within an agglomerate exhibit varied orientation, giving rise to equiaxed or star-like agglomerate formations. Figure 3 (a) and (b) illustrated microstructures showcasing the equiaxed and rope-like agglomerates, respectively, with agglomeration level of 50%. These details are presented in detail in [21]. For each agglomeration level, 25 microstructures were generated from the stochastic model to account for statistical variations in the point process agglomeration analysis.

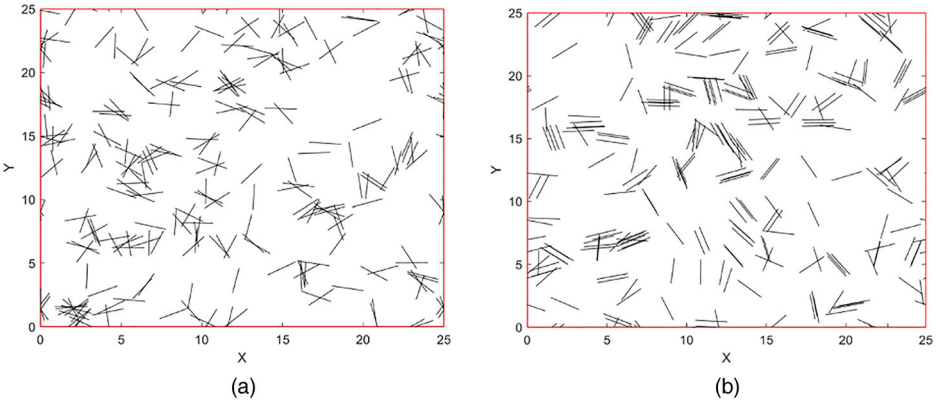

Figure 3. (a) Equiaxed agglomeration and (b) Rope-like agglomeration of carbon nanotubes.

2.3. Point process model formulation for agglomeration analysis

Consider a microstructure that consists of N points which represent the location of nanoparticles. r_i is the distance of a point i from origin.

$$\lambda(r) = \mu + \sum_{i:r_i<r} g_{A,\,\alpha}(r - r_i). \tag{1}$$

Here, λ is the limiting expected distribution of points. The model classifies the nanoparticles in the dataset into two categories, uniformly dispersed nanoparticles and agglomerated nanoparticles. Uniformly dispersed nanoparticles are assumed to be distributed independently at an areal density $\mu > 0$. This model primarily addresses discrete agglomeration state as described by a micrograph at a given location and time.

$g_{A,\alpha}(r - r_i)$ is the probability density function (PDF) of the occurrence of an agglomerated nanoparticle at a distance r_i and is modelled as follows:

$$g_{A,\alpha}(r - r_i) = \begin{cases} A * \alpha * \exp[-\alpha * (r - r_i)], & r > r_i\,, \\ 0 \qquad\qquad\qquad\qquad\quad , & r \le r_i. \end{cases} \tag{2}$$

The conditional intensity function $\lambda(r|H_r)$ can now be expressed as follows:

$$\lambda(r) = \mu + A \sum_{i:r_i<r} \alpha.e^{-\alpha(r-r_i)}. \tag{3}$$

In this case, α denotes the decay rate in distance for the occurrence of an agglomerated nanoparticle, and A is the preexponential parameter describing the magnitude of excitation. Notably, $g_{A,\alpha}$ is the function that describes the delta $r - r_i$ between an agglomerated and corresponding uniformly dispersed seed nanoparticle. The model is defined by three unknown parameters $\theta = (\mu,\ A,\ \alpha)$. While fitting the model to the microstructure data, these parameters are computed using maximum likelihood estimation. The log-

likelihood function [35] is given a distance series of microstructure data consisting of N points $\{(r_i),\ i = 1, \ldots, N\}$ in an area.

$$l(\theta|H_r) = \sum_{i=1}^{N} log\lambda_\theta(r_i|H_{ri}) - \int_0^R \lambda_\theta(r|H_r)dr. \tag{4}$$

The Davidon–Fletcher–Powell (DFP) approach, a gradient-based nonlinear optimisation procedure, is used to derive the maximum likelihood estimate (MLE) [32]. The DFP method works by iteratively updating an approximation to the inverse Hessian matrix. This approximation is used to generate a search direction, which is then used to update the current estimate of the minimum. The process is repeated until the convergence criteria are met. The probability that point i triggered point j, i.e. the probability that a nanoparticle j is in an agglomerate with nanoparticle i as a seed is given by:

$$p_{ij} = \begin{cases} \dfrac{g_{A,\alpha}(r_j - r_i)}{\lambda(r_j|H_{r_j})} & , r_j > r_i, \\ 0 & , r_j \le r_i. \end{cases} \tag{5}$$

Hence, the probability of nanoparticle j being an agglomerated nanoparticle is $p_j = \sum_{i=1}^{j-1} p_{ij}$. Consequently, the probability of nanoparticle j being a uniformly dispersed nanoparticle is:

$$1 - p_j = \frac{\mu}{\lambda(r_j|H_{r_j})}. \tag{6}$$

Based on the probability values p_j obtained from the model of N nanoparticle points can be classified into uniformly dispersed and agglomerated nanoparticles. This categorisation allows us to compute the microstructure's agglomeration level and the average agglomeration size of nanoparticles in a given microstructure. Pseudocode outlining the algorithm of the Hawkes point process model is shown in Figure 4.

The point process model described above relies on input data consisting of the distances of individual nanoparticles from the origin. To acquire these data, we first need to extract the nanoparticle locations from both experimental and simulated microstructures. We employed a widely used tool WebPlotDigitizer [36] to extract nanoparticle positions from the experimental microstructures. In the case of simulated microstructure, the centre of the CNT location is extracted directly from the model data. Subsequently, we calculated the distance of individual nanoparticle from the origin. This data is used as an input for the point process model.

Two or more nanoparticles at different angles may have the same radial distance from the origin. To avoid the overlapping of such nanoparticles, segments are created to allocate unique locations for the CNTs as shown in Figure 5. If any of the clustered nanoparticles (especially CNTs) are split across segments,

Algorithm: Simulation of Hawkes Point Process Model

1. Extract the location of each of the N nanoparticle in the RAE. (For both experimentally and computationally generated microstructures.)
2. Calculate the distance from the origin (r_i) *for particle i*. Find $\{(r_i), i = 1, \ldots, N\}$.
3. Find background intensity rate $\mu(r)$ corresponding to uniformly distributed microstructure with no agglomerates.
4. Calculate the conditional intensity function $\lambda(r) = \mu + \sum_{i:r_i<r} g_{A,\alpha}(r - r_i)$ in the space interval R= [s_{start}, s_{end}] for a given background intensity $\mu(r)$.
5. **inputs:**
   θ_0 - initial guess for the model parameters $\theta = (\mu, A, \alpha)$
   $\mu(r)$ - background rate
   k - 0
6. **Start loop**
7. use θ_k and get θ_{k+1}
8. $p_i = \frac{\mu}{\lambda(r_j|H_{r_j})}$ - Probability values for uniformly dispersed nanoparticles
9. k = k+1
10. **until** $l(\theta|H_r) = \sum_{i=1}^{N} log\lambda_\theta(r_i|H_{ri}) - \int_0^R \lambda_\theta(r|H_r)dr$ - Maximum Likelihood Estimation is optimized for the model parameters $\theta = (\mu, A, \alpha)$
11. **return** θ_k
12. **Post analysis:** based on the probability values obtained from the model nanoparticles are classified as dispersed (when $p_i < 0.9$) or agglomerated particles (when $p_i > 0.9$)
13. Based on the probability values and particle locations agglomeration levels and agglomerate sizes are quantified for a given microstructure

Figure 4. Pseudocode outlining the algorithm of Hawkes Point Process Model.

then the particles that are closest to one another are forced to fall within the same segment. Figure 5 shows two CNT clusters inside segments 1 and 4; in this example, the nanoparticles are assigned a unique position within their respective segments. In this case, when we see that one cluster is split across two segments (i.e. segments 2 and 3), so we create a buffer segment to ensure that the cluster is not divided across the segments, and any particles that are close by within the buffer segment are considered in the same segment. In this scenario, CNTs are considered in segment 2 and ignored in segment 3 to avoid recurrence. These scenarios are more common for high aspect ratio particles like CNTs.

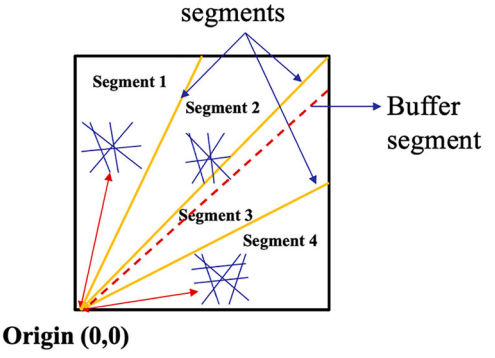

Figure 5. Allocation of unique location to CNTs in a micrograph.

3. Results

3.1. Analysis of experimental microstructures

The digitised nanoparticle positions from the experimental micrographs captured at various sonication times are as shown in Figure 6. Due to the limited contrast between the nanoparticles and the substrate, we used a manual process to extract the nanoparticle locations. However, this process can be easily automated using higher contrast particles. Once we have obtained the nanoparticle location data, we utilise MATLAB code to create segmentation that assigns unique identifiers to these locations as explained in Section 2.3. This dataset is used as input for the point process model, enabling the classification of nanoparticles into two categories: those that are uniformly dispersed and agglomerated nanoparticles.

The point process model provides output in terms of probability values that play a crucial role in classifying nanoparticle behaviour. Equation (5) is used to compute the probability that a given particle is uniformly dispersed. This probability value is the basis for the classification of all points as independent (i.e. dispersed) or dependent (i.e. part of an agglomerate. All agglomerates will still contain one particle that is classified as an independent point and the surrounding particles close to this independent particle would have low probability values indicating that they are a part of the agglomerate. The choice of the probability value 0.8 was determined as a threshold through visual examination, where it was noted that nanoparticles are in an agglomerated state when the probability that they are independent was below 0.8. Figure 7 shows the microstructure of titanium nanoparticles alongside a corresponding contour plot of

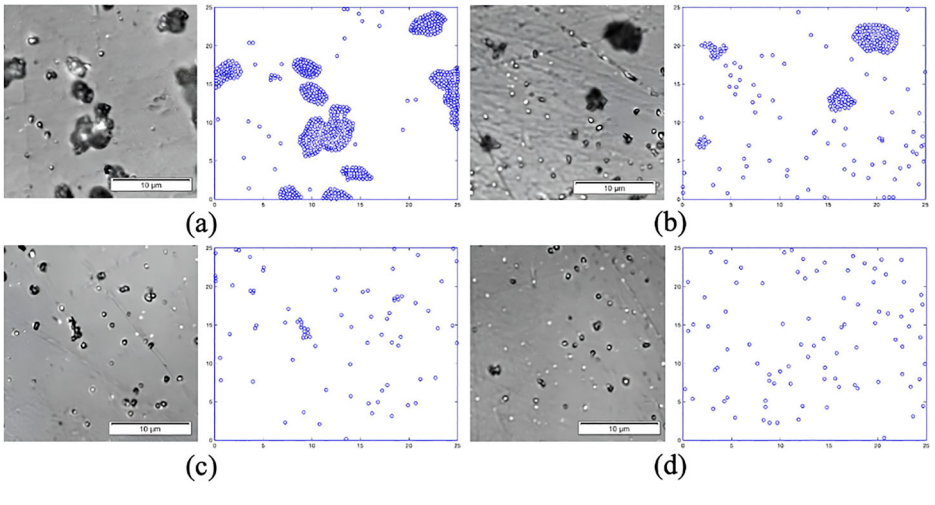

Figure 6. Extracted titanium nanoparticle location dispersed on the substrate at different sonication time (a) 5 min (b) 30 min (c) 1 h and (d) 2 h.

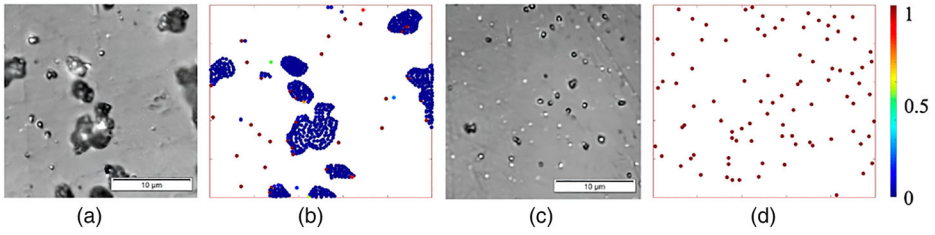

Figure 7. (a) Titanium microstructure sonicated after 5 min, (b) contour plot based on probability values form the model for sonication time 5 min, (c) titanium microstructure sonicated after 2 h and (d) contour plot based on probability values for sonication time 2 h. Note the contour legend corresponds to both (a) and (b), the size of the micrographs is 25 μm × 25 μm.

the probability values. After undergoing 5 min of sonication, the microstructure exhibits a relatively high level of agglomeration. The corresponding contour plot for most particles depicts a low probability that the particles are not agglomerated, indicating high levels of nanoparticle agglomeration. Conversely, the titanium microstructure subjected to 2 h of sonication tends to exhibit much lower levels of agglomeration. In the figure, the corresponding contour plot reveals higher probability values, depicted in red, signifying uniformly dispersed nanoparticles.

We investigated the agglomeration behaviour of titanium nanoparticles in relation to varying sonication durations. Commercially available titanium nanoparticles in a dry powder state are found to be agglomerated into particles that are several hundred nanometres in size [37, 38]. For each specific sonication duration, we capture three micrographs and subsequently quantify the agglomeration percentage based on the probability values generated by the point-process model. The findings presented in Figure 8 illustrate that a higher percentage of titanium nanoparticle agglomeration is observed when sonication times are shorter. It is quite evident that when a shorter duration of ultrasonication was employed, it was insufficient to effectively disperse the nanoparticle agglomerates, consequently resulting in a higher agglomeration percentage. As we progress from sonication duration A to G (see Figure 7), the agglomeration percentage consistently decreases indicating that a higher duration of ultrasonication results in uniform dispersion of the nanoparticles. The error bars depicted in Figure 7 signify the standard deviation of the nanoparticle agglomeration percentage corresponding to each sonication duration. This trend signifies that the nanoparticle agglomerates gradually break apart as the sonication time extends. The model can effectively capture the dynamic relationship between sonication duration and titanium nanoparticle agglomeration.

Once the nanoparticle classification as dispersed or agglomerated particles is completed, we employ a post-processing MATLAB code to determine the size of the nanoparticle agglomerate. This is accomplished by identifying

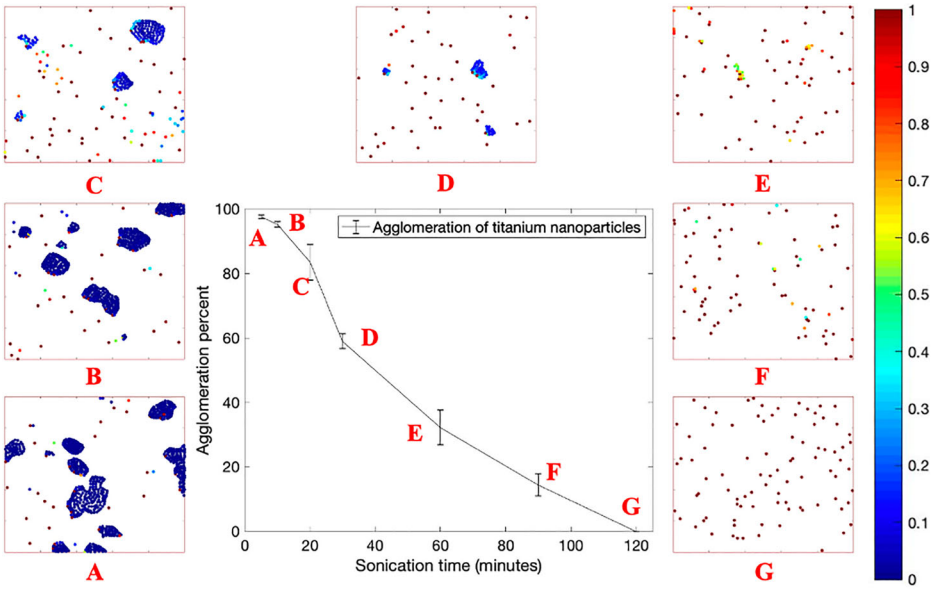

Figure 8. Agglomeration of titanium nanoparticles with respect to sonication time. Note the contour legend corresponds from A to G micrographs and the size of the micrographs is 25 μm × 25 μm.

agglomerate boundary based on the aforementioned probability values. Given that our input data consists of a sequential series of nanoparticle distances from the origin. We use the probability values to identify continuous sequences of values that consistently fall below 0.8. This pattern of consecutive low values is indicative of the existence of nanoparticle clusters. In contrast, if the values remain consistently above 0.8, it signifies that the nanoparticles are uniformly dispersed. By adopting this method, we can pinpoint nanoparticle agglomerate clusters and calculate the size of a given agglomerate, and the average agglomeration size for the micrograph. In Figure 9, as we progress from point A to point F, corresponding to increasing sonication times, it becomes evident that the agglomeration size consistently decreases. This observation indicates the gradual breakdown of nanoparticle agglomerates in response to longer sonication times.

To validate the point process model results, we compared the point process agglomeration analysis with microstructural analysis. The agglomeration statistics were manually extracted from the same micrographs that were used for point process analysis. The comparison between the two approaches shown in Table 1 indicates that point process model accurately captures the agglomeration behaviour.

3.2. Analysis of simulated microstructures

The same methodology is applied to the simulated microstructures containing carbon nanotubes, generated within a Representative Area Element measuring

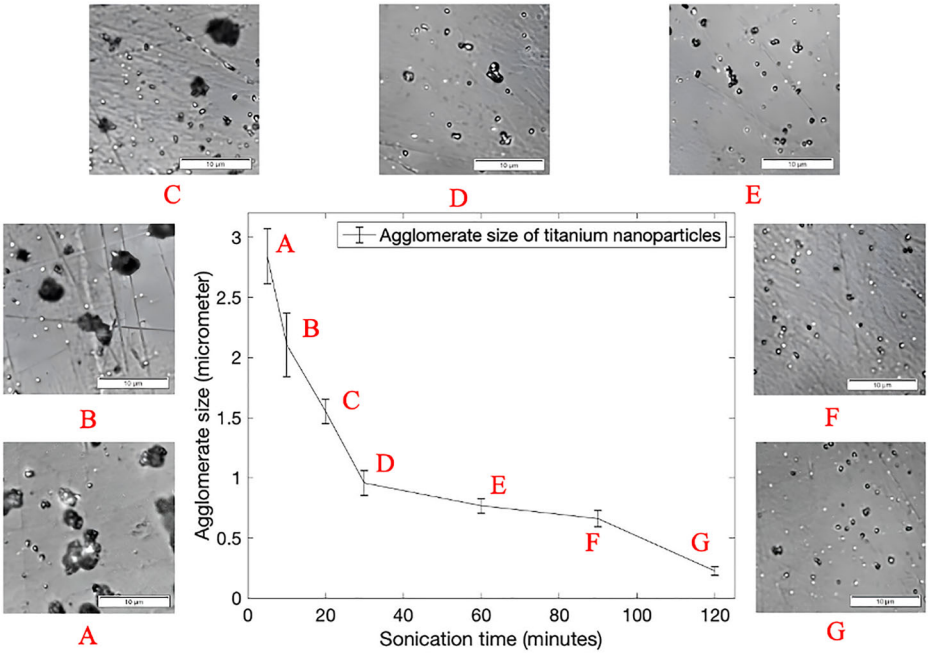

Figure 9. Agglomerate size of titanium nanoparticles with respect to sonication time.

25×25 micrometres. In Figure 10, we present a randomly generated microstructure, featuring a 50% agglomeration of CNT nanoparticles. We can discern two distinct nanoparticle behaviours as depicted in the figure. First, we observe CNT nanoparticle entanglement, which is referred to as agglomerated nanoparticles. Second, there are uniformly dispersed CNT nanoparticles, which appear isolated without nearby CNTs or entanglements. To distinguish between these two behaviours, we utilise a point-process model to calculate probability values for the classification. The corresponding contour plot in Figure 10 represents these nanoparticles based on the probability values obtained from the model. Equation (5) serves as the probability equation for uniformly dispersed nanoparticles, forming the foundation for classification. When the value derived from this equation is below 0.8, it indicates that the nanoparticles are in an agglomerated state. Conversely, when the value

Table 1. Comparison of point process results with manual microstructural analysis in terms of agglomerate size.

Ultrasonication time	Microscopic analysis Mean agglomerate size	Point process analysis Mean agglomerate size	% Difference
5 min	2939 nm	2842 nm	3.3
10 min	1009 nm	956 nm	5.2
1 h	744 nm	768 nm	−3.2
2 h	199 nm	226 nm	−13.56

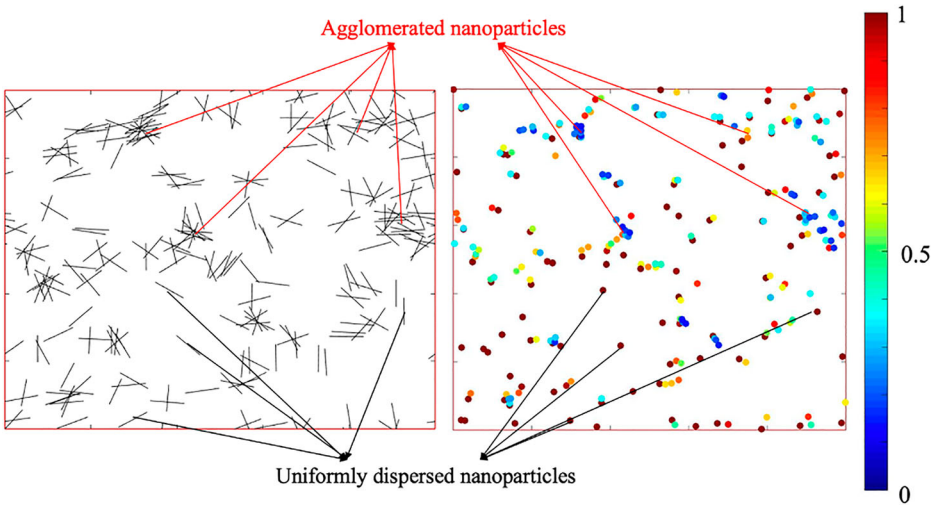

Figure 10. Randomly generated microstructure with 50% agglomeration of CNT nanoparticles and contour plot of representation of nanoparticles based on probability values obtained from point-process model.

exceeds 0.8, it signifies uniform dispersion of the nanoparticles. Uniformly dispersed nanoparticles are depicted as orange to red nanoparticles in the contour plot. In contrast, agglomerated nanoparticles are represented as yellow to blue dots in the contour plot. This approach allows us to effectively differentiate between uniformly dispersed and agglomerated CNT nanoparticles within the simulated microstructure, which helps to quantify nanoparticle agglomeration characteristics.

3.2.1. Equiaxed vs. rope-like agglomerated microstructures

Based on the processing conditions, agglomerates in carbon nanotubes have been found to exhibit two types of morphologies: equiaxed [39, 40] and rope-like [41, 42]. Equiaxed agglomeration of carbon nanotubes refers to a specific clustering pattern of CNTs where the agglomerates take on spherical or star-like shapes. In Figure 11, we can see that the simulated microstructure transitions from uniformly dispersed CNTs to various levels of equiaxed agglomerated microstructures, and this transformation is achieved using a stochastic microstructure model. To quantify these changes, corresponding contour plots represent the probability that a given CNT is in a dispersed state. These values are derived from a point process model. In the first micrograph (a), where CNTs are uniformly dispersed, the probability values are close to 1. This signifies that the CNTs are evenly distributed throughout the microstructure with minimal clustering. As we progress to micrographs (b), (c), and (d), we observe a decrease in probability values, indicating higher levels of agglomeration in the micrographs. In (b), with 30% agglomeration, some

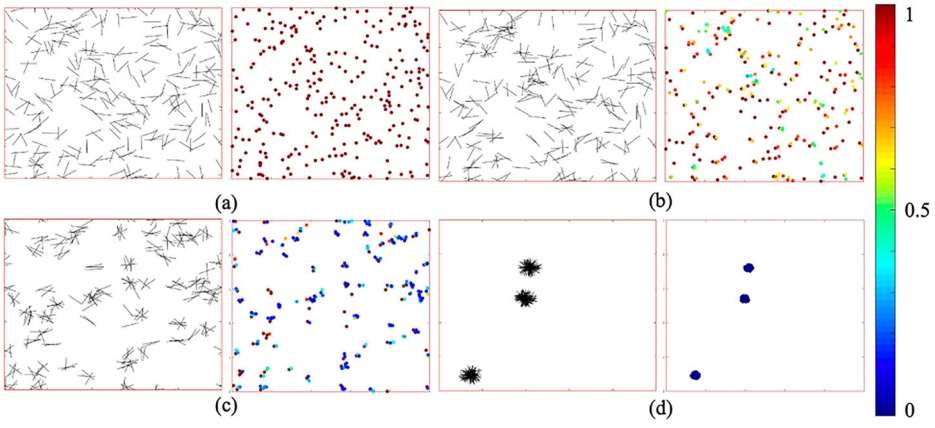

Figure 11. Randomly generated microstructure and contour plot of CNT nanoparticles based on probability values (a) 0% agglomeration (b) 30% agglomeration (c) 70% agglomeration and (d) 99% agglomeration. Note that the size of the micrographs is 25 μm × 25 μm.

clustering of CNTs has begun to occur. In (c), with 50% agglomeration, the clustering becomes more pronounced. Finally, in (d), with 99% agglomeration, the probability value is at its lowest, signifying that a significant portion of CNTs has aggregated into equiaxed agglomerates, forming spherical or star-like structures.

In contrast to equiaxed agglomeration, rope-like agglomeration of carbon nanotubes refers to bundling together CNTs parallel to each other into structures that resemble ropes or fibres. Figure 14 shows the evolution of the simulated rope-like microstructures, varying from uniformly dispersed to increasing levels of rope-like agglomeration. These variations are obtained by changing the input parameters to the stochastic microstructure model as described in Section 2.2. Figure 12 displays simulated micrographs and corresponding contour plots indicating the probability of CNT dispersion. For the completely dispersed state shown in Figure 12 (a), the probability values are close to 1. This signifies that the point process model computes that the CNTs are uniformly distributed throughout the microstructure, with minimal clustering. Figure 10b–d presents micrographs with increasing agglomeration and corresponding probability contours. For both rope-like and equiaxed agglomerated microstructures, the point process model computes the dispersion probabilities effectively which are used for further analysis.

We employed the point process model to categorise nanoparticle distributions as either uniformly dispersed or agglomerated and used this information to quantify the level of agglomeration within a given microstructure. We analysed 25 microstructures of specific agglomeration characteristics to account for statistical variation. We find that the results independently obtained from the point process model closely align with the input parameters used by the stochastic microstructure model to model the microstructures.

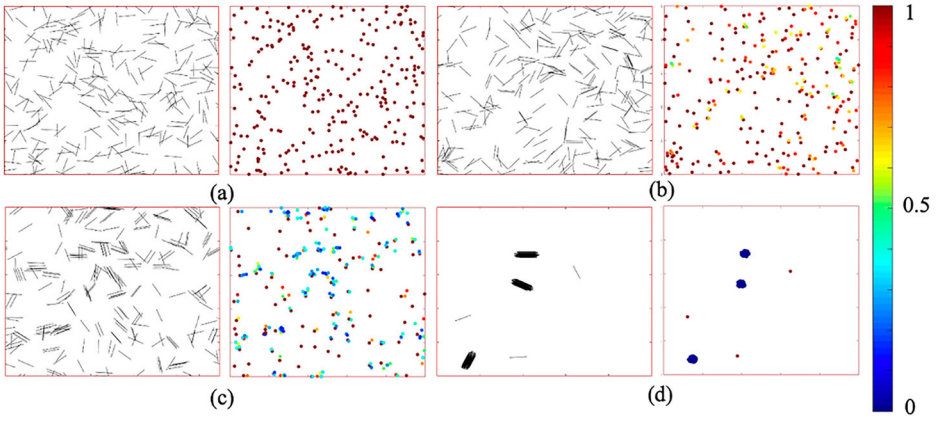

Figure 12. Rope-like generated microstructure and contour plot of CNT nanoparticles based on probability values (a) 0% agglomeration (b) 30% agglomeration (c) 70% agglomeration and (d) 99% agglomeration.

Error bars represent the standard deviation associated with the nanoparticle agglomeration percentages. Figure 13 shows these results for equiaxed microstructure and similar results for rope-like microstructures are shown in Figure 14.

3.2.2. Agglomerate size variation

We utilised the same post-processing MATLAB code used for experimental microstructures, to analyse the size of the nanoparticle agglomerates for the simulated microstructures as well. Figure 15 presents the average agglomerate size for a given agglomeration percentage for both equiaxed and rope-like microstructures. For equiaxed and rope-like agglomerates, the agglomeration size consistently increases with a corresponding rise in the agglomeration percentage. The equiaxed agglomerate exhibits a larger agglomerate size compared to the rope-like agglomerate. This size difference arises from the distinctive star-like shape found in equiaxed agglomerates, whereas rope-like agglomerations are characterised by their fiber-like structure. The reduction in agglomeration size in the rope-like formation is attributed to the alignment of carbon nanotubes, causing a decrease in size along the radial direction. This alignment results in an overall decrease in agglomeration size at higher rates of agglomeration.

4. Discussion

Controlled agglomeration offers the advantage of tailoring material properties to meet specific performance requirements. For instance, as agglomeration increases, particle-to-particle distances shorten, intensifying magnetic dipole interparticle interactions. This results in a more pronounced ferromagnetic

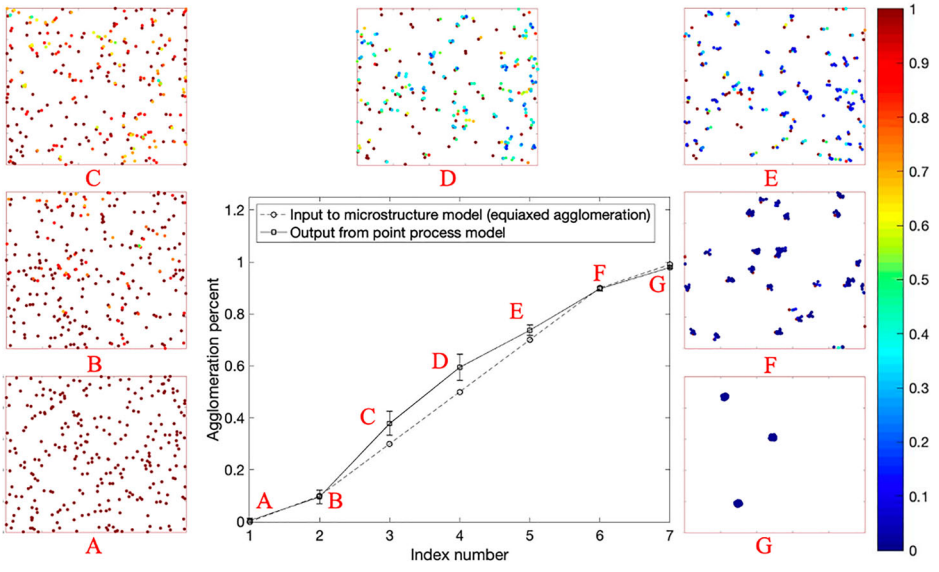

Figure 13. Comparison of percentage of agglomerated microstructure generated from stochastic model with the point process model.

behaviour with hysteresis losses, valuable for tumour treatment by selectively targeting cancer cells without harming surrounding healthy tissue [43]. Conversely, nanoparticle agglomeration can diminish the potential improvement in mechanical properties in nanocomposites due to restricted interfacial area. In orthopaedic applications [44], ceramic nanoparticles inherent

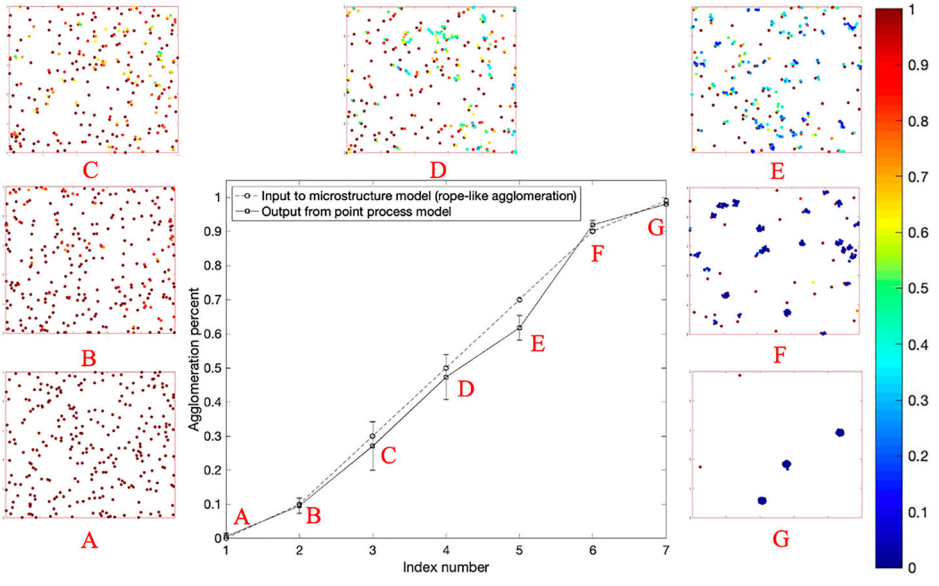

Figure 14. Comparison of percentage of rope-like agglomerated microstructure generated from stochastic model with the point process model.

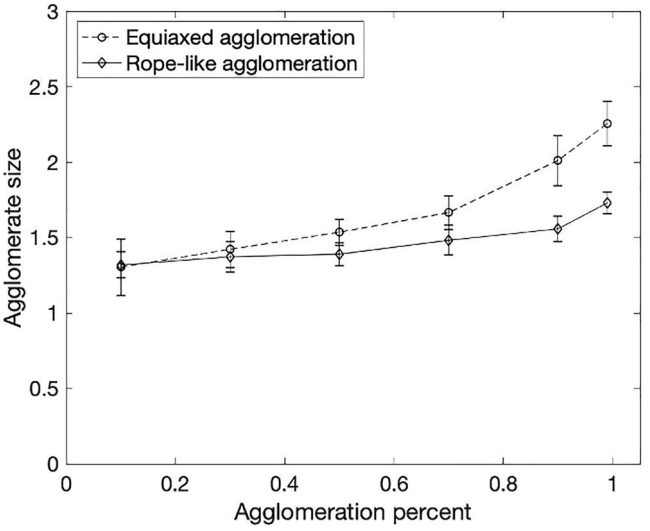

Figure 15. The average agglomeration size with error bars is represented for equiaxed and rope-like agglomerate with respect to agglomeration percent.

tendency to form larger agglomerates in a polymer matrix compromise mechanical performance. In materials' microstructure characterisation, nanoparticles have played an important role in determining strain maps and finding strain localisations via digital image correlation (DIC). In this case, properly dispersed particles must cover the area of interest, allowing the construction of displacement fields [45, 46]. The growing use of nanoparticles in everyday products raises concerns about their release into water sources and wastewater. In water treatment and wastewater sludge, nanoparticles and agglomerates with particle sizes less than 100 nm can be slow settling, prolong suspension, and hinder effective removal, increasing the risk of environmental toxicity [47]. Agglomerated nanoparticles often possess reduced effective surface areas compared to individual dispersed nanoparticles, limiting reactivity critical in applications like catalysis [48]. Additionally, agglomerates may exhibit diminished mobility and diffusion rates, impacting their effectiveness in applications requiring free nanoparticle movement, such as drug delivery [49]. Therefore, it is of utmost importance to gain a comprehensive understanding of nanoparticle behaviour with regard to aspects such as morphology, agglomeration percentage, agglomeration size, and associated factors.

Mathematical models to describe and predict nanoparticle agglomeration provide invaluable insights into the complex dynamics of nanoparticles coming together, forming clusters, and influencing various material properties. Several modelling approaches including stochastic percolation models [50], fractal analysis [51], Smoluchowski equation [52] and Kinetic Monte Carlo [53] have been used to study agglomeration. These models describe how

nanoparticles come together and form aggregates over time, taking into account factors such as particle concentration, collision frequency, and the probability of aggregation. Despite these developments, there is a limited correlation between modelling and experimental studies. Furthermore, there is a lack of modelling approaches that can quantitatively analyse a given experimental or simulated microstructure for agglomeration characteristics. The point process model proposed in this study effectively addresses this aspect.

Statistical methods offer distinct advantages in quantifying the agglomeration phenomenon compared to analytical methods. Considering the inherent stochasticity of agglomeration processes, statistical methods provide a robust framework for analysing and interpreting data. Unlike analytical techniques, statistical methods allow researchers to not only describe the central tendencies of agglomeration phenomena but also assess the variability, distribution, and trends within datasets, as well as quantify uncertainties and reveal patterns and correlations that might be overlooked by purely analytical methods. Self-exciting point process is an effective approach to model discrete history-dependent interrelated spatio-temporal events or points. Consequently, it has been used extensively in various domains with such data including earthquake occurrences [35], epidemiology[28], crime [26], financial markets [54], etc.

Despite the success of Hawkes point process models in various domains, they have not been utilised in materials science. To our knowledge, this study represents the first application of the Hawkes point process model to a problem in materials science. Self-excitation point process models are well-suited for analysing agglomeration due to the following reasons: (a) Discretisation: Point process models handle discrete points or events in the spatiotemporal domain. In the context of agglomeration, these discrete points can represent individual nanoparticles which are either dispersed or in clusters. (b) History or Path Dependence: Another prerequisite for applying point process models is the history dependence of the events or points. Agglomeration processes inherently exhibit history dependence, meaning the current state of agglomeration is influenced by the existing locations of the particles. The applied model uses a 2D dataset but holds the potential for adaptation to 3D datasets. For adapting to 3D, one would use volumetric data and convert x, y, and z positions to distance from origin in sub cells. This would be similar to the procedure described in section 2.3 except for including volumetric slices instead of planar segments. However, this would complicate the model and require 3D characterisation data. Some of the techniques used for 3D characterisation of nanoparticles include X-ray computed microtomography [55], confocal laser scanning microscopy [56] and transmission electron microscopy [57].

We acknowledge the limitations of optical microscopy, particularly when working with complex structures in three dimensions. Optical microscopy, while valuable for visualizing particle distributions, has inherent resolution limits that can introduce uncertainties in size measurements and the detailed

characterisation of nanoparticle agglomerates. These uncertainties primarily arise from diffraction limits and the inability to resolve features below the wavelength of light used in the microscope. Therefore, we complemented optical microscopy with Scanning Electron Microscopy (SEM) and Dynamic Light Scattering (DLS) spectroscopy to characterize the particle size distributions for high ultrasonication times. Another limitation is with respect to particle count. In the microstructures we have considered, the particle count varies from 621 to 89. The background rate used in the calculation is dependent on the number of particles. It is always desirable to analyse microstructures with a larger number of particles.

Here we have quasi-statically analysed the agglomeration in microstructures. The model and methodology are highly adaptable and can be readily extended to accommodate dynamic processes. For instance, the analysis in Figure 8, presents an opportunity to explore the spatiotemporal evolution of microstructures under the influence of sonication. By transitioning from quasi-static analysis to dynamic analysis, one can examine how microstructures change over time as a result of sonication. This will facilitate the time-dependent behaviour and responses of such structures and applications. Furthermore, many phenomena in material science can be discretised and have path dependence. For example, nucleation growth processes like solidification and equilibrium phase transformations. The self-excitation point process models can potentially be used for analysing such processes.

5. Conclusion

This study presents an innovative application of the self-exciting point process model to investigate nanoparticle agglomeration. Experimentally generated titanium nanoparticle microstructures were analysed, revealing a direct correlation between sonication duration and nanoparticle agglomeration. With increasing sonication time, it was observed that a simultaneous reduction in both agglomeration percentage and size. Additionally, our analysis extends to simulated carbon nanotube microstructures, encompassing a wide range of agglomeration patterns, including equiaxed and rope-like morphologies. The outcomes derived from the point process model align closely with those obtained from the microstructure model. Agglomeration size consistently increases alongside the agglomeration percentage for equiaxed and rope-like agglomerates, with equiaxed structures displaying larger agglomerates due to their star-like shape, while rope-like agglomerations are defined by their fibre-like structure. This study demonstrates that self-exciting point process models can be used for analysing phenomenon in materials science that can be broken down into discrete events or points, and exhibit path dependence. While we focus on agglomeration in this study, the approach can potentially be extended to other nucleation and growth-type processes.

Acknowledgement

This material is based upon work supported in part by the National Science Foundation under Grant numbers 2001038 and 2050887. The opinions, findings, conclusions, or recommendations expressed are those of the author(s) and do not necessarily reflect the views of the National Science Foundation.

Disclosure statement

No potential conflict of interest was reported by the author(s).

Funding

This work was supported by National Science Foundation [Grant Number 2001038, 2050887].

Data availability statement

We have added the supplemental data including microstructure images and computational codes to a GitHub repository. It can be accessed through the following link https://github.com/AMMG-at-ERAU/Nanoparticle-Agglomeration.

References

[1] I. Chowdhury, S.L. Walker, and S.E. Mylon, *Aggregate morphology of nano-TiO2: role of primary particle size, solution chemistry, and organic matter*. Environ. Sci: Processes Impacts 15 (2013), pp. 275–282.

[2] Y. Nur, J.R. Lead, and M. Baalousha, *Evaluation of charge and agglomeration behavior of TiO2 nanoparticles in ecotoxicological media*. Sci. Total Environ. 535 (2015), pp. 45–53.

[3] M. Zareei, H. Yoozbashizadeh, and H.R. Madaah Hosseini, *Investigating the effects of pH, surfactant and ionic strength on the stability of alumina/water nanofluids using DLVO theory*. J. Thermal Anal. Calorimet. 135 (2019), pp. 1185–1196.

[4] J. Jiang, G. Oberdörster, and P. Biswas, *Characterization of size, surface charge, and agglomeration state of nanoparticle dispersions for toxicological studies*. J. Nanoparticle Res. 11 (2009), pp. 77–89.

[5] K. Suttiponparnit, J. Jiang, M. Sahu, S. Suvachittanont, T. Charinpanitkul, and P. Biswas, *Role of surface area, primary particle size, and crystal phase on titanium dioxide nanoparticle dispersion properties*. Nanoscale Res. Lett. 6 (2011), pp. 1–8.

[6] S. Arya, P. Mahajan, S. Mahajan, A. Khosla, R. Datt, V. Gupta, S.J. Young, and S.K. Oruganti, *Review—influence of processing parameters to control morphology and optical properties of sol-gel synthesized ZnO nanoparticles*. ECS J. Solid State Sci. Technol. 10 (2021), pp. 23002.

[7] Y. Zare, *Study of nanoparticles aggregation/agglomeration in polymer particulate nanocomposites by mechanical properties*. Compos. A: Appl. Sci. Manuf. 84 (2016), pp. 158–164.

[8] R. Qiao, H. Deng, K.W. Putz, and L.C. Brinson, *Effect of particle agglomeration and interphase on the glass transition temperature of polymer nanocomposites*. J. Polym. Sci. B: Polym. Phys. 49 (2011), pp. 740–748.

[9] R.C. Murdock, L. Braydich-Stolle, A.M. Schrand, J.J. Schlager, and S.M. Hussain, *Characterization of nanomaterial dispersion in solution prior to in vitro exposure using dynamic light scattering technique*. Toxicol. Sci. 101 (2008), pp. 239–253.
[10] W.G. Shin, J. Wang, M. Mertler, B. Sachweh, H. Fissan, and D.Y.H. Pui, *Structural properties of silver nanoparticle agglomerates based on transmission electron microscopy: relationship to particle mobility analysis*. J. Nanoparticle Res. 11 (2009), pp. 163–173.
[11] A.M. Horst, A.C. Neal, R.E. Mielke, P.R. Sislian, W.H. Suh, L. Mädler, G.D. Stucky, and P.A. Holden, *Dispersion of TiO_2 nanoparticle agglomerates by* pseudomonas aeruginosa. Appl. Environ. Microbiol. 76 (2010), pp. 7292–7298.
[12] R.D. Boyd, S.K. Pichaimuthu, and A. Cuenat, *New approach to inter-technique comparisons for nanoparticle size measurements; using atomic force microscopy, nanoparticle tracking analysis and dynamic light scattering*. Colloids Surf. A: Physicochem. Eng. Asp. 387 (2011), pp. 35–42.
[13] S. Bandyopadhyay, J.R. Peralta-Videa, J.A. Hernandez-Viezcas, M.O. Montes, A.A. Keller, and J.L. Gardea-Torresdey, *Microscopic and spectroscopic methods applied to the measurements of nanoparticles in the environment*. Appl. Spectrosc. Rev. 47 (2012), pp. 180–206.
[14] E. Verleysen, P.-J. De Temmerman, E. Van Doren, M. Abi, D. Francisco, and J. Mast, *Quantitative characterization of aggregated and agglomerated titanium dioxide nanomaterials by transmission electron microscopy*. Powder Technol. 258 (2014), pp. 180–188.
[15] A. Rao, M. Schoenenberger, E. Gnecco, T. Glatzel, E. Meyer, D. Brändlin, and L. Scandella, *Characterization of nanoparticles using atomic force microscopy*. J. Phys. Conf. Ser. 61 (2007), pp. 971.
[16] Z. Jia, J. Li, L. Gao, D. Yang, and A. Kanaev, *Dynamic light scattering: A powerful tool for in situ nanoparticle sizing*. Colloids Interfaces 2023, 7(1), 15.
[17] T. Kim, C.H. Lee, S.W. Joo, and K. Lee, *Kinetics of gold nanoparticle aggregation: experiments and modeling*. J Colloid Interf. Sci. 318 (2008), pp. 238–243.
[18] H.H. Liu, S. Surawanvijit, R. Rallo, G. Orkoulas, and Y. Cohen, *Analysis of nanoparticle agglomeration in aqueous suspensions via constant-number Monte Carlo simulation*. Environ. Sci. Technol. 45 (2011), pp. 9284–9292.
[19] J. Morán, J. Yon, and A. Poux, *Monte carlo aggregation code (MCAC) part 1: fundamentals*. J. Colloid Interf. Sci. 569 (2020), pp. 184–194.
[20] A. Gbaguidi, S. Namilae, and D. Kim, *Stochastic percolation network model for hybrid nanocomposites*, in *IEEE Aerospace Conference*, IEEE, 2020. pp. 1–13.
[21] A. Gbaguidi, S. Namilae, and D. Kim, *Stochastic percolation model for the effect of nanotube agglomeration on the conductivity and piezoresistivity of hybrid nanocomposites*. Comput. Mater. Sci. 166 (2019), pp. 9–19.
[22] S. Bhoi, S. R. Kolan, Andreas Bück, and E. Tsotsas, *Population balance modeling of formation and breakage of nanoparticle agglomerates in a spouted bed*. Powder Technol. 433 (2024): 119271.
[23] J. Liao, S. Qing, X. Zhang, X. Huang, and X. Wang, *Factors that influence the aggregation structure of nanoparticles in nanofluids: A molecular dynamics simulation*. J. Molec. Liquids 368 (2022), 120716.
[24] R. Wang, S. Qian, and Z. Zhang, *Investigation of the aggregation morphology of nanoparticle on the thermal conductivity of nanofluid by molecular dynamics simulations*. Int. J. Heat Mass Transf. 127 (2018), pp. 1138–1146.
[25] A.R. Alian and S.A. Meguid, *Molecular dynamics simulations of the effect of waviness and agglomeration of CNTs on interface strength of thermoset nanocomposites*. Phys. Chem. Chem. Phys. 19 (2017), pp. 4426–4434.

[26] A. Daw and J. Pender, *An ephemerally self-exciting point process*. Adv. Appl. Probab. 54 (2022), pp. 340–403.
[27] G.O. Mohler, M.B. Short, P.J. Brantingham, F.P. Schoenberg, and G.E. Tita, *Self-exciting point process modeling of crime*. J. Am. Stat. Assoc. 106 (2011), pp. 100–108.
[28] Q. Zhao, M.A. Erdogdu, H.Y. He, A. Rajaraman, and J. Leskovec. Seismic: A self-exciting point process model for predicting tweet popularity. In Proceedings of the 21th ACM SIGKDD international conference on knowledge discovery and data mining, 2015, pp. 1513–1522.
[29] S. Meyer, L. Fahrmeir, and M. Höhle. *Spatio-temporal infectious disease epidemiology based on point processes*. Doctoral dissertation, Institut für Statistik, 2009.
[30] S. Towers, A. Gomez-Lievano, M. Khan, A. Mubayi, and C. Castillo-Chavez, *Contagion in mass killings and school shootings*. *PLoS One* 10 (2015), pp. e0117259.
[31] E.W. Fox, M.B. Short, F.P. Schoenberg, K.D. Coronges, and A.L. Bertozzi, *Modeling e-mail networks and inferring leadership using self-exciting point processes*. J. Am. Stat. Assoc. 111 (2016), pp. 564–584.
[32] V. Filimonov and D. Sornette, *Apparent criticality and calibration issues in the Hawkes self-excited point process model: application to high-frequency financial data*. Quant Finance 15 (2015), pp. 1293–1314.
[33] J. Chandrapala and T. Leong, *Ultrasonic Processing for Dairy Applications: Recent Advances*. Springer, New York, 2015.
[34] A. Gbaguidi, S. Namilae, and D. Kim, *Monte Carlo model for piezoresistivity of hybrid nanocomposites*. J. Eng. Mater. Technol. 140 (2018.
[35] Y. Ogata, Space-time point-process models for earthquake occurrences, Ann. Inst. Stat. Math. 50 (1998), Pp. 379–402.
[36] A. Rohatgi. WebPlotDigitizer User Manual Version 4.6, 2022.
[37] Y. Zhang, Y. Chen, P. Westerhoff, K. Hristovski, and J.C. Crittenden, *Stability of commercial metal oxide nanoparticles in water*. Water Res. 42 (2008), pp. 2204–2212.
[38] Y. Zhang, Y. Chen, P. Westerhoff, and J. Crittenden, *Impact of natural organic matter and divalent cations on the stability of aqueous nanoparticles*. Water Res. 43 (2009), pp. 4249–4257.
[39] P.C. Ma, N.A. Siddiqui, G. Marom, and J.K. Kim, *Dispersion and functionalization of carbon nanotubes for polymer-based nanocomposites: A review*. Compos. A: Appl. Sci. Manuf. 41(10) (2010), pp. 1345–1367.
[40] X. Zhang, Q. Li, T.G. Holesinger, P.N. Arendt, J. Huang, P.D. Kirven, T.G. Clapp, R.F. DePaula, X. Liao, Y. Zhao, L. Zheng, D.E. Peterson, and Y. Zhu, *Ultrastrong, stiff, and lightweight carbon-nanotube fibers*. Adv. Mater. 19 (2007), pp. 4198–4201.
[41] C.S. Jarali, S.R. Basavaraddi, B. Kiefer, S.C. Pilli, and Y.C. Lu, *Modeling of the effective elastic properties of multifunctional carbon nanocomposites due to agglomeration of straight circular carbon nanotubes in a polymer matrix*. J. Appl. Mech. 81(2) (2014), pp. 021010.
[42] N. Prakash and G.D. Seidel, *Electromechanical peridynamics modeling of piezoresistive response of carbon nanotube nanocomposites*. Comput. Mater. Sci. 113 (2016), pp. 154–170.
[43] C.L. Dennis, A.J. Jackson, J.A. Borchers, P.J. Hoopes, R. Strawbridge, A.R. Foreman, J. van Lierop, C. Grüttner, and R. Ivkov, *Nearly complete regression of tumors via collective behavior of magnetic nanoparticles in hyperthermia*. Nanotechnology 20(39) (2009), pp. 395103.
[44] H. Liu and T.J. Webster, *Mechanical properties of dispersed ceramic nanoparticles in polymer composites for orthopedic applications*. Int. J. Nanomed. 5 (2010), pp. 299–313.
[45] A.W. Mello, A. Nicolas, and M.D. Sangid, *Fatigue strain mapping via digital image correlation for Ni-based superalloys: The role of thermal activation on cube slip*. Mater. Sci. Eng: A 695 (2017), pp. 332–341.

[46] A.W. Mello, T.A. Book, A. Nicolas, S.E. Otto, C.J. Gilpin, and M.D. Sangid, *Distortion correction protocol for digital image correlation after scanning electron microscopy: emphasis on long duration and ex-situ experiments*. Exp. Mech. 57 (2017), pp. 1395–1409.

[47] S.K. Brar, M. Verma, R.D. Tyagi, and R.Y. Surampalli, *Engineered nanoparticles in wastewater and wastewater sludge - evidence and impacts*. Waste Manage. 30(3) (2010), pp. 504–520.

[48] F. Maillard, S. Schreier, M. Hanzlik, E.R. Savinova, S. Weinkauf, and U. Stimming, *Influence of particle agglomeration on the catalytic activity of carbon-supported Pt nanoparticles in CO monolayer oxidation*. Phys. Chem. Chem. Phys. (2005), pp. 375–383.

[49] M. Pavlin and V.B. Bregar, *Stability of nanoparticle suspensions in different biologically relevant media*. Digest J. Nanomater. Biostruct. (2012), 7(4).

[50] M. Haghgoo, R. Ansari, and M.K. Hassanzadeh-Aghdam, *The effect of nanoparticle conglomeration on the overall conductivity of nanocomposites*, Int. J. Eng. Sci. (2020), 157, 103392.

[51] V. Kanniah, P. Wu, N. Mandzy, and E.A. Grulke, *Fractal analysis as a complimentary technique for characterizing nanoparticle size distributions*. Powder Technol. 226 (2012), pp. 189–198.

[52] H.H. Liu, J. Lanphere, S. Walker, and Y. Cohen, *Effect of hydration repulsion on nanoparticle agglomeration evaluated via a constant number monte-carlo simulation*. Nanotechnology 26(4) (2015), pp. 45708.

[53] T.H. Lim, D. McCarthy, S.C. Hendy, K.J. Stevens, S.A. Brown, and R.D. Tilley, *Real-Time TEM and kinetic monte carlo studies of the coalescence of decahedral gold nanoparticles*. ACS Nano 3 (2009), pp. 3809–3813.

[54] Y. Aït-Sahalia, J. Cacho-Diaz, and R.J.A. Laeven, *Modeling financial contagion using mutually exciting jump processes*. J. Financ. Econ. 117 (2015), pp. 585–606.

[55] T. Xu, F. Li, and C. Lu, *Visualization of materials using the confocal laser scanning microscopy technique*. Chem. Soc. Rev. 49(8) (2020), pp. 2408–2425.

[56] D. Aishee, S. Gare, S. Swain, P. Bhattacharya, V. Dhyani, L. Giri, and S. Neogi. *3D imaging and quantification of PLL coated fluorescent ZnO NP distribution and ROS accumulation using laser scanning confocal microscopy*. AIChE J. 68, no. 9 (2022): e17801.

[57] A. J. Koster, U. Ziese, A. J. Verkleij, A. H. Janssen, and K. P. De Jong. *Three-dimensional transmission electron microscopy: A novel imaging and characterization technique with nanometer scale resolution for materials science*. J. Phys. Chem. B 104, no. 40 (2000): 9368-9370.

Taylor & Francis
Taylor & Francis Group

Philosophical Magazine

ISSN: 1478-6435 (Print) 1478-6443 (Online) Journal homepage: www.tandfonline.com/journals/tphm20

The phase-field model in tumor growth

Rui D.M. Travasso, Mario Castro & Joana C.R.E. Oliveira

To cite this article: Rui D.M. Travasso, Mario Castro & Joana C.R.E. Oliveira (2011) The phase-field model in tumor growth, Philosophical Magazine, 91:1, 183-206, DOI: 10.1080/14786435.2010.501771

To link to this article: https://doi.org/10.1080/14786435.2010.501771

Philosophical Magazine
Vol. 91, No. 1, 1 January 2011, 183–206

Taylor & Francis
Taylor & Francis Group

The phase-field model in tumor growth

Rui D.M. Travasso[a]*, Mario Castro[b] and Joana C.R.E. Oliveira[c]

[a]*Centro de Física Computacional, Universidade de Coimbra, 3004-516 Coimbra, Portugal;* [b]*Grupo Interdisciplinar de Sistemas Complejos (GISC) and Grupo de Dinámica No Lineal, Universidad Pontificia Comillas, E-28015 Madrid, Spain;* [c]*CFP and Departmento de Enginharia Física, R. Dr. Roberto Frias, 4200-465 Porto, Portugal*

(*Received 11 January 2010; final version received 10 June 2010*)

Tumor growth is becoming a central problem in biophysics both from its social and medical interest and, more fundamentally, because it is a remarkable example of an emergent complex system. Focusing on the description of the spatial and dynamical features of tumor growth, in this paper we review recent tumor modeling approaches using a technique borrowed from materials science: the phase-field models. These models allow us, with a large degree of generality, to identify the paramount mechanisms causing the uncontrolled growth of tumor cells as well as to propose new guidelines for experimentation both in simulation and in the laboratory. We finish by discussing open directions of research in phase-field modeling of tumor growth to catalyze the interest of physicists and mathematicians in this emergent field.

Keywords: phase-field; tumor growth; angiogenesis; multiphase model; mixture theory; simulation

1. Introduction

Tumor growth is a central problem in biology and medicine and it is a highly complex system. Despite continuous efforts by the scientific community, both the genomic characterization of tumors [1,2] and the main physical mechanisms driving their development [3] are currently a matter of debate. These efforts are greatly enriched through an interdisciplinary approach. Physics, mathematics and computer simulation and modeling thus play a pivotal role in the research of tumor growth. The approach of mathematicians and physicists provides remarkable new ways of looking at biology. Starting the modeling from basic principles, the fundamentals of the problem can be tested and understood. On the other hand, and complementary to this method, biologists aim to find ways to hinder the development of tumors through a traditional bottom–top approach. Mutations are performed in genes regulating individual mechanisms which are inspected by observing the consequence of these mutations in the organism.

*Corresponding author. Email: rui@teor.fis.uc.pt

ISSN 1478–6435 print/ISSN 1478–6443 online

DOI: 10.1080/14786435.2010.501771
http://www.informaworld.com

Neoplastic cells have a high ability to adapt to different environments [2] and until now the blockage of a single mechanism of adaptation and growth has not been able, in general, to stop their proliferation. This feature of tumor cells provides endless challenges to the traditional biological approach as well as to the design of cytotoxic drugs to be delivered in chemotherapy. These drugs currently do not target processes exclusive to tumor cells, and since these cells can more easily adapt to the harsh environment created by these drugs than normal cells, chemotherapy may become very severe to the organism [4].

The different chemical factors and cell types which interact in a non-trivial fashion complicate the problem immensely. Adding to this complexity there are diverse stages of growth as well as diverse types of tumors, each having specific ways of responding to the same regulatory cues. In general, a tumor starts when a cell undergoes varied mutations in key genes regulating the mitosis cycle and the apoptosis process. This line of cells may proliferate avidly and/or avoid death in situations of high stress. It may generate a disorganized group of densely packed cells giving rise to an avascular tumor.

Solid tumors in their early stages of development have the property of not growing past a certain size due to the death of their cells at the core by lack of nutrients. In simple terms, the acquisition of nutrients at the boundary is not able to meet the needs of the inner cells. This, in addition to the problem of confinement of the inner cells (the fast growth does not allow them to migrate), produces the so-called core necrosis inside the tumor.

When this stationary non-threatening stage is reached, malignant tumors adapt to the environment and undergo an active search for the nutrients they need to survive and proliferate. This can be achieved in two ways: (i) by migrating towards existing capillaries (through a process called co-option, characteristic of infiltrative tumors typically in densely irrigated organs like the brain, lung, liver or kidney [5,6]), or (ii) releasing factors, such the Vascular Endothelial Growth Factor (VEGF), which drive the nearby vessel's endothelial cells to create new branches in the direction of the tumor, providing it with nutrients [7]. In this last case, we have a vascular tumor which can metastasize to new regions of the body in the case when a cell is able to enter the blood circulation.

The insights coming from modeling and computer simulation help the understanding of the implications of common or unifying mechanisms in solid tumor growth, such as those described above. A prevalent feature in solid tumor growth is the existence of a boundary that separates the various constituents in the system. These organize themselves in different phases, and so the problem may be tackled by understanding and simulating the dynamics of the tumor/normal cells interface, falling into the moving boundary problem category. This reasoning may provide relevant insights into controlling the development of tumors in the future.

Phase-field models, originally developed by the physics community in the context of non-equilibrium systems, have achieved great success over the past decades in describing a whole range of materials science phenomena related to nucleation and growth. The phase-field permits an elegant and multifaceted numerical description of complex nonlinear problems with moving boundaries. It is a tailorable method that can be easily adapted to quantitatively describe an extremely vast range of

mechanical and dynamical properties of interfaces as a function of bulk properties [8]. In materials science, the various phase-field applications developed so far have matured sufficiently to allow their use in realistic applications with a high degree of accuracy.

Nevertheless, the application of the phase-field model to problems related to tumor dynamics is very much in its early stages of development. In this review, we describe the as-yet few applications in the literature of the phase-field model. We stress the benefits this new type of approach will bring to the better understanding of cancer dynamics with the aim of attracting scientists from different disciplines to this challenging problem.

Recent progress in imaging techniques allows oncologists to accurately track the evolution of tumors. With this in mind, it is paramount to develop means of following and predicting the development of a tumor in space and time. In this context, and with the insights learnt from materials science, the phase-field model has recently been used both to understand individual processes, as well as to attempt the simulation of a whole tumor in the avascular and vascular phases.

In Section 2, we review approaches that use phase-field to understand basic processes in tumor growth; in Section 2.1, the study of the relevance of different mechanisms controlling the movement of tumor cells in the avascular state is described, while in Section 2.2, we review a phase-field model for angiogenesis. In Section 3, we review approaches which use the phase-field model and constitutive relations for the stress tensor to study the dynamics of tumor growth. In Section 4, we discuss ways to systematize and improve the current phase-field modeling of tumors. Finally, in Section 5, we conclude by considering the benefits and limitations of this method in modeling tumor growth.

2. Simple phase-field approaches

As stated in the Introduction, tumors are highly complex systems and, from the beginning, simple models have been constructed to address one or two particular mechanisms of tumor growth, such as chemotaxis, cell adhesion, cell proliferation and death, or cell heterogeneity. These models probe the relevance of each process individually. Different techniques are suitable for modeling different mechanisms. The phase-field model, taking into account intrinsic cell adhesion, has been used to test the relevance of different competing mechanisms of chemotaxis in the situation of tumor growth [9].

Models for tumor angiogenesis, on the other hand, are more complex, include diverse scales in the system and simulate the growing ramified capillary network that nourishes the vascular tumor [10].

2.1. *The role of competing mechanisms in tumor growth*

One of the main difficulties when modeling tumor growth is the variety of ingredients that contribute to growth in similar ways. For instance, experiments have shown that a variety of tumor cells produce both protein growth factors and their corresponding receptors, enabling *autocrine* or *paracrine* signaling if, respectively, the stimulus not

only affects the *source* but also its bystander cells [11]. Such polypeptide growth factors can, for example, stimulate tumor cell growth and invasion, such as in the case of hepatocyte growth factors [12] and epidermal growth factors [13], or induce tumor angiogenesis (through secretion of VEGF [14,15]).

In those cases, when biological experiments only provide a qualitative understanding of such mechanisms, modeling becomes more valuable. Thus, from discrete to continuum modeling, much work has been devoted to understanding the specific role of those mechanisms, from a microscopic (see [16] and references therein) to a macroscopic point of view (see, for instance the review papers [17,18]).

Macroscopic modeling has been traditionally approached through reaction-diffusion equations. This allows us to account for cell migration in a simple way (through diffusion terms), and additionally to include cell signaling or cell–cell interactions through mass action laws (e.g. through a Michaelis–Menten mechanism). However, in order to exploit these methods to extract morphological features of the tumor, several restrictions and approximations usually appear (such as considering the tumor as a sphere, or one-dimensional versions of the models).

Notably, one can use some tools borrowed from the phase-field community to reinterpret reaction-diffusion theories as phase-field models. In [9], this approach was used to explain experiments of brain tumor spheroids grown *in vitro*. In this section, we review this work and some of the ideas that can be projected in future work in the field. Moreover, we anticipate that one of most interesting results is the large degree of universality of the results for different functional mathematical forms of the *reaction* terms (actually, this is one of the traditional benefits of the phase-field approach).

2.1.1. *Modeling* in vitro *tumor growth*

Current monitoring techniques have helped to visualize growing tumors (both *in vitro* and *in vivo*). However, simple inspection of the emerging morphology of the tumor does not always allow us to determine which are the main physical mechanisms controlling the tumor growth. For instance, whether it is compact or produces branches may be due to competing or, on the contrary, cooperative mechanisms.

In [9], the authors were precisely interested in how the mechanisms of hetero and homotype chemotaxis (induced, respectively, by both an external agent or by the very tumor cells) compete and/or cooperate in the formation of tumor branching structures, and how the reaction terms must be chosen in order to reproduce mathematically, with some degree of universality, the experimentally observed patterns.

The experimental setting consisted of a multicellular tumor spheroid (MTS) embedded in a tissue culture medium-enriched extracellular matrix (ECM) gel, matrigel [19]. Tumor expansion is a multistep process that involves several mechanisms of progression, mainly: tumor cell proliferation and invasion guided by chemotaxis. In Table 1, all of the involved fields are summarized.

The model tries to capture the underlying relationships between the different components of the system that are coupled in a non-trivial way. Biologically, the matrigel (which plays the role of both an extracellular matrix and a source of

Table 1. Mathematical description of *in vitro* brain tumor growth.

Symbol	Description
$M(\mathbf{x}, t)$	Density of the underlying matrigel
$Q(\mathbf{x}, t)$	Heterotype chemo-attractant (externally supplied)
$C(\mathbf{x}, t)$	Homotype chemo-attractant (produced by the tumor cells)
$U(\mathbf{x}, t)$	Density of tumor cells.[a]

Note: [a]This density plays the role of the *phase-field* of the model. Thus, the tumor boundary is the *diffuse* region where the tumor cell density goes from its mean value to almost zero.

nutrients) helps the *in vitro* tumor cells to proliferate but also limits their mobility. The tumor cells are attracted chemotactically by the heterotype chemo-attractant but also segregate their own homotype chemo-attractant. Finally, both chemo-attractants diffuse in the matrigel.

To put this on a mathematical footing, these biological relationships are described in simple terms (further details can be found in [9]):

- $M = M(\mathbf{x}, t)$ is the average density field of the gel matrix as a function of space $\mathbf{x}$ and time t. The role of M is two-fold. From a nutrient perspective, the tumor cells (whose concentration will be described by the density field $U(\mathbf{x}, t)$ hereafter) metabolize M and hence they are able to proliferate. Besides, from a mechanical perspective, the solid gel matrix has an impact on tumor cell mobility, i.e. it confines the tumor cells and so they are guided by *least or lesser resistance* areas throughout the ECM here *in vitro*, or *in vivo*, by the distinct mechanical properties of the surrounding tissue.
- Chemotaxis can be generally defined as motility induced and guided by a concentration gradient. Wells [20] reviews the main experimental results on tumor chemotaxis and the biological mechanisms that produce it. The heterotype chemo-attractant represents nutrients diffusing from a source, e.g. a blood vessel *in vivo*, and as such is what guides both on-site cell proliferation and the onset of invasion. Acknowledging that the original experimental setting [19] used a non-replenished nutrient source, in the model of [9] the heterotype chemo-attractant was supplied externally.
- Tumor cells have been shown to produce protein growth factors such as the transforming growth factor alpha (TGF-α). These growth factors can affect the tumor producing cell itself, hence generating an *autocrine* feedback loop, as well as bystander cells, an effect called *paracrine* [21]. Thus, C stand for the density field of the homotype chemo-attractants.

Mathematically, these involved interactions can be summarized in the following set of equations:

$$\partial_t M = \mu_M \nabla^2 M - \lambda_M R_M(M, U), \tag{1}$$

$$\partial_t Q = \nabla(\mu_Q(M)\nabla Q) - a_Q R_Q(Q, U), \tag{2}$$

$$\partial_t C = \nabla(\mu_C(M)\nabla C) + \alpha_C R_C^{(p)}(M, U) - a_C R_C^{(d)}(C, U), \tag{3}$$

$$\partial_t U = \nabla(\mu_U(K - \lambda_M/\lambda_U U)\nabla U) + \lambda_U R_M(K - \lambda_M/\lambda_U U, U), \tag{4}$$

where K is constant and the R functions are reaction terms. In particular, R_M may be understood as a *double-well potential* in phase-field terminology. This function forces the field U to take values close to the minima of the potential. In the case of the *double-well* potential, there are two equiprobable minima. With the interaction with external agents (for instance, chemo-attractants) one minimum becomes more favorable than the other. This asymmetry triggers the motion of the tumor surface.

2.1.2. *Results*

To the phase-field equation (4) may be added an interesting term not commonly present in condensed matter systems. This term has the form:

$$-\nabla(U\chi(Q)\nabla Q). \tag{5}$$

This term accounts for hetero-chemotaxis (through the coupling with the field Q). The details of the function $\chi(Q)$ are not as important as the explicit dependence on the gradient of Q.

Using the standard matching asymptotic procedure and matching the inner and outer expansions yields the normal velocity of the tumor in the original dimensions [8], and it can be found that (see [9] for details):

$$v_n = -\mu\kappa + \nu\nabla Q \cdot \mathbf{n}, \tag{6}$$

where κ is the mean curvature of the level surfaces of constant normal coordinate, $\mathbf{n}$ is a unit vector normal to the tumor interface and directed away from the tumor and ν and μ are coefficients related to the reaction terms in Equations (1)–(4). This simple equation has important consequences for the comprehension of tumor growth:

- In the absence of chemotaxis and proliferation, for an initially circular tumor of radius R_0, Equation (6) reduces to $dR/dt = -\mu/R$, so tumor growth rate decreases with time (as $\sim t^{-1/2}$) leading to a non-invasive growth which can remain benign for long periods of time.
- When chemotaxis is present (for a general tumor front geometry) Equation (6) provides a critical curvature (reminiscent of the classical Greenspan model [22]) $\kappa_c = (\nu/\mu)\nabla Q \cdot \mathbf{n}$, such that for $\kappa < \kappa_c$ the tumor interface locally has a positive velocity, for $\kappa > \kappa_c$ the tumor interface locally has a negative velocity and for $\kappa = \kappa_c$ the tumor interface locally has vanishing velocity. Note that this is precisely the reason for the dynamical instability that guarantees the development of invasive branches. Tumor invasion will take place on the tumor surface wherever the local curvature is below the critical value κ_c. This result agrees with the specific case considered in [23]. Invasive tumor growth is a consequence of this critical curvature (see Figure 1).

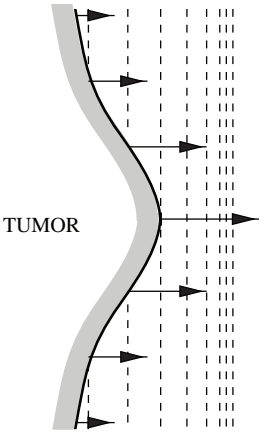

Figure 1. Sketch of the heterotype chemo-attractant effect on tumor cell invasive drift. Dashed lines represent level sets of Q and arrows represent the local normal velocity of the tumor cells due to chemotaxis (the length of the arrows is proportional to the normal velocity) [9].

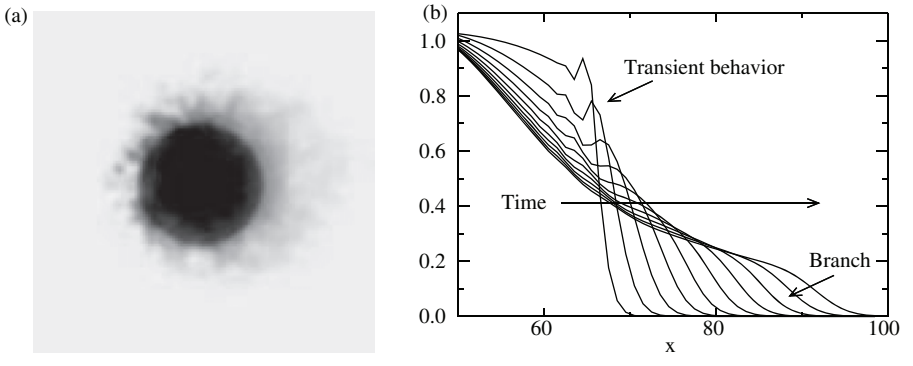

Figure 2. (a) Numerical simulation of tumor branching induced by a heterotype chemotactic source located at $x = L_x$. The plot represents the tumor density field $U(x, y, t)$. (b) Cross-section of the tumor in panel (a) for different times [9].

- The inclusion of homotype chemotaxis is straightforward (the only sophistication is the existence of two *outer* equations). In [9], it was shown that homochemotaxis enhances the growth rate of the invading branches but cannot, by itself, generate it.

Thus, the sharp-interface limit explains the role of proliferation (decaying growth rate) and chemotaxis (branching instability). Additional benefits of the phase-field approach lay on the fact that the full equations allow us to obtain the evolution of the morphology. In Figure 2, some branching morphologies are shown: (a) top view and (b) cross-section. The comparison between the *in silico* and *in vitro* tumors is suggestive (see [24] and [16]).

2.1.3. *Conclusion*

In summary, in this section we have emphasized that the phase-field approach allows us to write down relatively simple models which provide straightforward analytic predictions combining well established reaction-diffusion models in the light of phase-field techniques. In addition, it proves to be very useful for interdisciplinary cancer research as it provides the following, at least in part experimentally testable hypotheses:

(i) tumor cell proliferation by itself cannot generate the invasive branching behavior observed experimentally, yet, proliferation is a requirement for invasion;
(ii) heterotype chemotaxis provides an instability mechanism that leads to the onset of tumor cell invasion; and
(iii) homotype chemotaxis does not provide such a mechanism but enhances the mean speed of the tumor surface.

As we will show in Section 4.1, the identification between reaction-diffusion and phase-field can be performed systematically in order to include mechanical stress, necrosis and, in general, internal forces between the cells (beyond the pure *excluded volume* interaction of the reaction-diffusion formulation).

2.2. *Phase-field and angiogenesis*

Tumor simulation is currently able to quantitatively reproduce features of vascular tumor growth in systems *in vivo* [25]. It may be envisaged in the future as a reliable companion of experimental and clinical work, helping to clarify the processes and mechanisms in this type of system. As in tumor simulation, the intrinsic multiscale nature of tumor angiogenesis, led different research groups to address the topic from either the macroscopic or the microscopic perspective.

The first simulations were done 20 years ago using diffusion equations, and many others followed the same strategy (reviewed in [26]). These models describe the system macroscopically through average endothelial cell densities. Some of these works are able to delimitate a capillary by considering the points where the concentration of endothelial cells is higher, but do not show evidence of branching and do not predict the resulting capillary network.

In the context of continuous models, the possibility of pattern formation through mechanical interaction between endothelial cells and the extra-cellular matrix has been considered in the literature [27–30]. The main focus of these works was on the cell motion in hard substrates *in vitro*. These models consider a strain dependent diffusion constant for the endothelial cells which are also advected by a velocity field. This field is obtained through balancing the cell generated traction (written through a constitutive relation as a function of the local endothelial cell density) together with the viscoelastic extra-cellular matrix restoring forces and the anchoring forces to the Petri dish. The authors are able to qualitatively reproduce the patterns observed in these experiments, and to obtain the experimentally observed range of endothelial cell densities [30].

From the beginning of the 1990s microscopic cell based models have been used to model processes in the context of angiogenesis [31–38]. The large number of different cells in the tissue and the many processes in which they participate are a major stumbling block to cell based models. Some of these models incorporate an extremely large number of rules and parameters, while being hard to control, because of their high sensitivity to small modifications. This is of importance, since many of the required parameters are a true challenge to measure and have to be postulated.

Because it gives rise to a hierarchical network of capillaries, modeling angiogenesis is intrinsically different from modeling tumor growth. At the tip of each growing capillary there is a differentiated (or activated [40]) cell. This cell opens a pathway in the existing media responding to the environment differently from the other capillary cells. Hence, the natural modeling framework is a hybrid model [41] with particular rules for the tip cells and continuous/phase-field dynamics for the rest of the system. This model will reproduce the thickness of the vessels in an earlier stage of angiogenesis, before the blood has a chance to remodel the vessel network. It will correctly describe systems where the growth and receding of vessels is fast, such as in inflammation or early vascularization in tumor growth.

2.2.1. *Model*

A phase-field description of the stalk cells has been undertaken by Travasso et al. [10]. This model treats, in a controlled manner, the different scales of the problem, incorporating the correct physiological branching mechanism. Recently it was proved that endothelial cell activation, which is responsible for the sprouting of new branches, is controlled by the Notch signaling pathway [42]. This mechanism, until now, has rarely been considered in angiogenesis modeling [38,39]. The Notch is a intracellular pathway which takes as input the activation of a membrane protein specifically by proteins attached to the membrane of a neighboring cell. It allows the communication between neighboring cells in diverse processes of life and it is pivotal during both embryogenesis and angiogenesis. In angiogenesis, this communication forbids the neighbor from an activated cell to be sensitive to VEGF, not being able to become activated.

Proliferative and non-activated cells are described by the phase-field part of the model. An order parameter ϕ is introduced which is equal to -1 outside the capillary and $+1$ inside it. Values of ϕ larger than one correspond to areas of high proliferation of endothelial cells which will lead to the widening of the capillary.

In this model, the authors started with the Cahn–Hilliard description of the ϕ dynamics as a function of the VEGF concentration T:

$$\partial_t \phi = \nabla^2\left[-\phi + \phi^3 - \epsilon\nabla^2\phi\right] + \alpha_p(T)\phi\Theta(\phi). \tag{7}$$

The proliferation rate is given by $\alpha_p(T)$ and $\Theta(\phi)$ is the Heaviside function.

The VEGF is produced at the tissue cells and obeys a diffusion equation with a consumption term:

$$\partial_t T = \nabla\cdot(D(\mathbf{r}, T)\nabla T) - \alpha_c T\phi\Theta(\phi)\ , \tag{8}$$

where α_c is the consumption rate.

The migration and activation of endothelial cells correspond to phenomena at the cell scale, and are implemented in the model through the cell based component. Endothelial cell activation in the model occurs at points where T, ∇T and ϕ are above specific cut-off values if two distance requirements are satisfied. Firstly, the center of the new cell must be located further than a cell radius length from the surface of the capillary, and secondly it must also be located at least two diameters away from any other activated cell center (because Notch signaling forbids the activation of neighboring cells). At most one cell is activated per integration time step.

The equation describing the activated cell velocity $\mathbf{v}$, qualitatively with the same form used in Equation (6), is given by

$$\mathbf{v} = \chi(T, \nabla T)\nabla T, \tag{9}$$

where $\chi(T, \nabla T)$ is the chemotactic response of the endothelial cells.

As in the biological system, when the signal is removed, the endothelial cell returns to a non-activated state: an activated cell will be removed from the system when the concentration and gradient of VEGF both fall below the activation value.

To merge the tip cell dynamics with the phase-field description, the value of the order parameter inside the tip cell is related to the proliferation rate $\alpha_p(T)$ and the chemotactic response of the cells χ (through $|\mathbf{v}|$):

$$\phi_{\text{tip}} = \frac{\alpha_p(T)\pi R_c}{2|\mathbf{v}|}, \tag{10}$$

where R_c is the cell radius. This expression is obtained by calculating excess cell density by proliferation occurring as the tip cell moves chemotactically in the tissue. Per unit time, the material produced in the region of the activated cell is $\alpha_p(T)\pi R_c^2$, and the area the cell sweeps per unit time is $2R_c|\mathbf{v}|$. Dividing the material amount by the area, ϕ_{tip} is obtained. If the value of ϕ_{tip} is smaller than 1, then the capillary formed will become thinner than $2R_c$ unless proliferating cells fill it in, while if ϕ_{tip} is larger than 1, the resulting capillaries will become thicker than $2R_c$. Hence, this value of ϕ_{tip} does not describe the density of cells at the tip cell, a meaningless concept *per se*, but the density of stalk cells on the trail of the tip cell.

2.2.2. *Results and conclusions*

This simple model captures varied features of the angiogenesis dynamics, produces ramified networks (see Figure 3), achieves important qualitative conclusions and predicts and explains experimental observations.

Chemotaxis and proliferation rates are shown to be two extremely important parameters for the tailoring of the capillary network. They function as tuning knobs for the number of ramification points and vessel thickness in the network. In fact, decreasing the proliferation leads to thinner and less ramified vessels, while decreasing the chemotactic coefficient leads to thicker and less ramified vessels (Figure 3). The tissues may use these two parameters, controlled by the tissue properties and the environment signals, to specify networks with different properties in different parts of the organism.

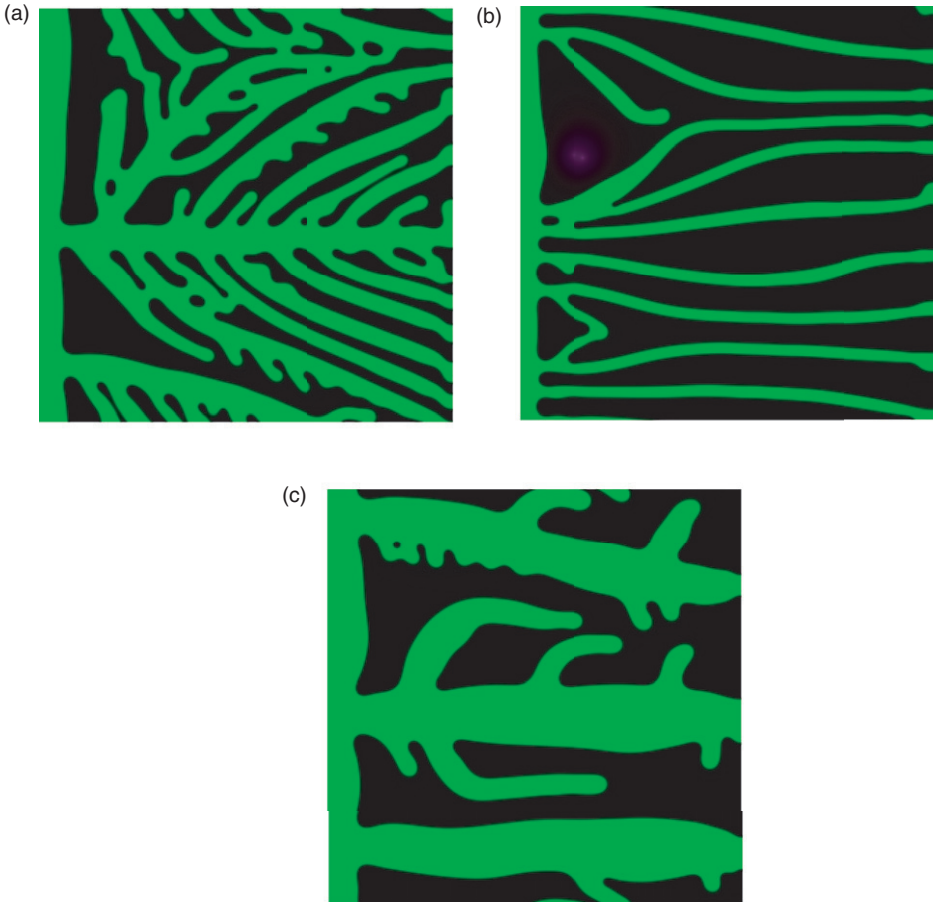

Figure 3. Numerical simulation of angiogenesis with the phase-field model described in [10]. (a) Resulting capillary network growing above a tissue in hypoxia. (b) Capillary network for reduced endothelial cell proliferation (α_p reduced to one third). Capillaries are thin and less ramified. (c) Capillary network for reduced endothelial cell chemotaxis response – χ is 40% of the corresponding value in (a). Capillaries are thick and less ramified.

Hence, the reason for the precise control by the organism of the angiogenesis process *in vivo* is evident, for example in situations of embryogenesis. This work demonstrates how angiogenesis is extremely sensitive to a variation of simply two or three-fold in either the endothelial cell proliferation rate or chemotactic coefficient, resulting in completely different capillary networks. This is also verified *in vivo* where an embryo is not able to form a functioning vasculature if one of the allele has a deletion in the VEGF gene.

The model also agrees qualitatively with experimental results, where metallo-proteinases production by the tissue cells was varied [43,44]. This protein controls indirectly the diffusion behaviors for different types of VEGF molecules. When this mechanism was introduced in the model, it was verified thickening and merging of

the vessels as the amount of metalloproteinases was increased in the system. This effect was only observed in the regime where the tip cell velocity does not depend on the magnitude of the VEGF gradient, i.e. the cells are moving at the maximum velocity allowed by the tissue. Hence the model predicts that what is limiting the velocity of the tip cell in the experimental setup of [44] is the tissue and not the gradient of VEGF, which has the primary function of directing the tip cell.

It is remarkable that a simple phase-field model can provide these insights into the process of angiogenesis. The pathway for the improvement of the model is readily seen by introducing elastic properties that can be measured in the system and can be implemented within the phase-field framework. More challenging will be to write a phase-field description for the tip of the capillary allowing analytical study of the system.

3. Phase-field and the multiphase tumor modeling

During the 1990s each research group created its own simple model for tumor growth focused on a special feature of the process. In this century, the models became more complete and the interaction between different groups led to models including a whole panoply of mechanisms in tumor growth. These models can be easily adapted to simulate particular types of tumors, but have the drawback of being very hard to explore because of the large number of parameters [25,45]. Multiphase models belong to this type of complex model. The governing equations for the tumor environment are based on mixture theory and are the result of reaction-diffusion equations coupled with constitutive equations describing the relation between the flow velocity and stress tensor [46–50]. Some of these models [51,52] describe vascular tumors and include the model for angiogenesis dynamics described in [36].

Recently, Frieboes et al. and Cristini et al. [52,53] obtained a phase-field version of their multiphase model for avascular tumor growth [54]. Cristini et al. showed that this approach can get rid of thermodynamic inconsistencies of the multiphase description while both models still share the same form in the linear regime [53]. This work is a major step forward since it opens this area of research to the phase-field community.

3.1. *The model*

We follow here the derivation of the model in [53]. The authors start by writing a conservation equation for each of the N phase's volume fractions ϕ_k, with $k = 0, \ldots, N-1$, corresponding to the different cell types, with $k = 0$ corresponding to the liquid phase:

$$\partial_t \phi_k + \nabla \cdot (\phi_k \mathbf{v}_k) = \frac{1}{\rho_k}(\Gamma_k - \nabla \cdot \mathbf{j_k}), \tag{11}$$

where ρ_k is the density of each phase. In this equation, $\mathbf{j}_k$ and $\mathbf{v}_k$ are the flux and velocity of each component corresponding, respectively, to the processes of diffusion

and advection. The factor Γ_k represents the rate of increase or decrease of a component k due to biological processes (proliferation or death).

The different component fluxes are given by (for $k \neq 0$)

$$\mathbf{j}_k = -\sum_{i=0}^{N-1} M_{ik} \nabla \mu_{ik} / \rho_k. \tag{12}$$

By conservation of mass,

$$\mathbf{j}_0 = -\sum_{k=0}^{N-1} \mathbf{j}_k. \tag{13}$$

M_{ik} gives the mobility of phase i in phase k and μ_{ik} is the chemical potential given as a function of the system's free energy. The existence of the free energy based description is the main difference between this approach and the other mixture models previously mentioned. Later the considered free energy density F will be of the Ginzburg–Landau type, but, in general, F will be a function of the various ϕ_k and $\nabla\phi_k$ for each component. The Ginzburg–Landau functional has two ingredients: a potential (for example, a double-well potential, whose role was stressed above) and an interfacial term. This term is an energy penalty related to the existence of interfaces between the different phases of the system. This is an effective way to model the preference for a tumor cell to be attached to other tumor cells. In fact, a solid tumor is compact and resistant to deformations (in opposition to a micelle or a membrane). The potential is used to constrain the field (outside the interfaces) to the potential's minima, corresponding to the various phases of the system.

The chemical potential can be defined as

$$\mu_{ik} = \frac{\partial F_i}{\partial \phi_k} - p(\rho_i - \rho_0)\delta_{ik} - \nabla \cdot \frac{\partial F_i}{\partial \nabla \phi_k}, \tag{14}$$

where p is the pressure.

For Γ_k different descriptions for the biology can be taken. One of the simplest is to consider that the tumor phase, corresponding to $k = 1$ for example, increases at rate λ_p with the concentration of nutrient n, and the tumor cells convert into the liquid phase by apoptosis at rate λ_a:

$$\Gamma_1 = \lambda_p n \rho_1 \phi_1 - \lambda_a \rho_1 \phi_1. \tag{15}$$

If we are dealing with a two phase model constituted by tumor and interstitial liquid, then $\Gamma_0 = -\Gamma_1$. In general $\sum_k \Gamma_k = 0$. Equation (15) represents a simple example of how these terms can be written into the model. Their form depends on the phenomena required to model and on its level of complexity.

The applications of this model discussed in [53] consider the tumor as a porous medium with the dynamics dominated by the advection term. This regime is valid for large enough phase domains [55], and so the coefficients M_{ik} in Equation (12) are set identically equal to zero.

The velocity field obeys the following incompressibility condition:

$$\sum_{k=0}^{N-1} \nabla \cdot (\phi_k \mathbf{v}_k) = \sum_{k=0}^{N-1} \frac{\Gamma_k}{\rho_k} \quad \Longleftrightarrow \quad \nabla \cdot \left(\sum_{k=0}^{N-1} \phi_k \mathbf{v}_k \right) = 0 \ , \text{ if } \rho_k = \rho = \text{const.} \tag{16}$$

The authors follow [50,54] to write a constitutive equation relating the free energy and the velocity field to the stress tensor. There is extensive practice in writing constitutive relations of this type in the mixture model formulation which serves the basis for this phase-field model. In particular, the considered general constitutive relation for the stress tensor is

$$\sigma_k = \left(F_k - \phi_k \sum_{i=0}^{N-1} \mu_{ik} - \rho_k \phi_k p \right) I - \sum_{i=0}^{N-1} \nabla\phi_i \otimes \frac{\partial F_k}{\partial \nabla \phi_i} + \mathcal{L}_k \left(\nabla \mathbf{v}_k + \nabla \mathbf{v}_k^T \right), \tag{17}$$

where $\mathcal{L}$ is a positive definite symmetric tensor related to the local viscosity of the medium and is able to include the anisotropy given by the fiber directions.

There is also a constitutive relation for the density of forces between the different components of the mixture π_k:

$$\pi_k = p\rho_0 \nabla\phi_k + \sum_{i=0}^{N-1} (\mu_{ik} \nabla\phi_k - \mu_{ki} \nabla\phi_i) - \alpha_k (\mathbf{v}_k - \mathbf{v}_0) \ . \tag{18}$$

The symmetric positive definite matrix α_k describes the forces acting on component k for moving with respect to the fluid phase with relative velocity $\mathbf{v}_k - \mathbf{v}_0$. Let us consider the absence of external body forces. Hence

$$\nabla \cdot \sigma_k = -\pi_k \ . \tag{19}$$

This equation relates the two constitutive equations, (17) and (18), enabling the writing of the velocity field as a function of the free energy density and the composition of the mixture. The incompressibility relation (16) allows us to solve the pressure.

From Equation (19), considering linear momentum conservation, one obtains the force matrix on the fluid phase: $\pi_0 = -\sum_k \pi_k$. The slow motion of the fluid through the porous media constituted by the tissue cells is driven by the pressure gradient, and the viscosity does not play an important role [50]. Hence, considering $\mathcal{L}_0 = 0$, Equation (19) becomes the Darcy law:

$$\phi_0 \nabla \left(\rho_0 p + \sum_{i=0}^{N-1} \mu_{i0} \right) = \phi_0 \nabla p' = \sum_{k=0}^{N-1} \alpha_k (\mathbf{v}_k - \mathbf{v}_0) \ . \tag{20}$$

Cell–cell adhesion can be implemented by a Ginzburg–Landau free energy density where the interface between the different phases is the result of a term proportional to the square of the order parameter gradient modulus:

$$F_k = f_k(\phi_0, \ldots, \phi_{N-1}) + \phi_k \sum_{l=0}^{L} \chi_{kl} c_l + \sum_{i=0}^{N-1} \frac{\epsilon_{ki}}{2} |\nabla \phi_k|^2 \ , \tag{21}$$

where c_l are the various chemical factors controlling the dynamics of the cells and χ_{kl} are the corresponding chemotactic coefficients. The responses to these agents are included directly in the energy of the system and will drive the order parameter in the

dynamical Cahn–Hilliard equation (11) through the advection term. Finally, from (19), the velocity of each component obeys

$$\alpha_k(\mathbf{v}_k - \mathbf{v}_0) = -\frac{\rho_k}{\rho + 0}\phi_k \nabla(p' + \mu_k') + \nabla \cdot \left(\mathcal{L}_k\left(\nabla \mathbf{v}_k + \nabla \mathbf{v}_k^T\right)\right) , \tag{22}$$

with

$$\mu_k' = \sum_{i=0}^{N-1}\left(\frac{\rho_0}{\rho_k}\mu_{ik} - \mu_{i0}\right) .$$

3.2. *Results and conclusions*

We have carefully formed here the most general equations for the phase-field description of the mixture model developed in [53]. Equations (20) and (22) together with Equation (16) allow for the calculus of the velocity field as a function of the composition of the mixture. Then this velocity is included in the Cahn–Hilliard equation (11) to obtain the evolution of the different concentration fields.

In [53], the authors proceed to apply the complete model to a simpler system: a two component phase-field model (liquid plus tumor). After defining this model they compare it with other existing models in the literature, verifying that it can be regarded as a simpler phase-field description of the model in [50], and in the sharp interface limit it reproduces existing single phase models in the literature.

The non-dimensional version of the simplified phase-field equations is similar to those derived in Section 4.1.1:

$$\frac{\partial \phi}{\partial t} = \nabla \cdot \left(\frac{\phi^2}{\epsilon}\nabla \mu\right) + \mathcal{P} n \phi - \mathcal{A}\phi , \tag{23}$$

$$\mu = \mathcal{G}^{-1}(f'(\phi) - \epsilon^2 \nabla^2 \phi) - \epsilon \chi n , \tag{24}$$

$$\nabla \cdot (D(\phi)\nabla n) - n\phi = 0 . \tag{25}$$

In these equations, the variables $\mathcal{P}, \mathcal{A}, \mathcal{G}, \chi, \varepsilon$ and D are non-dimensional combinations of the original variables. The third equation represents the fast diffusion of the nutrient throughout the tissue with respect to the slower tumor growth. The last term of the second equation represents the tumor chemotaxis driven by the nutrient.

The simulation of a 2D system using a multilevel multigrid scheme [61] yields surprising results. In an avascular situation and with no replenished nutrient, the authors verify the evolution of a tumor from a circular shape into a ramified structure (see Figure 4). This nonlinear model displays a shape instability which leads to the formation of a finger-like structure similar to structures observed *in vivo* in hypoxia induced invasive growth [62]. In fact, hypoxia may drive the formation

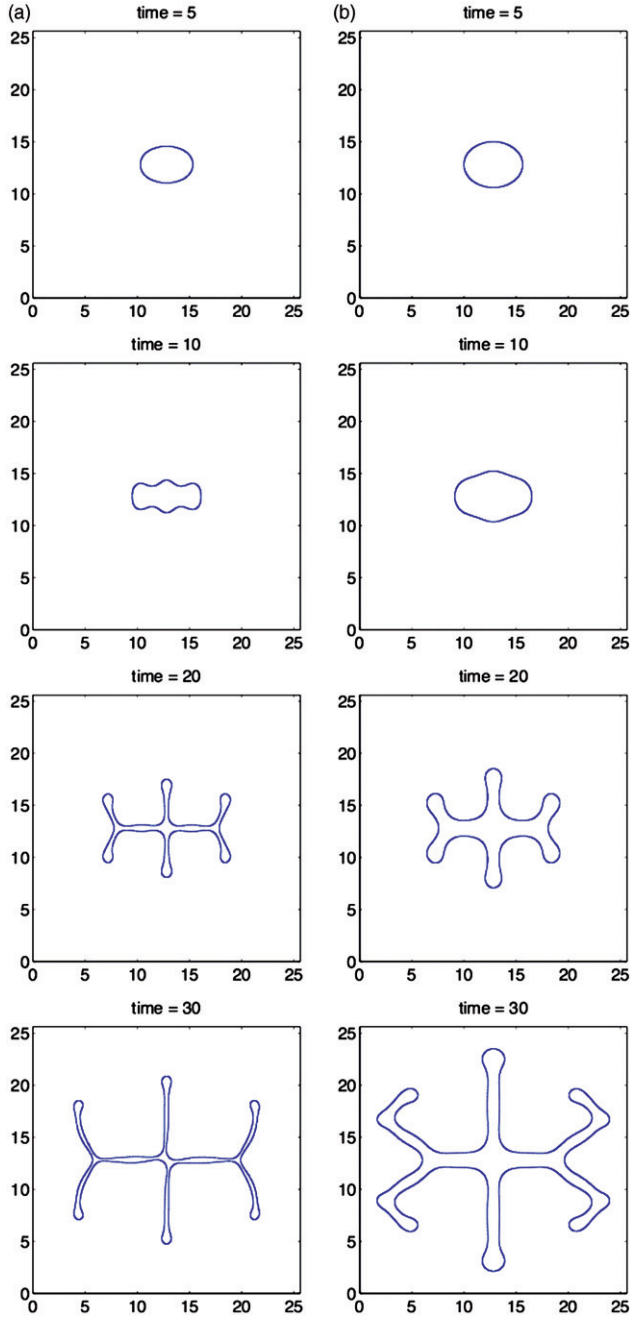

Figure 4. Evolution of the tumor surface according to the two component version of the model presented in [53]. An initial, almost circular tumor develops branches that become much thinner with time. In (a) the proliferation rate (in Γ_1) is one-fifth of the proliferation in (b) [53]. With kind permission from Springer Science + Business Media, Journal of Mathematical Biology, *Nonlinear simulation of solid tumor growth using a mixture model: invasion and branching*, Vol. 58, 2009, p. 723, V. Cristini, X. Li, J.S. Lowengrub and S.M. Wise.

of these structures in spherical tumor aggregates when the tumor cells are able to move chemotactically in oxygen deprived conditions.

In the simulation, the ramified structures always evolve in time until the model becomes invalid due to the formation of very thin domains. The instabilities are shown to be more dramatic at low proliferation rates while the fingers become thicker with the increase of the proliferation rate. Nutrient chemotaxis has been shown to be an important driver for the instability, though it is not a requirement, i.e. the fingering occurs at $\chi = 0$. This model does not present a cut-off curvature for branching as is the case of the model presented in Section 2.1.1 which simulated tumor dynamics in the matrigel, a much stiffer medium, than is the case here.

In [52], this model is applied to a vascular glioma, by including an angiogenesis model developed by Plank and Sleeman [14,15]. Tumor growth is simulated in a truly realistic environment consisting of various tissues: white matter, gray matter and bone. The model is able to produce quantitative predictions for the size and evolution of the tumor in time.

4. General picture, future research directions

Until now we have shown the current applications of phase-field models in tumor growth and related processes. We now need to find ways to improve these models, which can be done within the phase-field framework. First we introduce a simple and systematic way to write a phase-field model from the current mixture models in the literature. Then, we should be able to include extra relevant phenomena, such as soft tissue dynamics. There are various ways of introducing mechanical effects in a phase-field model.

4.1. *Systematic approach to multiphase-field mixtures*

In Equation (11), the fields ϕ_k are still not phase-fields but volume fractions of the total density. However, in the spirit of Section 2.1, one can formalize the connection between these two approaches in order to clarify the role of different mechanisms on the tumor boundary. Note that, in practice, the theory of mixtures is an elegant approach but difficult to analyze without making strong assumptions on the shape of the tumor or the constitutive equations. Moreover, the dependence of the dynamics on the specific form of the reaction terms makes them less universal than their phase-field counterparts.

The idea behind the mapping between the theory of mixtures and multiphase-field models is that reaction terms have two roles:

(i) to define *fixed-points* of the dynamics; and
(ii) to establish reaction rates.

The first one defines the number of phases and the second one allows us to perform a parameter reduction through effective coarse grained time-scales.

4.1.1. *Systematic mapping procedure*

In previous sections, we have introduced the philosophy behind the mapping between the theory of mixtures and the multiphase-field approach to tumor modeling. In this section, we summarize the main steps of this mapping (for details see [56]):

(i) First we need to rewrite the equations for the volume fractions, ϕ_k, in a more suitable way. We consider separately the dynamics of the interstitial fluid, which corresponds to the subindex 0 in Equation (18) and obeys the Navier–Stokes equation. One can assume that the motion of the cells takes place at low Reynolds numbers [57] so inertial terms in the equation for the conservation of momentum are negligible.

(ii) Then, one can write an equation for the *partial* velocity of each phase through Equation (22). Thus,

$$\mathbf{v}_k = \mathbf{v}_0 - \frac{\rho_k}{\alpha_k \rho_0}\phi_k \nabla(p' + \mu_k') + \nabla \cdot \left(\mathcal{L}_k\left(\nabla \mathbf{v}_k + \nabla \mathbf{v}_k^T\right)\right). \tag{26}$$

(iii) So far, steps (i) and (ii) are simply a bit of make-up, although they will allow us to proceed in a systematic way. The next step involves writing explicitly how the boundary of every phase, ϕ_k, evolves with time. From Equation (26) the boundaries obey

$$\partial_t \phi_k + \mathbf{v}_k \cdot \nabla \phi_k = 0. \tag{27}$$

(iv) Finally, we can write down the equation for the multiphase-fields, ψ_k, which are defined by

$$\psi_k = \begin{cases} +1, & \text{inside phase } k \\ -1, & \text{outside phase } k. \end{cases} \tag{28}$$

Being more specific, Equation (27) is translated to

$$\partial_t \psi_i = \underbrace{\nabla \cdot (M \nabla \psi)}_{\text{Mobility}} \underbrace{-f'(\psi)}_{\text{Double well}} + \underbrace{F(\psi_i, \rho_i, \nabla \psi_i, \mu_i, \ldots)}_{\text{Coupling terms}}, \tag{29}$$

where F is a *proper* translation of the right-hand side of Equation (26) in terms of the new phase-fields, ψ_k.

(v) By *proper* in (4) we mean that both formulations are equivalent in the sharp-interface limit through the solvability condition (using an inverse method based on the casuistry of the sharp-interface limit).

The last step is the most delicate one, so in order to make it clearer, here we illustrate it with the following example.

4.1.1.1. *Tumor growth by proliferation+chemotaxis.* Consider the simplest phase-field model, known as model A in the terminology of phase-transitions [58],

$$\partial_t \phi = \epsilon^2 \nabla^2 \phi + \phi - \phi^3 + \epsilon\lambda. \tag{30}$$

The sharp-interface limit provides the equation:

$$\mathbf{v}_n = \lambda - \nu\kappa. \tag{31}$$

If the constitutive equation for the velocity were to contain no curvature term, for instance, one should include an additional term in Equation (30) of the form $\kappa|\nabla\phi|^2$ to cancel the effective term $\nu\kappa$ (this idea was used in [59]).

In addition, if chemotaxis is important, one could replace λ by a chemotaxis term of the form $\nabla(\chi(q)\nabla q)$.

Going back to the system proposed on Section 2.1.1, Equations (1)–(4), the equivalent phase-field model would be [56]:

$$\begin{aligned}
&\underbrace{\partial_t\psi = \nabla\cdot(M(\psi)\nabla\psi) - f'(\psi)}_{\text{general}} + \underbrace{\alpha\kappa(\psi)|\nabla\psi|^2}_{\text{no surface tension}} - \underbrace{\mathbf{v}_0\cdot\nabla\psi}_{\text{advection}} \\
&- \underbrace{\nabla\cdot(\psi\tilde{\chi}_1\nabla u_1 + \psi\tilde{\chi}_2\nabla u_2)}_{\text{chemotaxis}} + \underbrace{\nabla\cdot(\beta\tilde{\Pi}'\psi\nabla\psi)}_{\text{Mechanical interactions}} \\
&+ \underbrace{\lambda(\psi+1)u}_{\text{proliferation}}\ .
\end{aligned} \tag{32}$$

This equation needs some clarification. If the extra-cellular matrix is solid and there is no fluid phase (the matrigel in the case of the system reviewed in Section 2.1.1) then $\mathbf{v}_0 = 0$ and the mechanical interactions between the tumor cells and the matrigel can be removed from the last term and included *effectively* into the mobility M (which, otherwise, would be constant).

4.2. *Mechanical aspects in phase-field modeling*

Many tumors have distinctive elastic properties which should be considered during tumor growth [60]. Also in angiogenesis, the endothelial cell response to mechanical signals is at the core of the dynamics of capillary growth. In fact, it has been noticed that 'because angiogenesis occurs in a mechanically dynamic environment, future investigations should aim at understanding how cells integrate chemical and mechanical signals so that a rational approach to controlling angiogenesis will become possible' [63]. Still in [63] the authors call for computational models that correctly integrate this mechanical aspect into angiogenesis. This step is far from trivial, since the deformations are typically large. The phase-field community has worked extensively in the study of elastic stresses in materials applied mainly to small deformations. Even if this regime is not always relevant during tumor growth, it is important to probe the influence of stress in the growth of carcinomas and capillaries.

One of the first approaches to the study of elastic effects in the solid phase separation of alloys within the phase-field context was considered by Onuki et al. [64], who presented a Ginzburg–Landau theory that included a systematic analysis of the alloys' elasticity. The elastic energy contribution to the total free energy in this type of model can be introduced directly by expressing the elastic strain energy as a

function of field variables or by including coupling terms between the field variables and the displacement gradients in the free-energy functional:

$$F(\phi, u_{ij}) = \int d\vec{r} \left[f(\phi) + \frac{\epsilon^2}{2} |\nabla\phi|^2 + f_{\mathrm{cl}}(\phi, u_{ij}) + f_{\mathrm{el}}(u_{ij}) \right], \tag{33}$$

where $f_{\mathrm{el}}(u_{ij})$ is the elastic free energy term, $f_{\mathrm{cl}}(\phi, u_{ij})$ the term coupling the strain and the phase-field, $u_{ij} = \frac{1}{2}(\partial u_i/\partial x_j + \partial u_j/\partial x_i)$ is the strain, and u_i the displacement field.

Following the Ginzburg–Landau approach, different phase-field models were proposed to study the dynamics of solid–liquid interfaces or solid–solid interfaces where the elastic effects are important (see [8] for a review).

The coupling free energy in first order is given by $f_{\mathrm{cl}}(\phi, u_{ij}) = \varepsilon g(\phi) \nabla \cdot \vec{u}$. For an isotropic material and for a solid–liquid interface, for example, $f_{\mathrm{el}}(\phi, u_{ij})$ is given by [65]:

$$f_{\mathrm{el}}(\phi, u_{ij}) = \frac{k}{2} (\nabla \cdot \vec{u})^2 + g(\phi)\mu \times \sum_{ij} \left(u_{ij} - \frac{\delta_{ij}}{d} \nabla \cdot \vec{u} \right)^2, \tag{34}$$

where κ is the compressibility and μ is the shear modulus in the soft liquid phase alone.

One important feature of these models is the adiabatic assumption, accomplished by the local mechanical equilibrium equation

$$\delta F / \delta u_{ij} = 0, \tag{35}$$

which is just a consequence of the reasonable assumption that the elastic field relaxes much faster than ϕ. Replacing the solution of this equation for the strain field one can express the free energy in terms of ϕ alone, considering the simplified case of the absence of external strain and a flat surface with $\phi = \phi(y)$. Dynamics is then simulated via the standard relaxation dynamics given by the phase-field equation derived along the principles of Section 4.1.

The study of solid–solid phase transitions, including elasticity in the phase-field formulations, has been significantly developed recently. Following Khachaturyan's theory of micro-elasticity (see [66,67] for reviews), a school of phase-field models emerged with different applications to microstructure evolution in the solid state. In the context of multicomponent systems, in grain growth systems, for example, multiphase-field models have also been developed in order to incorporate the elasticity properties of the different phases [68,69].

To solve the mechanical equilibrium equation (35), most existing phase-field simulations assume homogeneous elasticity where the difference in the elastic modulus between different phases is neglected. There have been significant efforts to incorporate elastic inhomogeneities in phase-field formulations through the dependence of the elastic modulus tensor on the field variables. When these inhomogeneities are small, first-order approximations may be employed [64,70,71]. High-order approximations were incorporated in [72] using an iterative approach, allowing strong elastic inhomogeneity. Following this approach an improved formulation was recently presented in [73] where a three-dimensional phase-field micro-elasticity theory for elastically inhomogeneous solids is presented. Note also that these elastic

properties may be introduced directly in the multiphase-field approach described in Section 4.1.

5. Conclusion: phase-field and tumor dynamics

A tumor is a complex system with a variety of different mechanisms relevant to its growth. Adding to this complexity there are different types of tumors and their growth proceeds along different stages. It is crucial to find new ways to tackle this problem. The reasoning that solid tumor growth is at its core a moving boundary problem, where the different constituents in the system organize themselves in different phases, allows for the development of phase-field models applied to tumor growth dynamics. The phase-field models were originally developed in the physics community in the context of non-equilibrium systems to describe a whole range of materials science phenomena related to nucleation and growth of complex nonlinear problems with moving boundaries. The application of phase-field modeling to tumor growth provides the fascinating possibility of knowledge transfer between the materials science community and the biomedical and clinical communities.

Many of the biological experiments can only provide a qualitative description of tumor growth offering phase-field modeling an opportunity of playing an important role in their explanation. Here we have reviewed the most relevant phase-field approaches describing the mechanisms of tumor growth in its avascular and vascular stages of evolution. This method is specially useful when the phases are clearly defined as in a solid tumor, not describing lymphomas for example.

Phase-field models have been used to understand how hetero and homotype chemotaxis mechanisms compete and/or cooperate in the formation of tumor branching structures in its avascular stage. This model allowed us to conclude that although tumor cell proliferation is a requirement for invasive branching behavior it cannot generate the invasion by itself. It also showed that heterotype chemotaxis provides an instability mechanism that leads to the onset of tumor cell invasion and that homotype chemotaxis does not provide such a mechanism but enhances the mean speed of the tumor surface.

Phase-field models can also capture relevant features of the angiogenesis dynamics providing insights into the parameters controlling the final capillary network morphology as well as explaining mechanisms playing an important role in capillary formation *in vivo*.

Finally, we presented a recently developed phase-field description of a multiphase model for avascular tumor growth that is able to produce quantitative predictions for the size and evolution of the tumor.

After conducting an overview of the current applications of phase-field models in tumor growth we made a short incursion through the possible improvements of these models. We started by systematizing the process of mapping between the theory of mixtures and the multiphase-field approaches in order to understand how extra relevant phenomena, such as mechanical effects, may be included in tumor phase-field modeling. We then proceeded with a short review of the current phase-field approaches that included elastic effects in their modulation.

The phase-field model is a new approach for cancer modeling that is easily generalized to include more complicated mechanisms leading to a quantitative simulation of the *in vivo* problem, thus providing in the future a benchmark for the biomedical and clinical communities.

Acknowledgements

RDMT thanks Fundação para a Ciência e Tecnologia (FCT) and Fundação Calouste Gulbenkian for financial support through, respectively, the *Ciência 2007* and *Estímulo à Investigação* programs. MC thanks the Spanish Ministry of Science and Innovation through Grant No. FIS2009-12964-C05-03.

References

[1] L.D. Wood, D. Williams Parsons, S. Jones, J. Lin, T. Sjöblom, R.J. Leary, D. Shen, S.M. Boca, T. Barber, J. Ptak, N. Silliman, S. Szabo, Z. Dezso, V. Ustyanksky, T. Nikolskaya, Y. Nikolsky, R. Karchin, P.A. Wilson, J.S. Kaminker, Z. Zhang, R. Croshaw, J. Willis, D. Dawson, M.I. Shipitsin, J.K.V. Willson, S. Sukumar, K. Polyak, B. Ho Park, C.L. Pethiyagoda, P.V. Krishna Pant, D.G. Ballinger, A.B. Sparks, J. Hartigan, D.R. Smith, E. Suh, N. Papadopoulos, P. Buckhaults, S.D. Markowitz, G. Parmigiani, K.W. Kinzler, V.E. Velculescu and B. Vogelstein, Science 318 (2007) p.1108.
[2] C.C. Maley, P.C. Galipeau, J.C. Finley, V. Jon Wongsurawat, X. Li, C.A. Sanchez, T.G. Paulson, P.L. Blount, R.-A. Risques, P.S. Rabinovitch and B.J. Reid, Nature Gen. 38 (2006) p.468.
[3] R.P. Araújo and D.L.S. McElwain, Bull. Math. Biol. 66 (2004) p.1039.
[4] R.T. Skeel and S.N. Khleif, *Biological and pharmacological basis of cancer chemotherapy and biotherapy*, in *Handbook of Cancer Chemotherapy*, R.T. Skeel, ed., Lippincott Williams & Wilkins, Philadelphia, 2007, p.1.
[5] R.M.W. de Waal and W.P.J. Leenders, *Sprouting angiogenesis versus co-option in tumor angiogenesis*, in *Mechanisms of Angiogenesis*, M. Clauss and G. Breier, eds., Birkhauser, Basel, 2005, p.65.
[6] W.P.J. Leenders, B. Kusters and R.M.W. de Waals, Endothelium 9 (2002) p.83.
[7] W.D. Figg and J. Folkman (eds.), *Angiogenesis – An Integrative Approach from Science to Medicine*, Springer, New York, 2008.
[8] H. Emmerich, Adv. Phys. 57 (2008) p.1.
[9] M. Castro, C. Molina-París and T.S. Deisboeck, Phys. Rev. E 72 (2005) p.041907.
[10] R.D.M. Travasso, E. Corvera Poiré, M. Castro, J.C. Rodríguez-Manzaneque, and A. Hérnandez-Machado, *Tumor angiogenesis and vascular patterning: A mathematical model*; submitted.
[11] C. Betsholtz, B. Westermark, B. Ek and C.H. Heldin, Cell 39 (1984) p.447.
[12] J. Laterra, E. Rosen, M. Nam, S. Ranganathan, K. Fielding and P. Johnston, Biochem. Biophys. Res. Commun. 235 (3) (1997) p.743.
[13] M.R. Chicoine, C.L. Madsen and D.L. Silbergeld, Neurosurgery 36 (6) (1995) p.1165.
[14] M.J. Plank, B.D. Sleeman and P.F. Jones, J. Theor. Medicine 4 (2002) p.251.
[15] M.J. Plank and B.D. Sleeman, Bull. Math. Biol. 66 (2004) p.1785.
[16] L.M. Sander and T.S. Deisboeck, Phys. Rev. E 66 (2002) p.051901.
[17] N. Bellomo, E. De Angelis and L. Preziosi, J. Theor. Medicine 5 (2003) p.111.

[18] N. Bellomo, A. Bellouquid and M. Delitala, Math. Models Meth. Appl. Sci. 14 (2004) p.1683.
[19] T.S. Deisboeck, M.E. Berens, A.R. Kansal, S. Torquato, A.O. Stemmer-Rachamimov and E.A. Chiocca, Cell Prolif. 34 (2001) p.115.
[20] A. Wells, Adv. Cancer Research 78 (2000) p.32.
[21] A.J. Ekstrand, C.D. James, W.K. Cavenee, B. Seliger, R.F. Pettersson and V.P. Collins, Cancer Res. 51 (8) (1991) p.2164.
[22] H. Greenspan, J. Theor. Biol. 56 (1976) p.229.
[23] D.S. Jones and B.D. Sleeman, *Differential Equations and Mathematical Biology*, CRC Press, London, 2003, and references therein.
[24] S. Habib, C. Molina-París and T.S. Deisboeck, Physica A 327 (2003) p.501.
[25] Z. Wang and T.S. Deisboeck, Sci. Model. Simul. 15 (2008) p.381.
[26] N. Mantzaris, S. Webb and H. Othmer, J. Math. Biol. 49 (2004) p.111.
[27] D. Manoussaki, S.R. Lubkin, R. Vernon and J.D. Murray, Acta Biotheor. 44 (1996) p.271.
[28] J.D. Murray, *Mathematical Biology II: Spatial Models and Biomedical Applications*, 3rd ed., Springer, NewYork, 2003, p.416.
[29] L. Tranqui and P. Tracqui, C.R. Acad. Sci. 323 (2000) p.31.
[30] P. Namy, J. Ohayon and P. Tracqui, J. Theor. Biol. 227 (2004) p.103.
[31] M. Kiani and A. Hudetz, J. Theor. Biol. 150 (1991) p.547.
[32] M.E. Gottlieb, IEEE Eng. Med. Bio. Mag. 13 (1991) p.2196.
[33] G. Landini and G. Misson, Invest. Opthamol. Visual Sci. 34 (1993) p.1872.
[34] A.R.A. Anderson and M.A.J. Chaplain, Bull. Math. Biol. 60 (1998) p.857.
[35] M. Markus, D. Bohm and M. Schmick, Math. Biosci. 156 (1999) p.191.
[36] M.A.J. Chaplain, S.R. McDougall and A.R.A. Anderson, Annu. Rev. Biomed. Eng. 8 (2006) p.233.
[37] A.L. Bauer, T.L. Jackson and Y. Jiang, Biophys. J. 92 (2007) p.3105.
[38] M.R. Owen, T. Alarcon, P.K. Maini and H.M. Byrne, J. Math. Biol. 58 (2009) p.689.
[39] K. Bentley, H. Gerhardt and P.A. Bates, J. Theor. Biol. 250 (2008) p.25.
[40] A.M. Schor, S.L. Schor and R. Baillie, *Angiogenesis: experimental data relevant to theoretical analysis*, in *On Growth and Form: Spactio-Temporal Pattern Formation in Biology*, M.A.J. Chaplain, G.D. Singh and J.C. McLachlan, eds., John Wiley & Sons, New York, 1999, p.201.
[41] F. Milde, M. Bergdorf and P. Koumoutsakos, Biophys. J. 95 (2008) p.3146.
[42] M. Hellström, L.K. Phng, J.J. Hofmann, E. Wallgard, L. Coultas, P. Lindblom, J. Alva, A.K. Nilsson, L. Karlsson, N. Gaiano, K. Yoon, J. Rossant, M.L. Iruela-Arispe, M. Kalén, H. Gerhardt and C. Betsholtz, Nature 445 (2007) p.776.
[43] S. Lee, S.M. Jilani, G.V. Nikolova, D. Carpizo and M.L. Iruela-Arispe, J. Cell Biol. 169 (2005) p.681.
[44] J.C. Rodriguez-Manzaneque, T.F. Lane, M.A. Ortega, R.O. Hynes, J. Lawler and M.L. Iruela-Arispe, Proc. Nat. Am. Sci. 22 (2001) p.12485.
[45] S. Sanga, H.B. Frieboes, X. Zheng, G. Gatenby, E.L. Bearer and V. Cristini, Neuroimage 37 (2007) p.S120.
[46] R.P. Araújo and D.L.S. McElwain, SIAM J. Appl. Math. 65 (2005) p.1261.
[47] R.P. Araújo and D.L.S. McElwain, SIAM J. Appl. Math. 66 (2005) p.447.
[48] H.M. Byrne, J.R. King, D.L.S. McElwain and L. Preziosi, Appl. Math. Lett. 16 (2003) p.567.
[49] S.J. Franks, H.M. Byrne, H.S. Mudhar, J.C.E. Underwood and C.E. Lewis, J. Math. Biol. 47 (2003) p.277.
[50] H.M. Byrne and L. Preziosi, Math. Med. Biol. 20 (2003) p.341.
[51] X. Zheng, S.M. Wise and V. Cristini, Bull. Math. Biol. 67 (2005) p.211.

[52] H.B. Frieboes, J.S. Lowengrub, S. Wise, X. Zheng, P. Mackin, E.L. Bearer and V. Cristini, Neuroimage 37 (2007) p.S59.
[53] V. Cristini, X. Li, J.S. Lowengrub and S.M. Wise, J. Math. Biol. 58 (2009) p.723.
[54] V. Cristini, J. Lowengrub and Q. Nie, J. Math. Biol. 46 (2003) p.191.
[55] A.J. Bray, Adv. Phys. 43 (1994) p.357.
[56] M. Castro, R.D.M. Travasso and C. Molina-París, *Multiphase-field approach to tumor growth*; in preparation.
[57] E.M. Purcell, Am. J. Phys. 45 (1977) p.3.
[58] P.C Hohenberg and B.I. Halpering, Rev. Mod. Phys. 49 (1977) p.435.
[59] R. Folch, J. Casademunt, A. Hernández-Machado and L. Ramirez-Piscina, Phys. Rev. E 60 (1999) p.1724.
[60] B.S. Winters, S.R. Shepard and R.A. Foty, Int. J. Cancer 114 (2005) p.371.
[61] S.M. Wise, J. Kim and J.S. Lowengrub, J. Comp. Phys. 226 (2007) p.414.
[62] S. Pennacchietti, P. Michieli, M. Galluzzo, M. Mazzone, S. Giordano and P.M. Cornoglio, Cancer Cell 3 (2003) p.347.
[63] Y.-T. Shiu, J.A. Weiss, J.B. Hoying, M.N. Iwamoto, I.S. Joung and C.T. Quam, Critical Rev. Biomed. Eng. 33 (2005) p.431.
[64] J. Onuki, J. Phys. Soc. Jpn. 58 (1989) p.3065.
[65] J. Muller and M. Grant, Phys. Rev. Lett. 82 (1999) p.1736.
[66] A.G. Khachaturyan, *Theory of Structural Transformations in Solids*, Wiley, New York, 1983.
[67] L. Chen, Annu. Rev. Mater. Res. 32 (2002) p.113.
[68] W. Dreyer and W. Muller, Int. J. Solids Struct. 37 (2000) p.3841.
[69] I. Steinbach, Model Simul. Mater. Sc. 17 (2009) p.073001.
[70] H. Nishimori and A. Onuki, Phys. Rev. B 42 (1990) p.980.
[71] C. Sagui, D. Orlikowski, A.M. Somoza and C. Roland, Phys. Rev. E 58 (1998) p.R4092.
[72] S.Y. Hu and L.Q. Chen, Acta Materialia 49 (2001) p.1879.
[73] Y. Shen, Y. Li, Z. Li, H. Wan and P. Nie, Scripta Materialia 60 (2009) p.901.

PHILOSOPHICAL MAGAZINE

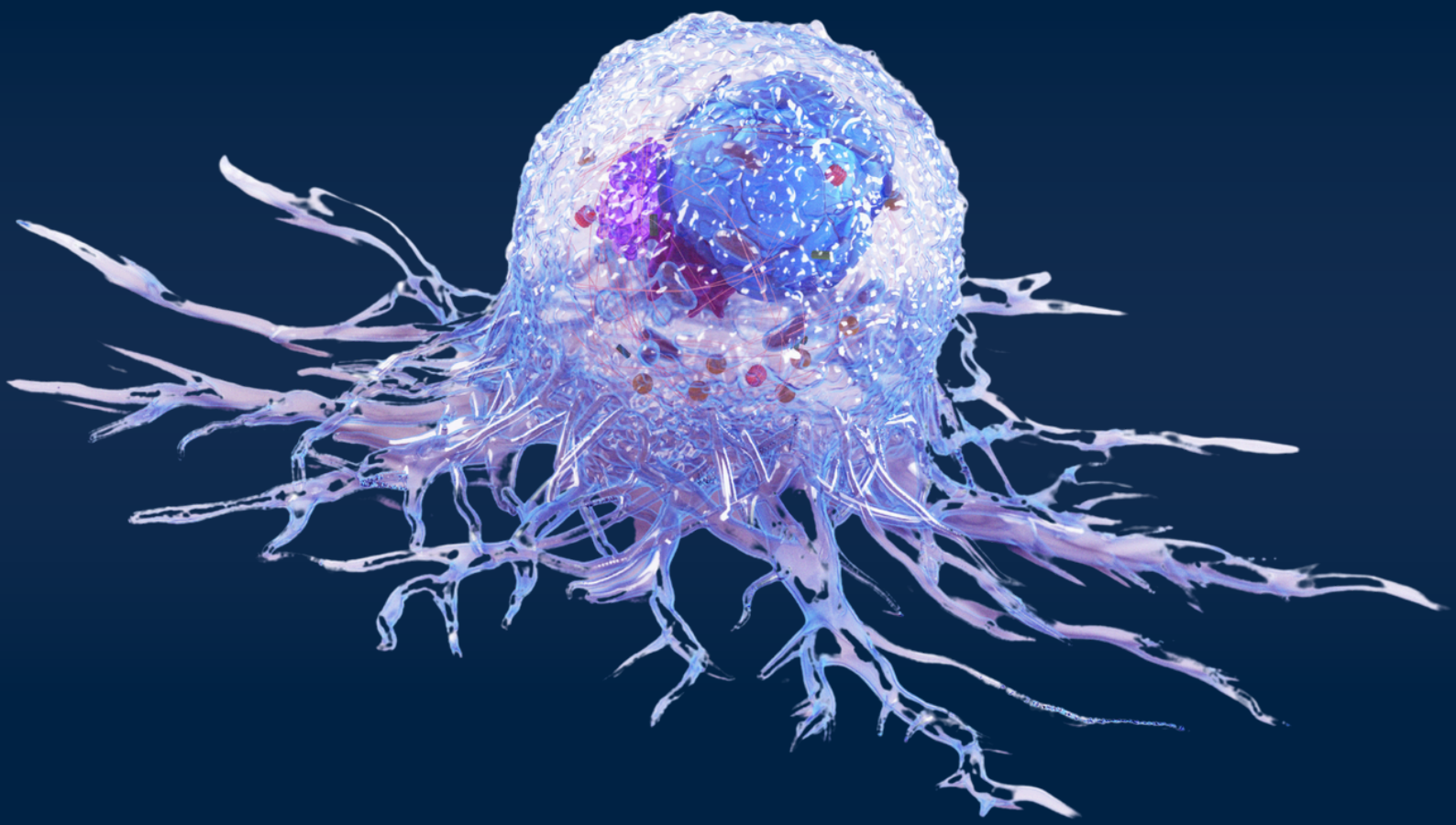

Contact us

Editorial Department | digitaleditor@philosophicalmagazine.com

Taylor & Francis
by informa